FILTERING OF ACOUSTIC INFORMATION FROM AERO-OPTICAL MEASUREMENTS

A Dissertation

Submitted to the Graduate School
of the University of Notre Dame
in Partial Fulfillment of the Requirements
for the Degree of

Doctor of Philosophy

by

Brian Lowell Catron

R. Mark Rennie , Co-Director

Eric J. Jumper, Co-Director

Graduate Program in Aerospace and Mechanical Engineering
Notre Dame, Indiana

December 2021

FILTERING OF ACOUSTIC INFORMATION FROM AERO-OPTICAL MEASUREMENTS

Abstract

by

Brian Lowell Catron

Abstract Goes Here

To my wife Karen & our son Arthur

CONTENTS

FIGURES

TABLES

SYMBOLS

Ap	Aperture size - Typically diameter
I	Actual on target intensity
I_0	Diffraction-limited intensity
k	Wavenumber ($k = 2\pi/\lambda$)
n	Index of refraction
OPD	Optical path difference
$\mathrm{OPD}_{\mathrm{RMS}}$	Spatial OPD root-mean-square
SR	Strehl ratio ($\mathrm{SR} = I/I_0$)
	Greek
δ	Boundary layer thickness
$\langle \theta^2 \rangle$	Mean-squared of the fluctuating deflection angle

ACKNOWLEDGMENTS

CHAPTER 1

INTRODUCTION

FINISHED

There have been two major attempts to field a directed-energy system aboard an aircraft to date [21]. The first was the Airborne Laser Laboratory (ALL) which took place in the late 1970's and early 1980's which used a CO_2 laser with a wavelength of 10.6-μm. The second was the Airborne Laser (ABL) program which operated in the 2000's and used a COIL laser at 1.315-μm. Airborne optical systems like ALL and ABL have to deal with a phenomenon known as "aero-optics," which refers to optical distortions caused by compressible aero-dynamic flow features that pass through the outgoing beam. These optical distortions were first noticed due to image degradation in wind tunnel measurements in the 1950's [43] as well as in photo-reconnaissance missions in the 1960's [23].

The peak on-target irradiance of a beam passing through an optical disturbance, I, divided by the diffraction-limited performance, I_0, is known as the Strehl ratio [27], SR,

$$\mathrm{SR} = \frac{I}{I_0}. \tag{1.1}$$

The diffraction-limited performance is the beam intensity that would exist on the same target if not for the optical disturbance. The Airborne Laser Laboratory had an estimated Strehl ratio of 95%[21] so that the "aero-optics problem" effectively did not apply for this case. Following the Airborne Laser Laboratory program there was a desire to move toward shorter wavelengths in order to take advantage of improved diffraction-limited performance, leading to a smaller-diameter focused spot on target with a higher irradiance I_0: [20],

$$\frac{I_0}{P} = \frac{1}{\pi}\left(\frac{Ap}{\lambda z}\right)^2, \tag{1.2}$$

where P is the laser output power, Ap is the aperture size, and z is the propagation distance. The improvement in diffraction-limited performance as the laser wavelength is decreased is shown in

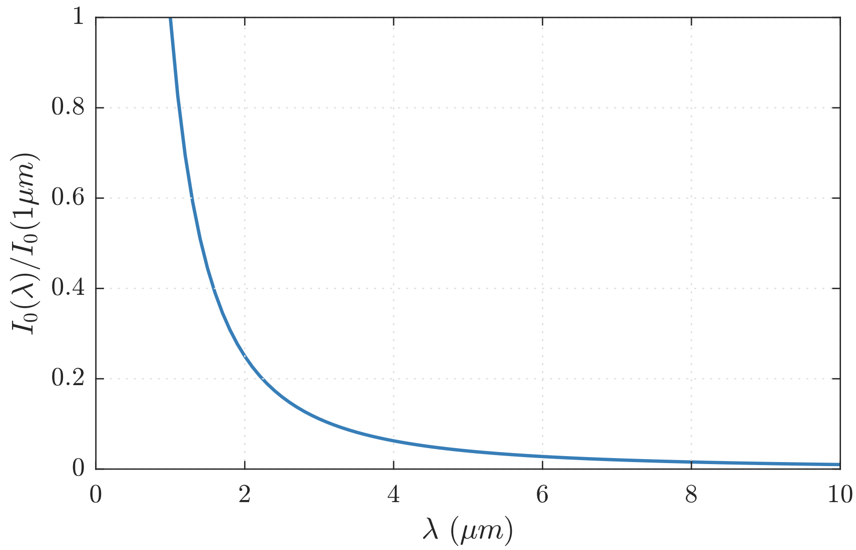

Figure 1.1. Diffraction-limited far-field intensity of a beam normalized by the performance at 1-μm.

Figure 1.1. By only changing the laser source from a 10-μm to 1-μm wavelength the diffraction-limited performance can be increased 100 times.

Aero-optical issues start to become important as the wavelength is decreased as is evident from the Maréchal approximation [28] which relates the Strehl ratio to wavelength,

$$\mathrm{SR} \approx \exp\left\{-\left[\frac{2\pi\,\mathrm{OPD_{RMS}}}{\lambda}\right]^2\right\}, \tag{1.3}$$

where $\mathrm{OPD_{RMS}}$ is the spatial root-mean-square of the optical path difference over the aperture and is a way to quantify the optical disturbance as will be discussed further in Chapter 2. As stated above, the ALL had a Strehl ratio of 95%; however, if the ALL system's laser was swapped with another laser of a lower wavelength, the Strehl ratio would significantly decrease as shown by Figure 1.2. While going from 10 to 1-μm hypothetically results in a 100-fold increase in diffraction-limited performance, the actual on-target intensity that this hypothetical system obtains would be essentially zero due to the much larger effect that aero-optical aberrations have on the outgoing beam as the wavelength is reduced. This means that the aero-optical problem can no longer be ignored, which was recognized as one of the main developmental risks of the ABL program [13].

As the next generation of airborne directed-energy systems are developed some amount of ground testing of those systems will need to occur. In order to understand the aero-optical environment

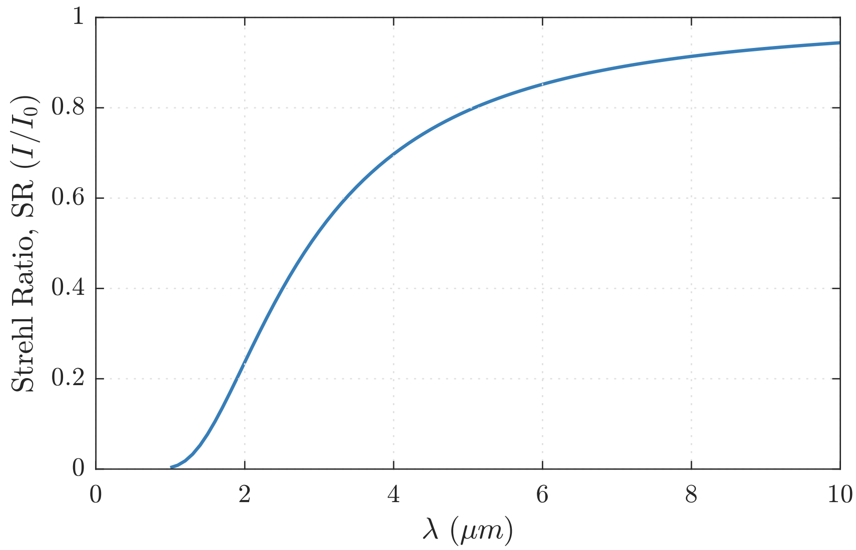

Figure 1.2. Strehl ratio due to the $\mathrm{OPD}_{\mathrm{RMS}}$ of the Airborne Laser Laboratory (ALL) at various laser wavelengths. ALL had an estimated Strehl ratio of 95% with its 10.6-μm laser.

that these systems will experience in the air, wind tunnel tests will need to be employed. These tests are cheaper to perform than, for example, flight testing, and allow for quicker iteration of design parameters. However, as will be described in further detail in Chapter 2, wind-tunnel measurements of aero-optical effects typically require passing a test beam into and through the test-section, so that the test beam is susceptible to acquiring additional optical contamination including but not limited to the boundary layer present on the wall and the acoustic environment generated by the wind tunnel fan [17]. Note that it is common in signal-processing terminology to use the word "noise" to describe unwanted interference that appears in addition to the "signal" that is the objective of the measurement; however, in this dissertation, the word "contamination" is used to describe any optical noise sources that are unrelated to the aero-optical signal, in order to avoid confusion with use of the word "noise" to describe acoustic noise which, as will be shown, is also a source of optical contamination.

Assuming that the optical disturbances from aero-optical effects are statistically independent from the contaminating optical disturbances from the testing environment, we can estimate the total optical disturbance as

$$\mathrm{OPD}_{\mathrm{RMS}}{}^2_{TOTAL} = \mathrm{OPD}_{\mathrm{RMS}}{}^2_{MODEL} + \mathrm{OPD}_{\mathrm{RMS}}{}^2_{ENVIRONMENT}\,. \tag{1.4}$$

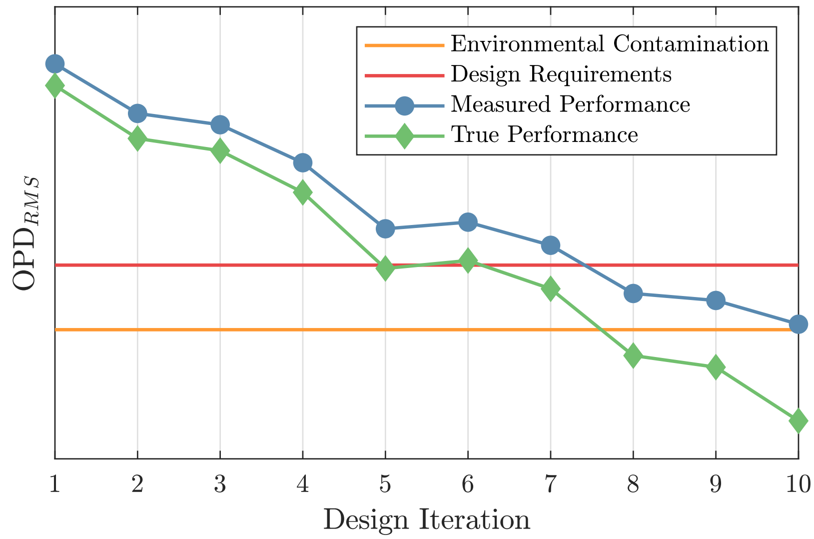

Figure 1.3. Hypothetical iterative design process of an airborne directed-energy system. The required performance level is shown by the red line and the testing environment's contamination is shown by the orange line.

an example of the effect that optical contamination may have on system design, Figure 1.3 illustrates a hypothetical iterative design process, where the design objective is to obtain a design that meets a required level of performance shown in red, in the presence of a level of environmental optical contamination shown in orange. The design process was simulated by an initial aero-optical $\mathrm{OPD}_{\mathrm{RMS}}$ shown on the left of the plot, and the improvement in system performance achieved with each design iteration was simulated as a nearly linear reduction in $\mathrm{OPD}_{\mathrm{RMS}}$ combined with 15% random variation. If only the measured data, that is, including the effect of environmental contamination using Equation 1.4, is used to assess the system's performance then three additional design iterations are needed to achieve a usable design, which can add significantly to the development time and costs. If the environmental contamination is greater than the design requirement, the measured performance will never reach the required performance criteria. However, if the environmental contamination can be estimated, mitigated and/or removed, then the measured performance is a more accurate evaluation of the true aero-optical performance, and design convergence can be achieved more quickly and with more accurate results.

This dissertation will examine the environmental contamination of aero-optical measurements in wind tunnels, with a particular focus on the contamination due to acoustic noise within the wind tunnel. A review of the available literature and important concepts in given in Chapter 2. In Chapter 3, the optical disturbances caused by acoustic waves from simple plane and spherical waves are presented, leading to a process for estimating the acoustical environment within the test section of a wind tunnel. The strength of an spherical acoustic wave will be assessed with both microphone and optical measurements. Multi-dimensional spectral techniques will be used to analyze optical wavefronts in Chapter 4 and to filter optical wavefronts in Chapter 6. These filtering techniques will contain some optical contamination particularly in regions where the various signal components interfere with one another. In order to further reduce the optical contamination, Chapter 7 will utilize additional sensor information from both microphones and accelerometers to remove some of the overlapping contamination to obtain a better picture of the actual optical performance of an airborne directed-energy system from ground test measurements.

CHAPTER 2

LITERATURE REVIEW

The literature review will consist of primarily two sections. The first section will examine aero-optics while the second will look at acoustics inside of ducts.

2.1 Aero-Optics

Optical communication and directed energy systems require a tightly focused beam on target in order to meet system performance objectives. The farfield performance of airborne optical systems can be degraded by the nearfield flow that becomes optically active at compressible flow speeds. "Aero-optics" is the study of the optical effect of these nearfield flow disturbances. Examples of important aero-optical flows that have been studied extensively include boundary layers [17, 42, 45], shear layers [14, 38], shock waves [21], and even tip vortices [36]. The effect of acoustic disturbances on aero-optical measurements has also been shown in both flight testing [12] and ground testing [9, 10].

In these optically active flows the index-of-refraction, n, varies locally as does the other fluid properties. Gladstone and Dale [15] found that the index-of-refraction is primarily a function of density with a loose dependence on the wavelength of light. Gladstone and Dale proposed a "specific refractive energy" now known as the Gladstone-Dale constant, K_{GD},

$$K_{GD} = \frac{n-1}{\rho}. \tag{2.1}$$

For air the refractive index can be related to state quantities [44]

$$n - 1 = 77.6 \times 10^{-6} \frac{P}{T} \left(1 + \frac{7.53 \times 10^{-3}}{\lambda^2}\right), \tag{2.2}$$

where P is in mbar, T is in K, and λ is in μm. By combining this relationship with the ideal gas

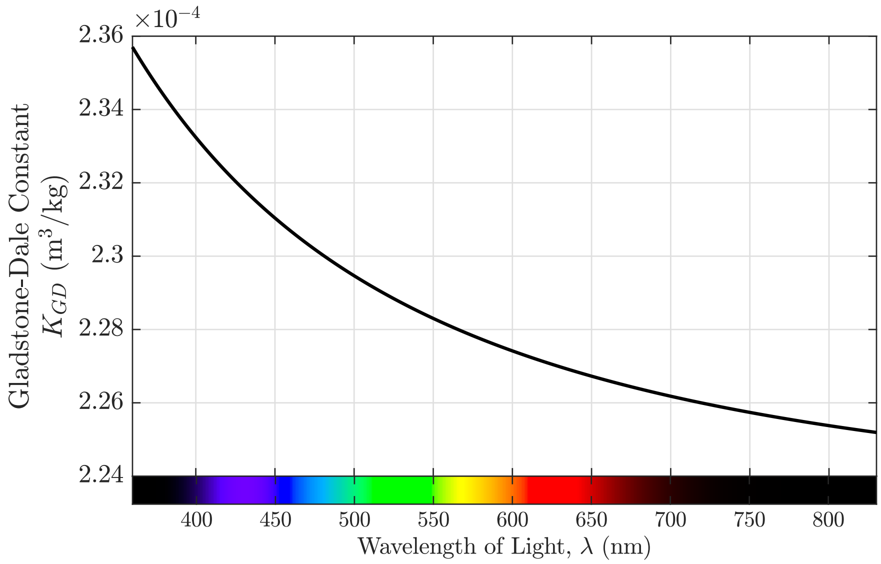

Figure 2.1. Gladstone-Dale constant for air over the visible wavelength range.

law, the Gladstone-Dale constant can be determined as a function of light wavelength,

$$K_{GD} = 2.23 \times 10^{-4} \left(1 + \frac{7.53 \times 10^{-3}}{\lambda_{\mu m}^2}\right) \left[\frac{m^3}{kg}\right]. \tag{2.3}$$

The Gladstone-Dale constant for air over the visible range is shown in Figure 2.1. While the value for K_{GD} does vary over the visible range, it is only a few percent, and many sources use an average value of $2.27{\times}10^{-4}$ m^3/kg for the visible and near-infrared [19]. The Gladstone-Dale relationship is typically presented as

$$n = 1 + K_{GD}\rho \tag{2.4}$$

but when applied to situations where there are significant fluctuations in the flow an alternate form is often more useful

$$n' = K_{GD}\rho' \tag{2.5}$$

where $'$ denotes the quantity represents the fluctuating component ($n' = n - \bar{n}$).

When a beam with an initially planar wave front passes through a region of optical active flow its wave front aberrated The optical path length (OPL) at any point in the beam can be obtained by integrating the index of refraction along the propagation of an optical ray [22].

$$\mathrm{OPL}(x, y, t) = \int_{s_1}^{s_2} n(x, y, z, t)ds \tag{2.6}$$

The optical path difference (OPD), is then the spatially-averaged OPL over an aperture removed from the OPL.

$$\text{OPD}(x, y, t) = \text{OPL}(x, y, t) - \langle \text{OPL}(x, y, t) \rangle \tag{2.7}$$

When working with fluctuating components, the OPD can be calculated directly

$$\text{OPD}(x, y, t) = \int_{s_1}^{s_2} n'(x, y, z, t) ds. \tag{2.8}$$

When OPD is combined with the beam intensity profile, one can compute the farfield complex amplitude distribution using the Fraunhofer approximation [16].

$$U(x_0, y_0, t) \propto \iint_{Ap} \exp\left\{\frac{2\pi j}{\lambda}\left[\text{OPD}(x_1, y_1, t) - \frac{(x_0 x_1 + y_0 y_1)}{z}\right]\right\} dx_1 dy_1 \tag{2.9}$$

where U is the complex amplitude, the subscripts 0 and 1 represent the coordinates of the farfield and nearfield respectively. The intensity can be computed from the complex amplitude via: $I = UU^*$. For cases in which optical aberrations are nonexistent (i.e. $\text{OPD}(x, y, t) = 0$), the farfield irradiance pattern that results from Equation 2.9 is caused entirely by diffraction from the optical aperture, and is referred to as the "diffraction-limited" irradiance pattern. For a beam with a flat wave front and circular aperture, the farfield irradiance pattern is the Airy's disk, and the peak irradiance at the center of the disk, I_0 , is the maximum irradiance that can be achieved by the optical system:

$$I_0 = \left(\frac{kAp^2}{8z}\right)^2 \tag{2.10}$$

where k is the wavenumber ($k = 2\pi/\lambda$), Ap is the aperture diameter, and z is the distance from the aperture. In the presence of aero-optical aberrations, $\text{OPD}(x, y, t)$ is non-zero, and the farfield irradiance pattern in this case tends to be more spread out and diffuse than the diffraction-limited case; furthermore, the beam may be shifted off target by optical tip/tilt imposed by the aberrations.

The Strehl ratio (SR), is the ratio of intensity on target (I) to the diffraction-limited on target intensity (I_0):

$$\text{SR} = \frac{I}{I_0} \tag{2.11}$$

The Strehl ratio can be computed accurately by applying Equation 2.9 twice, once for the diffraction-limited case to obtain I_0, and a second time with the OPD field due to aero-optical aberrations included to obtain I. The farfield performance, can also be estimated via the Maréchal approximation:

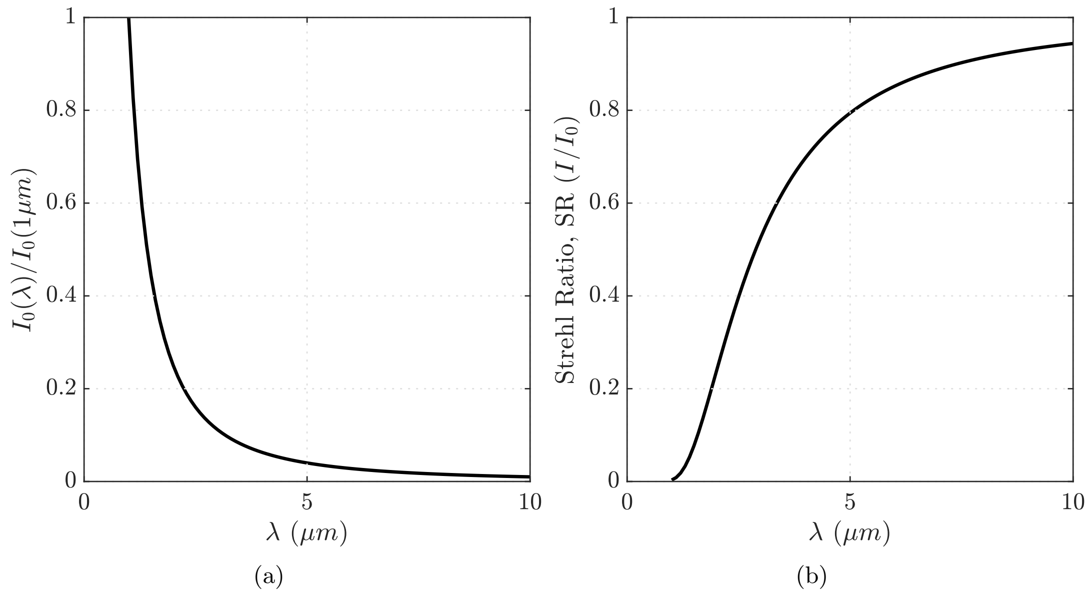

Figure 2.2. (a) Diffraction limited on target intensity as a function of wavelength normalized by the value at $\lambda = 1$ μ m. (b) Strehl ratio as a function of wavelength for an aberration that gives SR = 0.95 at $\lambda = 10.6$ μm.

$$\mathrm{SR}(t) \equiv \frac{I(t)}{I_0} \approx \exp\left\{-\left[\frac{2\pi\,\mathrm{OPD_{RMS}}(t)}{\lambda}\right]^2\right\} \tag{2.12}$$

where $\mathrm{OPD_{RMS}}$ is the spatial rms of the wave front and λ is the wavelength of the beam. Equation 2.12 shows a key relationship between OPD, wavelength, and the farfield performance, plotted in Figure 2.2b. On the other hand, Equation 2.10 shows that the diffraction-limited farfield irradiance increases as the wavelength is shortened, plotted in Figure 2.2a. Together, Figure 2.2a and 2.2b show that as modern optical systems move to shorter wavelengths to increase I_0, aero-optical aberrations cause a much more serious degradation of the Strehl ratio, illustrating why aero-optical considerations are critical in the development of any airborne optical system.

Figure 2.3 shows the $\mathrm{OPD_{RMS}}$ necessary to achieve various Strehl ratios over a range of wavelengths. As the wavelength of light decreases the required $\mathrm{OPD_{RMS}}$ decreases linearly for a fixed Strehl ratio.

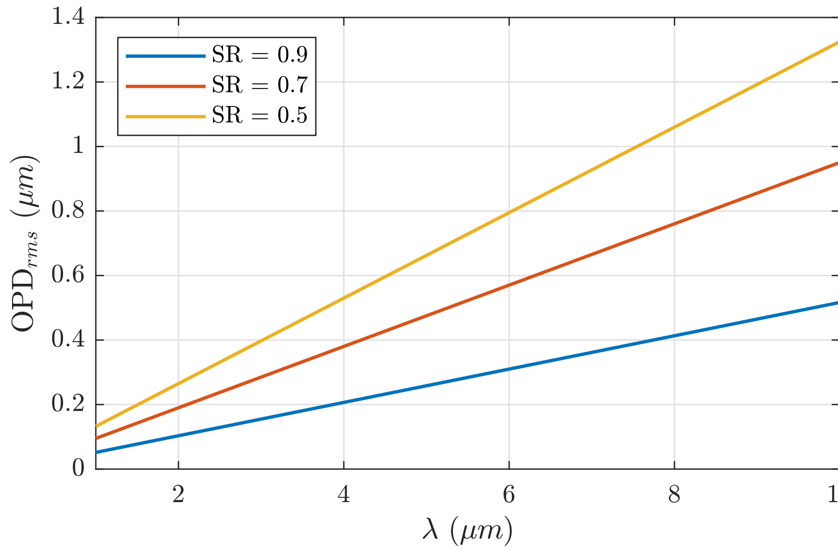

Figure 2.3. OPD$_{\mathrm{RMS}}$ values necessary to obtain Strehl ratios of 0.9, 0.7, and 0.5 over a range of wavelengths.

2.1.1 Typical Optical Wavefront Measurement System

2.1.2 A Brief History of Aero-Optics

The field of aero-optics began with an investigation by Liepmann [24] into the limits of sensitivity of schlieren systems when used in high-speed flow analysis. Liepmann used geometric optics to analyze a small-diameter beam and derive its mean-squared fluctuating deflection angle, $\langle \theta^2 \rangle$. Liepmann propagated the beam in the y direction and assumed the index of refraction changes in the $x - z$ plane were statistically similar. Liepmann's analysis for a boundary layer of thickness δ resulted in

$$\langle \theta^2 \rangle = \frac{1}{[n_0(\delta)]^2} \int_0^{\delta} \int_0^{\delta} n_0(y) n_0(\zeta) \left\langle \left(\frac{\partial \nu}{\partial y} \right)^2 \right\rangle R_v(|y - \zeta|) dy d\zeta \tag{2.13}$$

where the index of refraction is determined from $n = n_0(y)(1 + \nu)$ and $R_v(|y - \zeta|)$ is the correlation function for the index variation. This analysis introduced the concept of a linking equation that allows one to predict time-averaged optical degradation to turbulent flow statistical measurements.

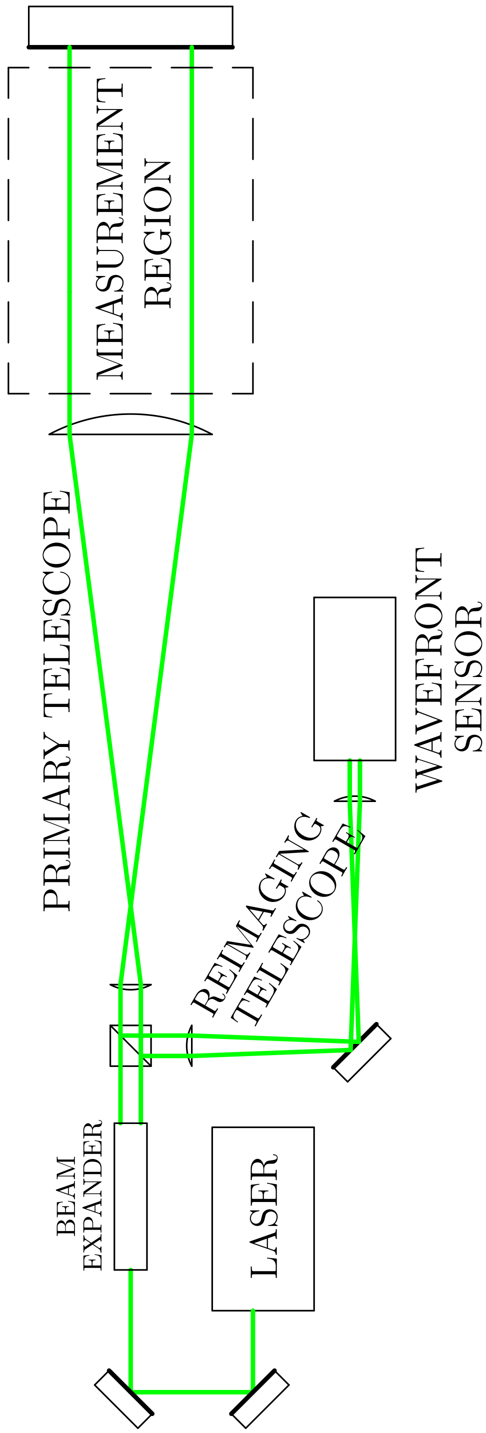

Figure 2.4. Typical double-pass optical wavefront measurement setup.

2.2 Acoustics

2.2.1 Basic Acoustics

Starting with the conservation of mass,

$$\frac{\partial \rho}{\partial t} + \nabla \cdot (\rho \mathbf{u}) = 0, \tag{2.14}$$

and separating the density into a time-averaged (ρ_0) and fluctuating portion (ρ'), $\rho = \rho_0 + \rho'$. The fluctuating conservation of mass equation is obtained by separating the density ($\rho = \rho_0 + \rho'$) into a temporally averaged density, ρ_0, and a

$$\frac{\mathbf{D}\rho'}{\mathbf{Dt}} + \nabla \cdot (\rho_0 \mathbf{u}) = 0 \tag{2.15}$$

For acoustics waves of frequency less than 10^9 Hz the compression of the fluid can be assumed to be adiabatic [30].

$$\left.\frac{\partial p}{\partial \rho}\right|_s = c_0^2 \tag{2.16}$$

2.2.2 Duct Acoustics

Acoustic waves are often enclosed inside of somesort of structure. This section will look at acoustics when confined to a duct in which the acoustic waves primarily travel along one-axis and have walls confining the acoustics along the other two axes as is the case inside of a wind tunnel. Figure 2.5 shows the diagram used for deriving the acoustic properties inside of a constant area duct.

This derivation is primarily influenced from Munjal [31] along with Jacobsen and Juhl [18]. The primary assumption used in this derivation is that the duct is of constant cross-section. This means that all mean quantities (ρ_0, $\mathbf{u_0}$, ...) a constant throughout space and time. Starting with the linearized inviscid forms of the conservation of mass,

$$\frac{\mathbf{D}\rho}{\mathbf{Dt}} + \rho_0 \nabla \cdot \mathbf{u} = 0, \tag{2.17}$$

and conservation of momentum,

$$\rho_0 \frac{\mathbf{Du}}{\mathbf{Dt}} + \nabla p = 0. \tag{2.18}$$

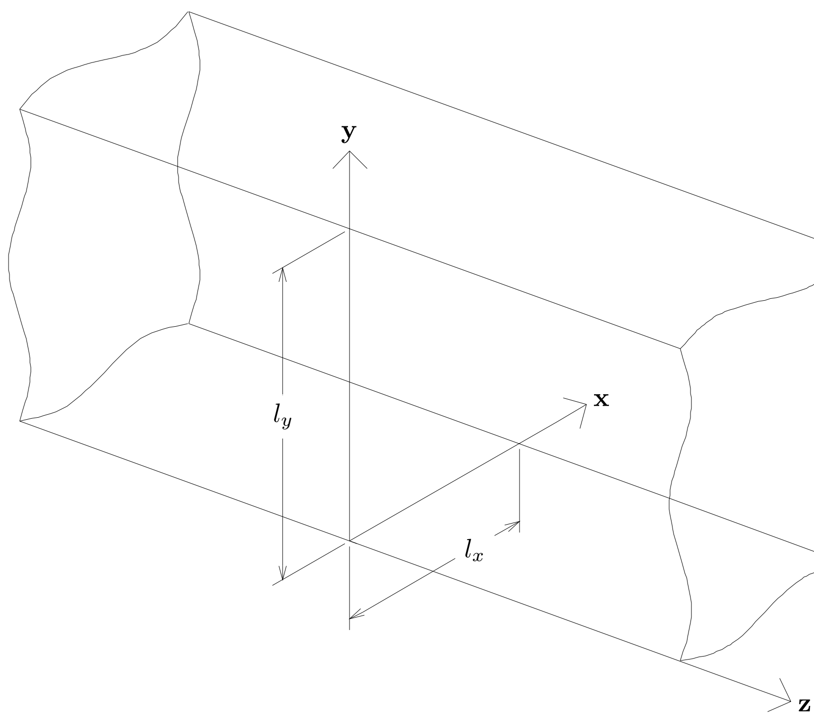

Figure 2.5. Duct with a rectangular cross-section.

The definition of the speed of sound (Equation 2.16) is then substituted into Equation 2.17,

$$\frac{1}{c_0^2}\frac{\mathbf{D}p}{\mathbf{Dt}} + \rho_0 \nabla \cdot \mathbf{u} = 0, \tag{2.19}$$

where c_0 is the speed of sound at average fluid properties (ρ_0, p_0, T_0, ...). Next the difference between the material derivative ($\mathbf{D}/\mathbf{Dt}$) of Equation 2.19 and the partial derivative ($\partial/\partial\mathbf{x}$) of Equation 2.18 with respect to space is taken which results in the convected 3-D wave equation,

$$\left(\frac{\mathbf{D}^2}{\mathbf{Dt}^2} - c_0^2\nabla^2\right) p = 0. \tag{2.20}$$

Expanding the material derivative and dividing by c_0^2,

$$\left(\frac{1}{c_0^2}\frac{\partial^2}{\partial t^2} + \frac{2\mathbf{M}}{c_0}\frac{\partial^2}{\partial t \partial \mathbf{x}} - (1-\mathbf{M}^2)\nabla^2\right) p = 0, \tag{2.21}$$

where $\mathbf{M} = \mathbf{u_0}/c_0$. By using the fact that $c_0 = \omega/k_0$, Equation 2.20 can be written in a more convent form,

$$\left(\frac{1}{\omega^2}\frac{\partial^2}{\partial t^2} + \frac{2\mathbf{M}}{\omega k_0}\frac{\partial^2}{\partial t \partial \mathbf{x}} - \frac{1-\mathbf{M}^2}{k_0^2}\nabla^2\right) p = 0, \tag{2.22}$$

where ω is the angular frequency and k_0 is the total wavenumber.

At this point the pressure field is going to written in a complex form and assumed to be separable in both time and space such that $\hat{p}(\mathbf{x}, t) = \hat{p}(x, y)\hat{p}(z)\hat{p}(t)$. The temporal solution is assumed to take the form

$$\hat{p}(t) = \exp\{j\omega t\}. \tag{2.23}$$

This results in the spatial component of the convecting wave equation

$$\left((1-\mathbf{M}^2)\nabla^2 - 2jk_0\mathbf{M}\nabla + k_0^2\right)\hat{p}(x, y)\hat{p}(z) = 0. \tag{2.24}$$

This can be further split into axial and cross-sectional components by splitting k_0 into components,

$$k_0 = \sqrt{k_{xy}^2 + k_z^2}, \tag{2.25}$$

and because the mean flow is only in the axial direction ($\mathbf{M} = M\hat{\mathbf{k}}$). The cross-sectional component is a typical Helmholtz equation

$$\left(\frac{\partial^2}{\partial x^2} + \frac{\partial^2}{\partial y^2}\right)\hat{p}_{xy}(x, y) + k_{xy}^2\hat{p}(x, y) = 0, \tag{2.26}$$

whos solution,

$$\hat{p}(x, y) = \Psi_m(x, y), \tag{2.27}$$

is one of infinity many eigen-function solutions with discrete wavenumbers, k_m. The axial component of the convecting wave equation,

$$(1-M^2)\frac{\partial^2\hat{p}(z)}{\partial z^2} - 2jk_0M\frac{\partial\hat{p}(z)}{\partial z} + k_z^2\hat{p}(z) = 0, \tag{2.28}$$

retains the total wavenumber in second term which means its solution will depend on the cross-sectional wavenumber value at cross-sectional mode. The solution to the axial convecting wave equation,

$$\hat{p}(z) = p_m^+ \exp\left\{-jk_{zm}^+ z\right\} + p_m^- \exp\left\{+jk_{zm}^- z\right\}, \tag{2.29}$$

has waves traveling in both directions with the axial wavenumber in each direction for a given mode

$$k_{zm}^{\pm} = \frac{\mp M k_0 + \sqrt{k_0^2 - (1 - M^2) k_m^2}}{1 - M^2}. \tag{2.30}$$

The solution for a three-dimensional acoustic wave in a duct with a constant but arbitrary cross-section in complex pressure is the combination of the component solutions presented in Equations 2.23, 2.27, and 2.29,

$$\hat{p}(x, y, z, t) = \Psi_m(x, y) \left(p_m^+ \exp\left\{-jk_{zm}^+ z\right\} + p_m^- \exp\left\{+jk_{zm}^- z\right\} \right) \exp\left\{j\omega t\right\}. \tag{2.31}$$

The two solutions for a plane wave ($\Psi_m = 1$, $k_m = 0$) traveling in a duct have a characteristic speed of $u \pm c_0$. Acoustic modes will travel indefinitly if $k_0^2 - (1 - M^2)k_m^2 > 0$ (the quantity inside of the square-root of Equation 2.30). This presents a frequency at which a given mode will cut-on,

$$f_{cuton} = \frac{c_0}{2\pi} \sqrt{(1 - M^2) k_m^2}. \tag{2.32}$$

Below this frequency, an acoustic mode will be exponentially attenuated as it travels throught the duct.

2.2.2.1 Characteristic Equations of Cross-Sections

In order to determine the characteristic equations of an acoustic field within a cross-section the solution to Equation 2.26 needs to be determined. A typical boundary condition that is used in the solution of this 2-D Helmholtz equation is using the assumption that the walls are rigid.

$$\nabla p_{x,y}(x, y) \cdot \mathbf{n}_{wall} = 0 \tag{2.33}$$

This boundary condition results in the acoustic waves being perfectly reflected off of the duct walls. There are several known empirical solution sets of the characteristic equations for specific geometry with the rigid wall assumption.

The first of these solutions is for a rectangular cross-section,

$$\Psi_{m,n}(x, y) = \cos(k_x x) \cos(k_y y), \tag{2.34}$$

where the wave numbers along each axis are $k_x = m\pi/l_x$ and $k_y = n\pi/l_y$. The duct has a width of l_x and a height of l_y. The total cross-sectional wave number for use in determining the axial wave

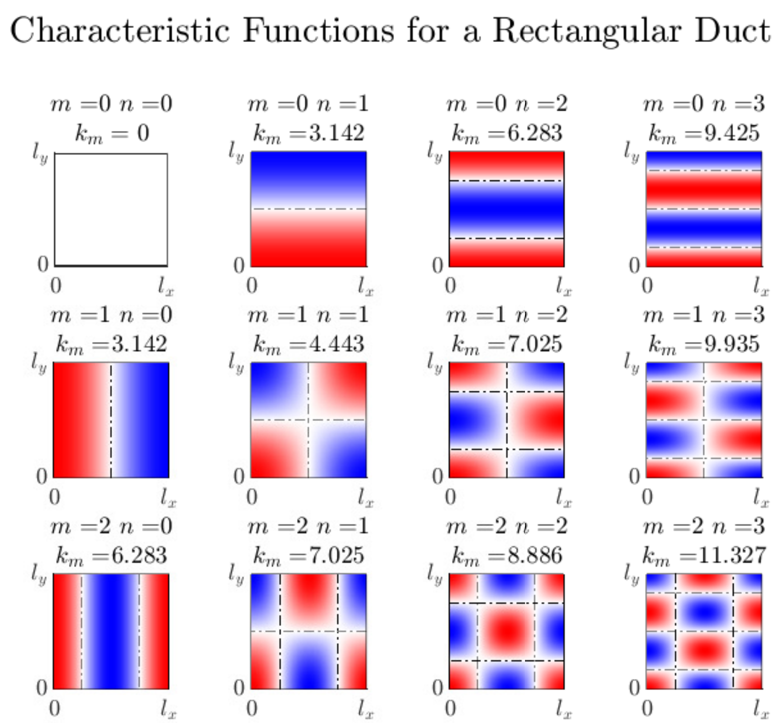

Figure 2.6. Characteristic solutions to Equation 2.26 with rigid wall in a rectangular cross-section where m=0:2 and n=0:3. Nodal lines are depicted by the dot-dash lines. The cross-sectional wave numbers, k_m, listed are for a duct of unit length and height.

numbers is

$$k_m^2 = k_x^2 + k_y^2. \tag{2.35}$$

Figure 2.6 shows the characteristic functions when m=0:2 and n=0:3 for a rectangular cross-section of width of l_x and height of l_y. The lines depicted in the figure are nodal lines and represent locations where there is zero pressure fluctuations for that acoustic mode.

The second set of known empirical solutions is for a circular cross-section with radius R,

$$\Psi_{m,n}(r,\theta) = J_m(k_{mn}r)\exp\{\pm jm\theta\}, \tag{2.36}$$

where J_m is the m^{th} Bessel function of the first kind and the $\pm$ indicates the direction of spin. If the left and right spin coefficients are equal in magnitude then a non-spinning mode is created. In order to satisfy the solid wall boundary condition $J_m'(k_{mn}R) = 0$ which determines a set of discrete values for the cross-sectional wave number at the n^{th} zero for the m^{th} Bessel function. Figure 2.7

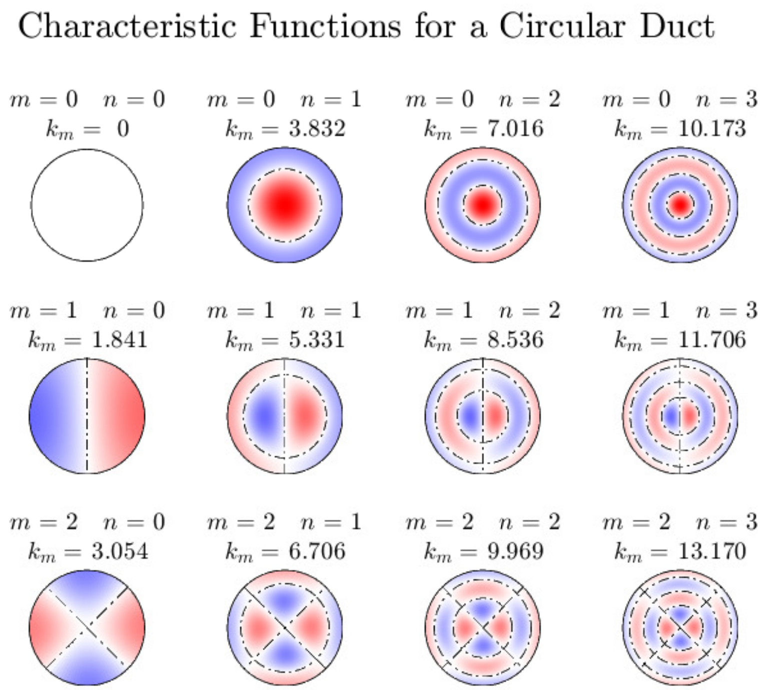

Figure 2.7. Characteristic solutions to Equation 2.26 with rigid wall in a circular cross-section where m=0:2 and n=0:3. Nodal lines are depicted by the dot-dash lines. The cross-sectional wave numbers, k_m, listed are for a duct of unit radius.

shows the characteristic functions for a circular duct.

CHAPTER 3

AERO-OPTICAL AND ACOUSTICAL COUPLING

- Mode marching method

Acoustic waves are isentropic compression waves with the fluctuating pressure, p', determining the strength of the wave. This fluctuating pressure is related to the sound pressure level, SPL by

$$\mathrm{SPL} = 20\log_{10}\left(\frac{p_{rms}}{p_0}\right) \tag{3.1}$$

where p_{rms} is the root mean square of the pressure fluctuation, and p_0 is the reference pressure (20 μPa for air). The pressure fluctuations can be converted to the density fluctuations via the definition of the speed of sound:

$$c_0^2 = \left(\frac{\partial p}{\partial \rho}\right)_s = \frac{p'}{\rho'} \tag{3.2}$$

where c_0 is the speed of sound at mean fluid properties and the subscript s denotes constant entropy. It can be shown by combining Equations 2.5 and 2.7 that the fluctuating density can be related to the OPD,

$$\mathrm{OPD} = K_{GD}\int_{s_1}^{s_2} \rho' ds. \tag{3.3}$$

This can be combined with Equation 3.2,

$$\mathrm{OPD} = \frac{K_{GD}}{c_0^2}\int_{s_1}^{s_2} p' ds, \tag{3.4}$$

to provide a way of computing the optical path difference of a pressure field.

3.1 Simulating an Optical Wavefront Measurement from an Acoustic Field Function

An optical wavefront can be simulated from a complex pressure field by applying Equation 3.4. To accomplish this, two separate coordinate systems will need to be defined. The first is the beam coordinate system, $\mathbf{x}_B$, that will have a measurement aperture, which is typically circular, defined in the xy-plane and propagates in the z-direction. The second is the acoustic coordinate system, $\mathbf{x}_A$, that will be defined based on the source location or the geometry that the acoustic waves are propagating through. These to coordinate systems will have a function representing a transform from one to the other

$$\mathbf{x}_A = R\mathbf{x}_B + T, \tag{3.5}$$

where R is a matrix which represents the rotation and T is a vector that represents the translation.

The important parameters for defining the aperture which the beam coordinate system is based are the aperture size, Ap, and the number of lenslets or sub-apertures, $N_{lenslets}$. Assuming that the aperture is either circular or square and the lenslet size and sub-aperture size is approximately $Ap/N_{lenslets}$, the x locations of the center of the sub-apertures go from $-Ap/2(1-1/N_{lenslets})$ to $Ap/2(1-1/N_{lenslets})$ by steps of $Ap/N_{lenslets}$ with the y locations having the same values. This gives a matrix representing both x_{Ap} and y_{Ap} that is $N_{lenslets}$ by $N_{lenslets}$. For the purpose of removing piston, tip, and tilt and creating a mask that represents the beam aperture, the radial coordinates, ρ_{Ap} and θ_{Ap}, of the aperture should also be calculated. A circular beam will have a mask defined by,

$$Mask_{Ap} = \begin{cases} 1, & \text{if } \rho_{Ap} \le Ap/2 \\ 0, & \text{otherwise.} \end{cases} \tag{3.6}$$

The beam coordinate frame is the aperture coordinates extruded in the z-direction over the range of desired z-values.

After the beam coordinates are transformed into the acoustic coordinates using Equation 3.5, the complex pressure field, $\hat{p}(x, y, z, t)$ can be calculated at the points that are within the optical beam. If the pressure field is separable into spatial and temporal components, than the integration along the beam length only needs to be done once for each temporal frequency,

$$\widehat{\mathrm{OPD}}(x, y) = \frac{K_{GD}}{c_0^2} \int_{z_1}^{z_2} \hat{p}(x, y, z)_{Ap} dz, \tag{3.7}$$

where $\widehat{\mathrm{OPD}}(x, y)$ is the complex optical path difference as measured in the aperture plane. If a complex density field is known instead, than Equation 3.7 becomes

$$\widehat{\mathrm{OPD}}(x, y) = K_{GD} \int_{z_1}^{z_2} \hat{\rho}(x, y, z)_{Ap} dz. \tag{3.8}$$

For the purposes of calculating temporally mean optical properties of simulated beam passing through a known complex pressure or density field a phase vector was defined, $\phi = [0, 2\pi)$. The measurable component as a function of phase is

$$\mathrm{OPD}(x, y, \phi) = \mathrm{REAL}\left[\widehat{\mathrm{OPD}}(x, y)\exp\{-j\phi\}\right], \tag{3.9}$$

or as a function of time for all temporal frequencies,

$$\mathrm{OPD}(x, y, t) = \mathrm{REAL}\left[\sum \widehat{\mathrm{OPD}}(x, y)\exp\{-j\omega t\}\right], \tag{3.10}$$

where there is a separate $\widehat{\mathrm{OPD}}(x, y)$ computed for each temporal frequency. One of the more important measurements that can be calculated from OPD is the spatial RMS, $\mathrm{OPD}_{\mathrm{RMS}}$, which is calculated at each time or phase step at the points where the aperture mask equals one.

3.2 Simple Examples of Acoustic-Optical Coupling

Two basic acoustic pressure fields will be numerically examined for their optical properties. The first will be a planar acoustic wave that will be numerically simulated over a variety of conditions. The second will be a spherical acoustic wave that will be both numerically simulated and validated experimentally.

3.2.1 Planar Acoustic Waves

A planar wave is the simplest solution to the wave equation and varies only in time and the direction of travel. A planar wave can be calculated from the set of solutions for duct acoustics, Equation 2.31, given that $\Psi_m(x, y) = 1$,

$$\hat{p}(z, t) = p_m \exp\left\{j(\omega t \mp k_{zm}^{\pm} z)\right\}. \tag{3.11}$$

This section will show several plots to show the effect that acoustic waves have on the optical wavefront of a planar wave with the general geometry shown in Figure 3.1. For the following example, l_n is the width of the acoustic disturbance (for example, the width of the wind tunnel), θ is the angle between the planar acoustic wave and the beam direction, A_p is the aperture diameter of the beam, and Λ is the wavelength of the acoustic wave.

Figure 3.2 shows the time averaged $\mathrm{OPD}_{\mathrm{RMS}}$ per meter of beam propagation when the beam path is parallel ($\theta = 0$) to the peaks and troughs of the planar acoustic wave as SPL is varied. As

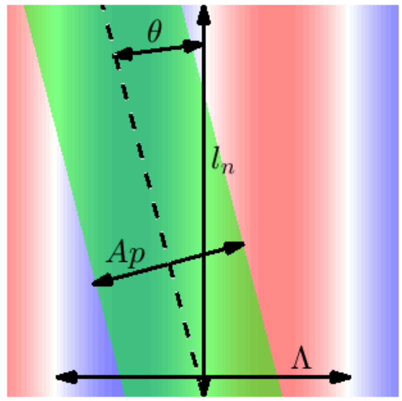

Figure 3.1. General geometry for various sample calculations for showing the acoustic-optical coupling effect.

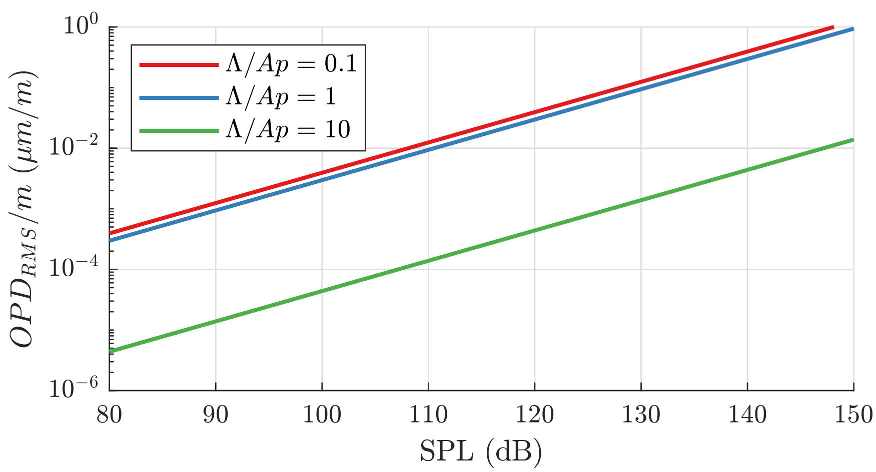

Figure 3.2. Theoretical time-averaged $\mathrm{OPD_{RMS}}$ per meter of beam propagation as a function of sound pressure level, SPL, for several Λ/Ap ratios and $\theta = 0$.

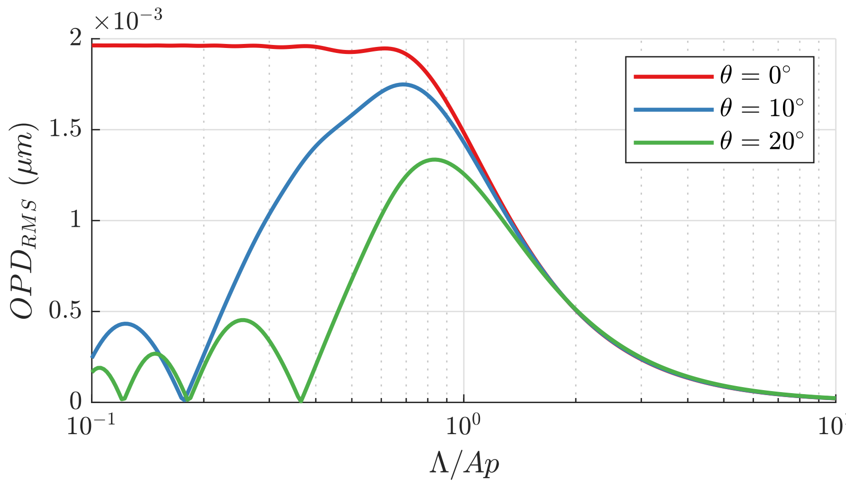

Figure 3.3. Theoretical time-averaged OPD_{RMS} for a rms sound pressure of 1 Pa (SPL of 94 dB), l_n of 1 m, and various angles and Λ/Ap ratios.

the sound pressure level increases the time averaged OPD_{RMS} also increases and can easily reach the point of being a significant factor in the measured optical disturbance. There is little difference between 0.1 and 1 Λ/Ap, but as the wavelength gets much larger compared to the beam diameter, then the optical effect of the noise is greatly reduced, this effect is known as aperture filtering [41].

Aperture filtering is more clearly shown in Figure 3.3. As the Λ/Ap ratio increases from 0.1, time-averaged OPD_{RMS} remains fairly constant until it starts to drop around Λ/Ap of 0.7 and starts to asymptotically approach zero which it basically reaches by Λ/Ap of 10. Figure 3.3 also shows the effect of changing the beam angle, θ, through the acoustic field. For nonzero θ, the beam encounters alternating high and low index of refraction as it passes through the test region, so that the time-averaged OPD_{RMS} begins to decrease compared to the $\theta = 0°$ case below $\Lambda/Ap = 1$. There are also points of zero optical disturbance that occur at $\theta_{zero} = \tan^{-1}(n\Lambda/l_n)$ for $n \neq 0$; these points occur because the peaks and valleys of the optical disturbance caused by the sound wave effectively cancel out over the length of the integration path, $l_n/\cos\theta$.

Figures 3.2 and 3.3 show the optical effect of plane acoustic waves in a no-flow environment. The effect of wind-tunnel flow is to stretch (downstream-traveling waves) or compress (upstream-traveling waves) the wavelength of the acoustic noise thereby altering the filtering effect of the beam aperture. Figure 3.4 shows a typical optical disturbance from the two transverse acoustic waves (u+c and u-c) present in a wind tunnel at Mach 0.6. Both waves have a RMS sound pressure of 1 Pa and the beam has an aperture of 15 cm and propagates through a 1 m acoustic field

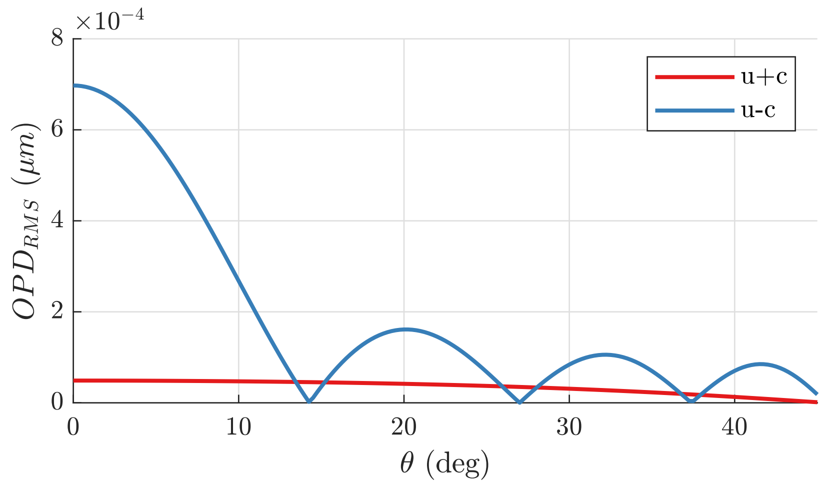

Figure 3.4. Theoretical time-averaged $\mathrm{OPD_{RMS}}$ for the two acoustic waves (u+c and u-c) for the blade pass frequency (534 Hz) at Mach 0.6 with a RMS sound pressure of 1 Pa (SPL of 94 dB), l_n of 1 m, and Ap of 15 cm.

inside the tunnel. Over a vast majority of the look back angles the upstream-traveling acoustic wave has a much greater effect on the optical disturbance compared to the downstream-traveling acoustic wave, due to the much shorter wavelength of the upstream-traveling waves which is less affected by aperture filtering. However, the upstream-traveling wave goes through several zero points so the downstream-traveling wave dominates at some look back angles.

3.2.2 Spherical Acoustic Waves

The acoustic field from an speaker maybe assumed to be a spherical wave from a pulsating point if the frequency is sufficiently low and measurement region is far enough away from the source [37]. This pressure field when converted to complex pressure is represented by

$$\hat{p}(r,t) = \frac{A_0}{r} \exp\left\{-j(kr - \omega t)\right\}, \tag{3.12}$$

where A_0 is the fluctuating pressure strength and r is the distance from the source to the measurement point. The RMS pressure of this field can be represented by

$$p_{rms} = \frac{|A_0|}{r\sqrt{2}}. \tag{3.13}$$

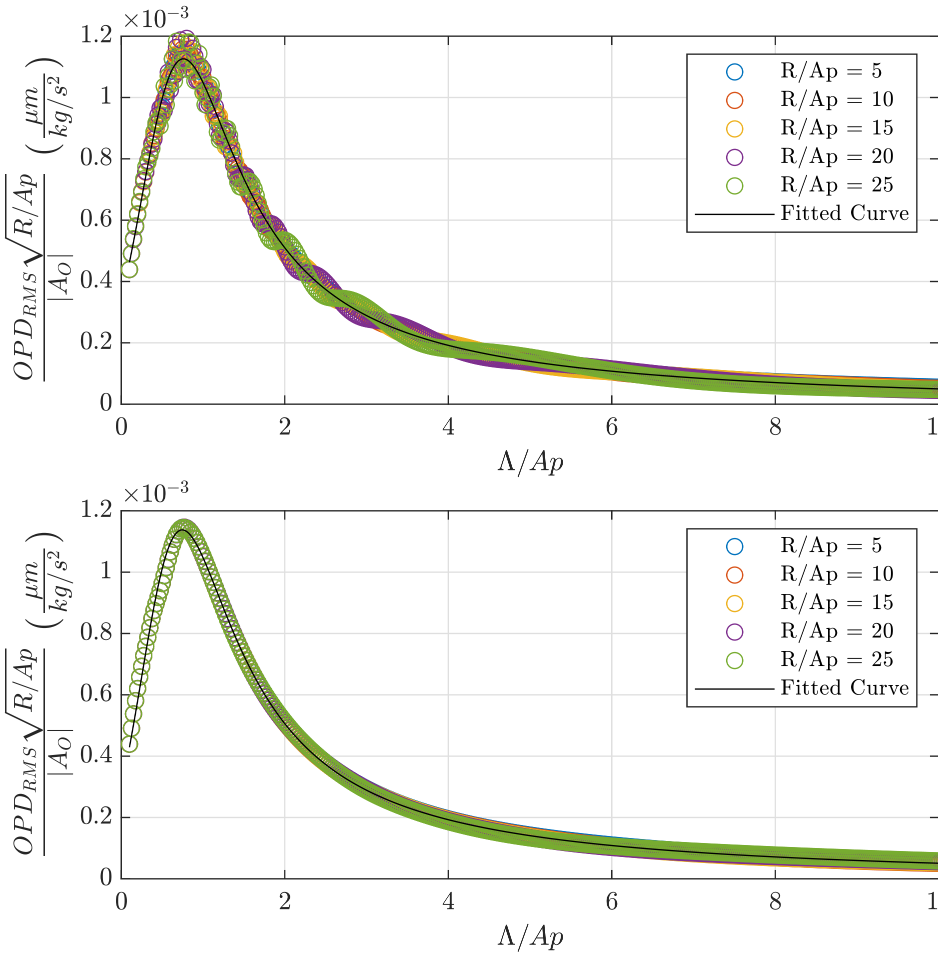

Figure 3.5. Theoretical time-averaged $\mathrm{OPD_{RMS}}$ for a spherical acoustic wave. The top plot shows a perfect spherical acoustic signal integrated over ±5-m. The bottom plot shows has a Tukey window applied along the beam length to partially emulate source directivity which significantly reduces the measured oscillations.

3.2.2.1 Theoretical OPD Measurements

A set of optical properties where calculated for a beam passing through a spherical acoustic field as defined by a point source using the process described previously in Chapter 3.1. These calculations used an circular aperture size of 0.25-m in diameter consisting of 32x32 sub-apertures, an acoustic wavelength, Λ, of $Ap/4$ to $10Ap$, and a distance from the point source to the center of the aperture, R, of $5Ap$ to $25Ap$. The beam was integrated over ±5-m from the plane of the point source with 25 phase step used to calculate mean values.

The result of these simulated acoustic fields is shown in Figure 3.5. The top plots shows the expected optical disturbance ratio, $\mathrm{OPD_{RMS}}/|A_0|$, for a perfectly spherical acoustic field measured

TABLE 3.1

CURVE FIT VALUES FOR FIGURE 3.5 AND EQUATION 3.14

Coefficent	Value
p_1	-1.845e-05
p_2	4.769e-04
p_3	4.520e-03
p_4	1.435e-03
q_1	5.399e+00
q_2	-5.145e+00
q_3	4.869e+00

over the beam length. With the exception of some oscillations that are caused by end effects in the integration. The oscillations can be greatly reduced by using a windowing function in the z-direction such as a Hanning or Tukey window which also can be used to roughly model directivity of the speaker's acoustic emission as shown in the bottom plot. While this plot was calculated with a single aperture diameter, the general trend holds for all other aperture diameters that were tested, the only effect was the size and width of the oscillations.

The peak of the optical disturbance ratio, $\mathrm{OPD}_{\mathrm{RMS}}/|A_0|$, is located at $\Lambda/Ap \approx 0.75$ for a circular aperture. The signal is reduced above this value due to aperture filtering and below this value because the shorter wavelength have a reduced distance before alternating high and low index-of-refraction regions reduce the optical path difference. When the acoustic source point is sufficiently far enough away from the measurement beam, $R/Ap \geq 2$, the optical disturbance ratio, $\mathrm{OPD}_{\mathrm{RMS}}/|A_0|$ when multiplied by $\sqrt{R/Ap}$, can be collapsed onto a single curve for a range of Λ/Ap of 0.1 to 10. Above $\Lambda/Ap = 10$ the curves start to diverge away from one another. An approximate function fit to this data is

$$\frac{\mathrm{OPD}_{\mathrm{RMS}}\sqrt{R/Ap}}{|A_0|} \approx \frac{p_1(\Lambda/Ap)^3 + p_2(\Lambda/Ap)^2 + p_3(\Lambda/Ap) + p_4}{(\Lambda/Ap)^3 + q_1(\Lambda/Ap)^2 + q_2(\Lambda/Ap) + q_3} \tag{3.14}$$

with coefficient values shown Table 3.1. This functional fit has a R^2 value of 0.9991.

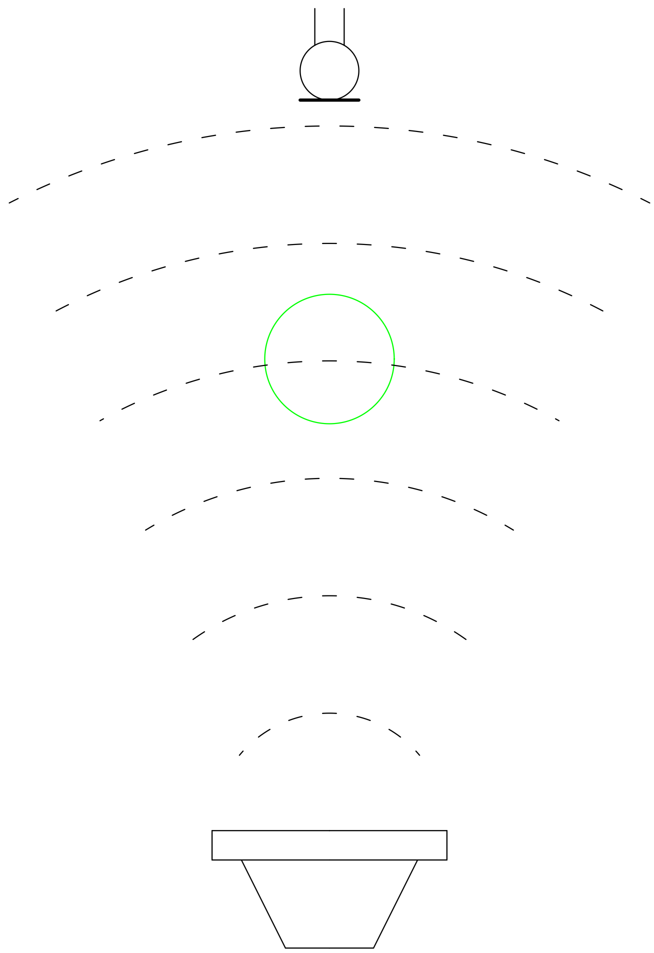

Figure 3.6. Spherical acoustic wave measurement test.

3.2.2.2 Measurement of a Spherical Acoustic Wave with an Optical Beam

A small bench top experiment was used to compare the simultaneous optical and microphone measurements of an acoustic field from a speaker as shown in the measurement plane in Figure 3.6. The distance from center of the beam to the speaker was 102-mm with a beam diameter of 28-mm. An ACO model 7016B microphone [11] was placed directly over the speaker at a distance of 158-mm and was used with a Brüel & Kjær model 2670 preamplifier [6]. The speaker in use was Peerless model XT25SC90-04 [35] which has a fairly flat on-axis response from 1-kHz to 40kHz.

The wavefront measurements system utilized in these measurements is similar to that shown in Figure 2.4 except there was no primary telescope. The speaker was located in the center of the measurement region which was about 2-feet in length and the re-imaging telescope reduced

TABLE 3.2

COMPARISON OF MICROPHONE AND WAVEFRONT COMPUTATION OF $|A_0|$

$f_{speaker}$ (Hz)	$V_{speaker}$ (mV)	p_{rms} (Pa)	OPD$_{RMS}$ (μm)	$\lvert A_0\rvert_{mic}$ (kg/s^2)	$\lvert A_0\rvert_{wf}$ (kg/s^2)	Diff (%)
9000	100	5.65	6.545e-04	1.26	1.55	20.38
9000	250	12.23	1.421e-03	2.73	3.36	20.56
9000	500	19.52	2.386e-03	4.36	5.64	25.62
14000	1250	5.20	6.831e-04	1.16	1.18	1.24
14000	250	9.33	1.230e-03	2.09	2.12	1.50
14000	375	9.68	1.272e-03	2.16	2.19	1.16
18000	125	3.73	4.987e-04	0.83	0.84	1.10

the beam diameter by a factor of two and re-imaged the return mirror. Optical wavefronts and microphone measurements were taken at 49-kHz. The speaker was sinusoidally excited at three different frequencies (9, 14, and 18-kHz) at a variety of voltages.

The absolute value of the fluctuating pressure strength, $|A_0|$, was calculated two different ways. The power spectra of the microphone data was used to calculate the average p_{rms} at the excitation frequency and the fluctuating pressure strength using Equation 3.13. The optical wavefront was band-pass filtered at the excitation frequency using a process that will be discussed in Chapter **??**. The time averaged OPD$_{\mathrm{RMS}}$ was used to calculate the fluctuating pressure strength using Equation 3.14.

The results of these measurements of the fluctuating pressure strength is shown in Table 3.2. The differences between the two techniques for measuring the fluctuating pressure strength fell into two groups. For the 9-kHz cases, the differences ranged from 20-26% while the higher frequency cases the differences were between 1.1-1.5% and in all cases the wavefront measurement reported a higher fluctuating pressure strength. With the exception of the highest excitation case at 9-kHz, the differences between the to techniques was fairly constant for each frequency group. Some of these differences maybe attributable to the frequency response of the microphone.

Measured and simulated wavefronts for the highest excitation cases at each frequency are shown in Figure 3.7. The 9-kHz case shows some anomalies on the measured wavefront on the right

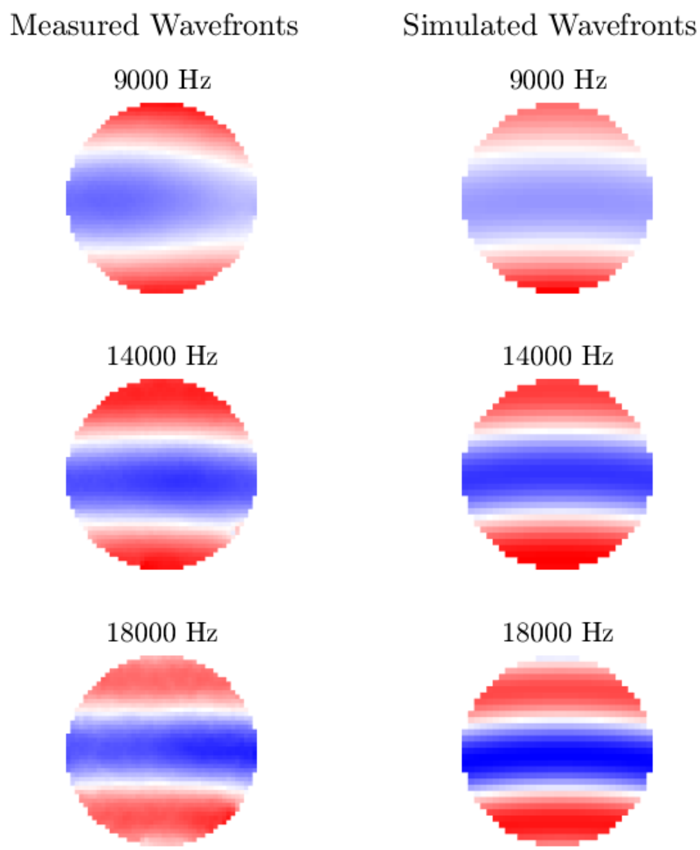

Figure 3.7. Comparison of some of the measured wavefronts and simulated ones.

side, deviating from spherical wave significantly likely contributing the significantly higher estimated pulsating field strength value when compared to the microphone estimate. The 14 and 18-kHz cases show some remarkable agreement between the measured and simulated images. Optical wavefront measurements can be utilized for making non-intrusive acoustic field measurements espically when the acoustic field is simple.

3.3 Estimating the Acoustic Field Inside the Test-Section

3.3.1 Mode Marching Process

1. Start with a known or assumed source acoustic field, $p^n(x, y)$
2. Calculate the transmitted pressure ratio
   - Traveling with subsonic flow

$$\frac{p^t}{p^i} = \left(\frac{1 + M_n}{1 + M_{n+1}}\right)\left(\frac{2M_{n+1}}{M_n + M_{n+1}}\right)\left(\frac{X_{n,n}}{X_{n,n+1}}\right)\left(\frac{X_{n,n}}{X_{n+1,n+1}}\right)^{1/(\gamma-1)} \tag{3.15}$$

   - Traveling against subsonic flow

$$\frac{p^t}{p^i} = \left(\frac{1 - M_n}{1 - M_{n+1}}\right)\left(\frac{2M_{n+1}}{M_n + M_{n+1}}\right)\left(\frac{X_{n,n}}{X_{n,n+1}}\right)\left(\frac{X_{n,n}}{X_{n+1,n+1}}\right)^{1/(\gamma-1)} \tag{3.16}$$

   - Where

$$X_{a,b} = 1 + \frac{\gamma - 1}{2} M_a M_b \tag{3.17}$$

3. March acoustic field to next axial step,

$$p^{n+1}(x, y) = p^n(x, y)\frac{p^t}{p^i}\exp\{j(\omega t \mp k_{zm}^{\pm} z)\} \tag{3.18}$$

4. Best-fit set of local duct modes coefficients, C_m, to acoustic field $p^{n+1}(x, y)$
5. Calculate new acoustic field from duct mode and repeat from step 2

$$p^n(x, y) = \sum_{m=0}^{M} C_m \cdot p_m(x, y) \tag{3.19}$$

6. When the end point is reached, step inlet acoustic field (rotate fan) and repeat

CHAPTER 4

MULTIDIMENSIONAL SPECTRAL ESTIMATION OF OPTICAL WAVEFRONTS

As described in Chapter 1, the objective of this research is to develop methods to evaluate and, if possible, eliminate the effect of facility-related acoustic noise on aero-optical measurements. As such, the first goal of the research is to establish analytical methods to identify and isolate acoustic sources of optical signals within a given data sample. This is a significant challenge since, as will be shown later, acoustic sources of optical aberrations typically have a magnitude and frequency content that is in the same range as the signal that is the objective of the measurement. This chapter will begin with a brief overview of some of the benefits to analyzing multidimensional data in this way, followed be a short discussion on how these spectrum are calculated, and conclude with a more in depth discussion on the analysis of multidimensional spectral estimates.

The multi-dimensional spectral approach that is employed throughout this research helps identify and characterize acoustic sources of optical noise as well as aero-optical signals. The spectral approach is also used as the basis for methods to filter the acoustic sources. For measurements in multiple dimensions, such as a line of sensors that are recorded over time, a multidimensional spectral estimation not only produces temporal frequency content but can also be used to identify the direction and speed of travel of a particular wave. The benefits of using multidimensional spectral estimation are shown in Figure 4.1. A single row of sub-apertures was from an optical wavefront measurement with a 5-inch diameter beam propagating normally through a wind-tunnel test section with a free-stream Mach number of 0.5. This measurement was preformed in the University of Notre Dame Whitefield Wind Tunnel in a test section that contained a model representing the fuselage of the AAOL aircraft [21] with window that was flat and flush to the outer mold line of the fuselage. The top plot shows a traditional power spectrum ensemble-averaged over the row of data. Both the blade-passing frequency (517-Hz) and its sub-harmonic had similar amplitudes with an additional five harmonics showing significant spikes above the local baseline measurement. There are three additional strong peaks at approximately 3100, 4850, and 5850 Hz that are likely due to additional fan vibration that is currently limiting the top speed of the tunnel.

Both the middle and bottom plots show the multidimensional spectral estimation plot of two-

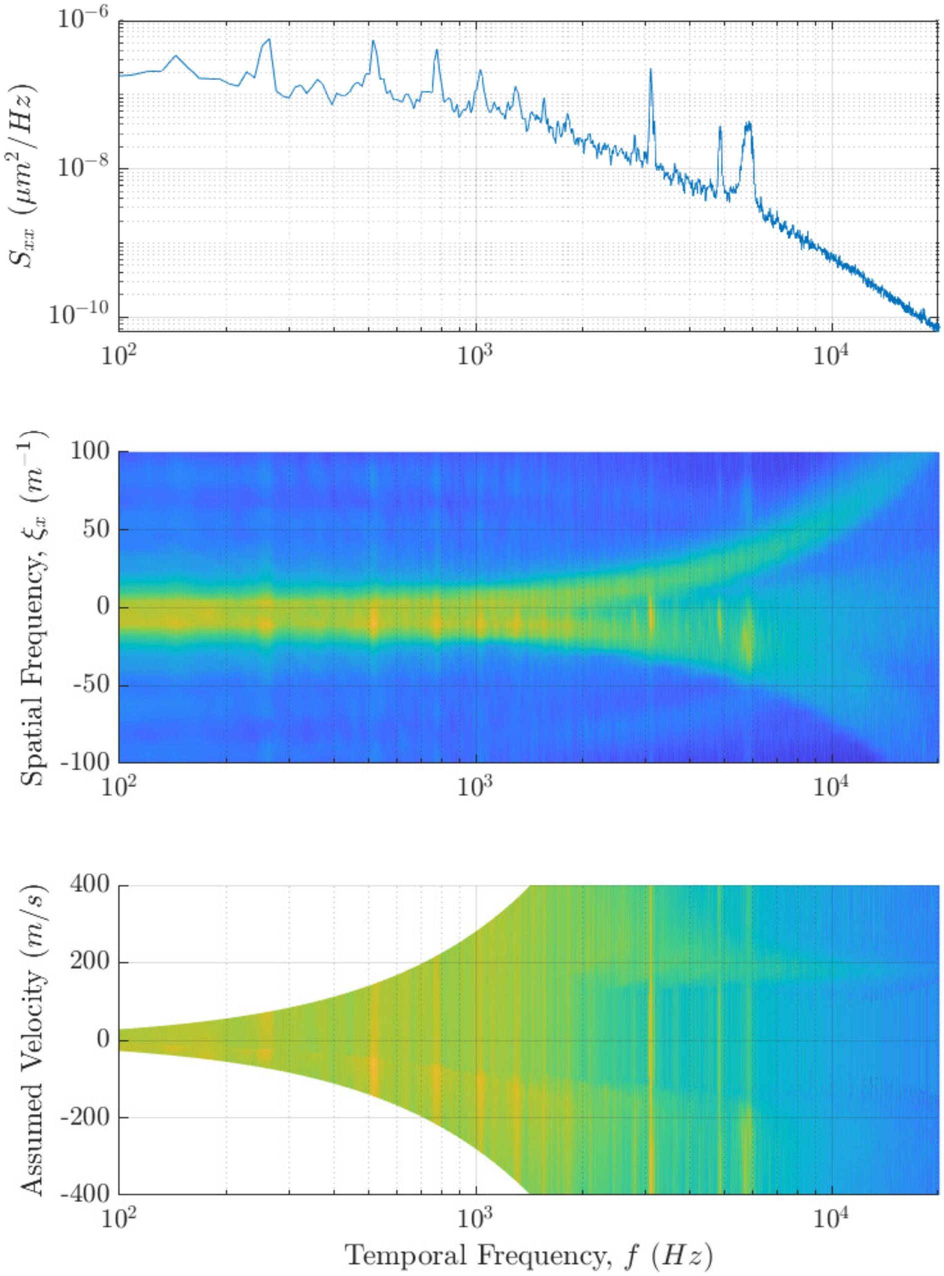

Figure 4.1. Multidimensional spectral estimation plot example and comparison to traditional power spectrum measurements. A single row of an optical wavefront measurement was used in this example. The top plot shows the typical power spectrum averaged over the entire row of data. Both the middle and bottom plots show the multidimensional spectrum plot with the y-axis as spacial-frequency in the middle and velocity in the bottom assuming $u = f/\xi_x$.

dimensional measurement. The colorbars were intentionally not shown in order to allow for all three plots to be aligned in the temporal-frequency axis and the color is representative of the logarithm of the power or variance in the wavefront signal (i.e. $\mathrm{OPD_{RMS}}^2$) with yellow representing more power and blue representing less. The colorbar range in this plot is the same is constant with the other plots throughout this chapter. In the middle plot the y-axis represents the stream wise spatial frequency, ξ_x with the units of inverse meters. It is important to note that, unlike temporal-frequencies, spatial-frequencies can have positive or negative values depending on the direction of travel of the disturbance; this means that, waves with positive spatial-frequencies are moving in the direction of flow. The upstream and downstream traveling signals begin to diverge at around 2000-Hz with the signal below that point primarily laying on the upstream traveling side of the plot. The blade-passing frequency and its various harmonics can also be discerned in the center plot, by the vertical "streaks" that line up with the peaks in the standard spectrum shown in the top plot; the center spectral plot shows that these fan blade-passing signals have significant broadband spatial-frequency content. All of these narrow-band signals have a majority of their signal traveling upstream. In addition to optical disturbances branching off in the upstream and downstream moving directions there are significant disturbances along zero spatial-frequency representing a collection of standing waves. Elsewhere in this paper the multidimensional spectral estimation will be plotted with the temporal-frequency axis linearly. This data has been plotted logarithmically along the temporal-frequency axis to better slow the low frequency content. When plotted linearly, the two primary upstream and downstream traveling signals lay in a straight line.

A dispersion analysis can be performed on these multidimensional spectral estimates. In order to obtain the velocity of a given wave we can start with the most basic forms of the wave equation,

$$\hat{y} = a \exp\{j\theta\}, \tag{4.1}$$

where θ is the phase of the wave and equal to $kx - \omega t$. From here we can take the partial of θ with respect to time and set it equal to zero,

$$\frac{\partial \theta}{\partial t} = 0 = \frac{\partial k}{\partial t}\frac{\partial x}{\partial t} - \frac{\partial \omega}{\partial t}\frac{\partial t}{\partial t}, \tag{4.2}$$

which can be rearranged to

$$u = \frac{\partial \omega}{\partial k} = \frac{\partial f}{\partial \xi}. \tag{4.3}$$

If we are to assume that a wave packet intercepts the origin ($f = \xi = 0$) then every point on the spectral plot can be labeled with an assumed velocity,

$$u_{assumed} = \frac{f}{\xi_x}. \tag{4.4}$$

The bottom plot shows the same multidimensional spectral estimation plot as the middle one but with the y-axis representing an assumed velocity. There is not much in the way of velocity measurement capability at low temporal-frequencies The primary optical disturbance moving in the direction of flow is moving at the free-stream velocity of approximately 175-m/s. The upstream traveling disturbance is traveling at the same speed but due to the signal being broader is more difficult to measure this way. The stationary modes in the middle plot are nowhere to be found on the bottom plot. When the assumed velocity for this these waves is calculated their speed approaches infinity.

4.1 One-Dimensional Power Spectrum Calculation

Power spectral analysis is typically performed on one-dimensional data sets, for example, a single sensor measurement over time. On the other hand, if a sensor array were used, a multi-dimensional power spectrum could be computed that would also show spatial frequency information at each instant in time. For a single-point measurement that varies in time, $x(t)$, the power spectrum calculation is

$$S_{xx} = \frac{|\,\mathrm{FFT}\{x(t)\}|^2}{N f_s}, \tag{4.5}$$

where FFT is the Fast Fourier Transform, N is the number of samples, and f_s is the sample rate [3]. For data that has only a real component the Fast Fourier Transform function produces magnitude and phase relations at each frequency step, f_s/N, over the range from zero-frequency up to but not including the Nyquist frequency, f_s/w, with a mirrored set of data that can be represented either below (starting at $-f_s/2$) or above (ending just below f_s) this range. The Nyquist frequency not being included and the mirrored data is due to an assumption that is integral to the Fourier Transform, which is that the signal is assumed to be periodic.

The total energy, σ^2, of the signal must be preserved through the transform from physical space-time to frequency space

$$\sigma^2 = \frac{\sum x^2(t)}{N} = \Delta f \sum S_{xx}(f). \tag{4.6}$$

Additionally, because of the periodic nature of the Fourier Transform and a finite sample length of discrete data, spectral leakage can cause the power in one frequency bin to leak into adjacent frequency bins. To minimize this spectral leakage, windowing functions are employed which typically force the end points of the signal to zero. The Hann window,

$$w(t) = 1/2\left[1 - \cos\left(\frac{2\pi t}{T}\right)\right], \tag{4.7}$$

is one of the more commonly used windowing functions [5] where $w(t)$ is the window function, t is the time at a given sample, and T is the total sample time. Since the windowing of a data set changes the signal energy some correction is needed to be applied. For an arbitrary windowing function the correction factor, c_w, can be obtained by substituting the windowing function in place of $x(t)$ in Equation 4.6,

$$c_w = \frac{1}{\sqrt{\sum w^2(t)/N}}. \tag{4.8}$$

For a Hann window this correction factor approaches $\sqrt{8/3}$ as N goes to infinity. When Equation 4.5 is combined with a windowing function and associated correction the double sided power spectra equation in one dimension becomes

$$S_{xx} = \frac{|c_w\, \mathrm{FFT}\{x(t)w(t)\}|^2}{N f_s}. \tag{4.9}$$

A simple MATLAB function for computing the power spectrum of a one-dimensional signal with an arbitrary windowing function is shown in Appendix A.1.

4.2 N-Dimensional Power Spectra Calculation

For measurements with multiple spatial and temporal dimensions the Fast Fourier Transform is applied n-times where n is the total number of dimensions, with each application in a different dimension,

$$\mathrm{FFT_n}(x) = \mathrm{FFT}(\mathrm{FFT}(\cdots \mathrm{FFT}(\mathrm{FFT}(x,1),2)\cdots, n-1), n), \tag{4.10}$$

where $\mathrm{FFT}(x,n)$ is the Fast Fourier Transform of x in the n^{th} dimension [2]. For a n-dimensional array the operation becomes [29]

$$\mathbf{S_{xx}} = \frac{|c_w\, \mathrm{FFT_n}\{f(\mathbf{x})w(\mathbf{x})\}|^2}{\prod \overrightarrow{N}\overrightarrow{f_s}}, \tag{4.11}$$

where $\mathbf{S_{xx}}$ is the n-dimensional power spectra array or dispersion array, $f(\mathbf{x})$ is a n-dimensional set of data, $w(\mathbf{x})$ is a n-dimensional windowing function, $\overrightarrow{N}$ is a vector denoting the number of elements in each dimension, $\overrightarrow{f_s}$ is a vector denoting the sample rate in each dimension, and

$$c_w = \frac{1}{\sqrt{\sum w^2(\mathbf{x}) / \prod \overrightarrow{N}}}. \tag{4.12}$$

The signal energy conservation relationship becomes

$$\sigma^2 = \frac{\sum \mathbf{x}}{\prod \overrightarrow{N}} = \prod \overrightarrow{\Delta f_s} \sum \mathbf{S_{xx}}, \tag{4.13}$$

where $\overrightarrow{\Delta f_s}$ is a vector representing the frequency step sizes in each dimension. A simple MATLAB code for calculating the dispersion of x with an arbitrary windowing function is shown in Appendix A.2.

4.3 Non-Rectangular Spatial Windows

For n-dimensional data sets that fill a rectangular array, a windowing function can be created by multiplying together a series of one-dimensional windowing functions in the direction of each dimension. For non-rectangular data sets, such as is often the case with optical wavefront measurements, a windowing function can take some additional steps in its construction. In cases when the spatial measurement locations are constant throughout time, the windowing function can be split into two separate components,

$$w(\mathbf{x}) = w_t(t) \cdot w_s(x, y), \tag{4.14}$$

the temporal windowing function, $w_t(t)$, and the spatial windowing function, $w_s(x, y)$. This study uses a Hann window for the temporal windowing function and a modified Hann window for the spatial windowing function. For the case of a perfectly circular aperture, the Hann window can be reformulated to be based on the normalized radius, ρ_N, of the aperture,

$$w_s(\rho_N) = \begin{cases} \frac{1+\cos(\pi \cdot \rho_N)}{2} & \text{if } \rho_N < 1 \\ 0 & \text{otherwise.} \end{cases} \tag{4.15}$$

This modified Hann window is two-dimensional with a value of one at the center of the aperture and decreases to zero at the edge of the aperture in the same manner as a Hann windows decreases from the center to either end.

Because the wavefronts measurements often had a clipped edge or some other obscuration, a different method was employed in this study. For an arbitrary shaped aperture, the minimum distance from any given measurement location to the edge of the aperture was used to create the spatial windows. The minimum distance can be computed given the a set of points (x and y) that spans the measurement range and the set of points outside of the aperture (x_O and y_O),

$$d_{min}(x, y) = \min\left\{\sqrt{(x - x_O)^2 + (y - y_O)^2}\right\}. \tag{4.16}$$

This distance is then normalized by the maximum value and the resulting spatial window given a modified Hann window,

$$w_s(x, y) = \frac{1 + \cos\left\{\pi \cdot (1 - d_{min}^{norm}(x, y))\right\}}{2}. \tag{4.17}$$

This same basic idea can be extended to data sets where the locations of measurements in space vary with time.

4.4 Wavefront Multidimensional Spectrum

At the beginning of this chapter a multidimensional spectral plot for data resolved in time and one spatial dimension was shown along with a typical power spectrum plot in Figure 4.1. This was shown to facilitate a simple discussion of some of the benefits of using multidimensional spectrum analysis on optical wavefronts. That simple analysis was performed on only a single row of a wavefront data set and provided an insight into the disturbances that were moving in the horizontal (stream wise) direction only. When multidimensional spectral estimation is performed over all dimensions of a wavefront (i.e. time and both spatial dimensions), as will be done for the remainder of this chapter, additional detail is available, that also enables the determination of optical disturbances moving vertically (i.e. cross-stream to the flow) or any direction in between. Figure 4.2 shows a comparison between the two-dimensional single row spectrum and a three-dimensional spectral slice showing the horizontal moving optical disturbances at both zero-vertical spatial frequency and integrated through the vertical spatial frequencies in order to obtain the two-dimensional spectrum. The top plot shows the three-dimensional spectral estimation plot at $\xi_y = 0\ m^{-1}$, which shows planar waves traveling in the horizontal direction. The middle plot shows the three-dimensional spectrum integrated through the vertical spatial-frequency axis creating an estimate of the two-dimensional

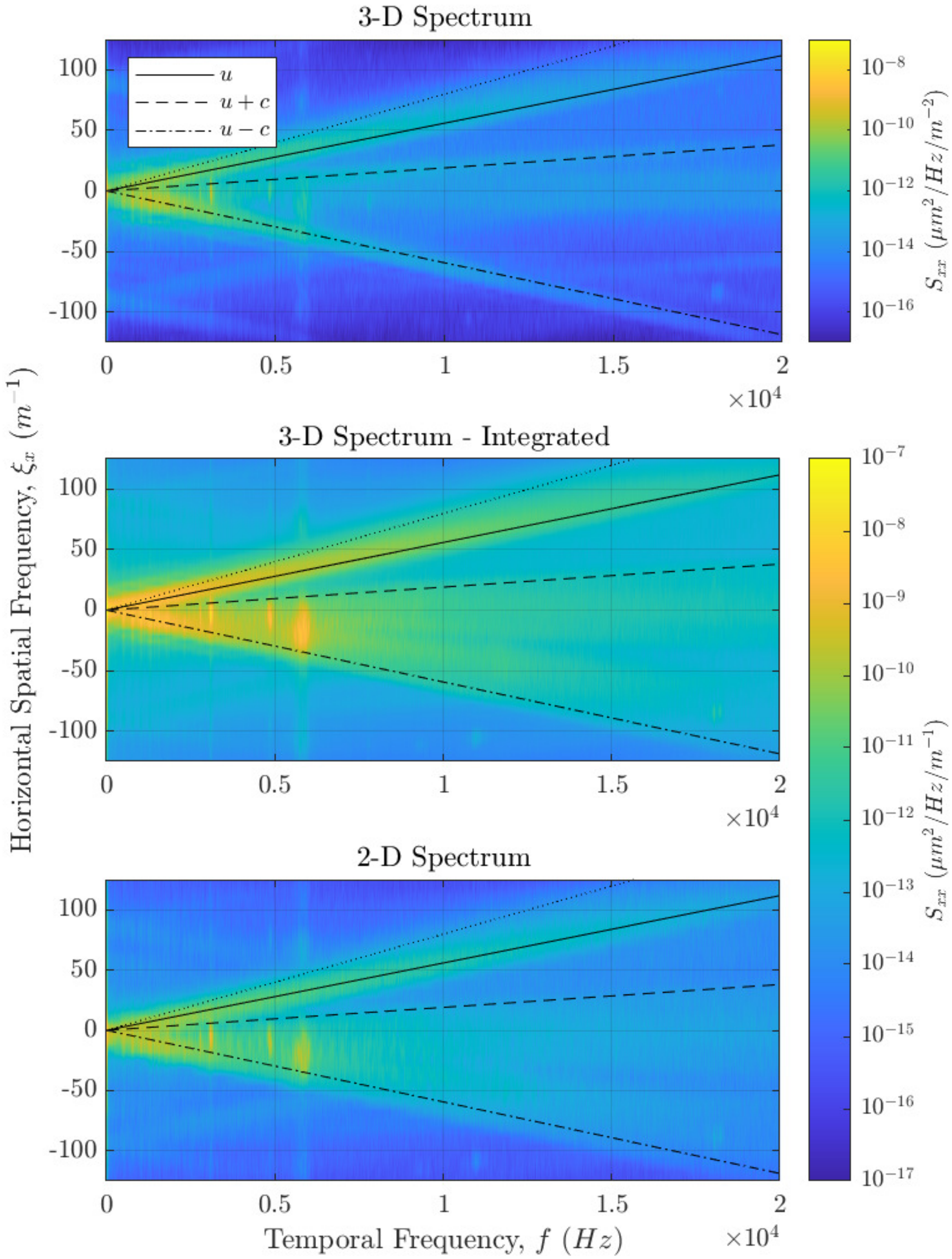

Figure 4.2. Horizontal moving optical disturbances comparison. The top plot shows a slice of the three-dimensional spectrum focusing on the plane waves that are traveling in the horizontal direction. The middle plot is a recreation of the two-dimensional spectrum by integrating through the the vertical spatial-frequencies. The bottom plot is the two-dimensional spectrum.

spectrum. The bottom plots shows the two-dimensional spectral plot that was previously shown in Figure 4.1 but this time with a linear temporal-frequency axis. Both of the two-dimensional spectrum whether directly computed or integrated show a significant increase in the signal content between the acoustic lines ($u \pm c$).

The three-dimensional spectral slice shows signal at the same limits characteristic velocity limits of the free-stream velocity, u, and the acoustic lines, $u \pm c$, as the two-dimensional spectrum of signal along with some signal laying along the temporal-frequency axis at $\xi_y = 0\ m^{-1}$. This signal represents a collection of stationary modes at each temporal-frequency. If this were a flow-related phenomenon the velocity of the disturbance according to Equation 4.4 would be near infinity; as such, it is more likely caused by mechanical vibration of the wind tunnel and components of the optical measurement system. On the three-dimensional spectrum plot there are signals that run parallel to u and $u - c$ that do not emanate origin but from $\xi_x \approx \pm 80\ m^{-1}$ that show the assumed velocity is not always valid. I can't think of a good explanation for these other than some mean lensing feature that is both convecting and traveling at $u - c$ and maybe $u + c$. Could be a ghost beam at a different magnification. There is also an aliased signal that runs parallel to $u + c$ starting at $\xi_x \approx -50\ m^{-1}$ and decaying towards the left. Aliased signals are due to the sample rate, either spatial or temporal, being to low.

The middle plot of Figure 4.2 shows the integrated spectrum through vertical spatial-frequency axis which effectively recreates the two-dimensional spectrum plot. A reduced order spectrum can be calculated by

$$S_{xx}^{n-1} = \int S_{xx}^{n} df_s^m, \tag{4.18}$$

where S_{xx}^n is the n-dimensional spectrum and df_s^m is the differential frequency in the m-th dimension. This can also be shown in Figure 4.3. While the integrated signal over estimated the spectrum going from three-dimensions to two in Figure 4.2, it under estimated the spectrum going from two to one dimensions. Unfortunately, due to the limited number of spatial sample points and the large dynamic range of the signal, this integrated value can contain a significant of error.

Due to the the signal being relatively sparse, a reduced order spectrum can be estimated by

$$S_{xx}^{n-1} \approx \max(S_{xx}^{n}, m) f_s^m, \tag{4.19}$$

where $\max(S_{xx}^n, m)$ is the maximum value of the spectrum along dimension m and f_s^m is the sample rate for that dimension. The calculated temporal power spectrum from the two-dimensional spec-

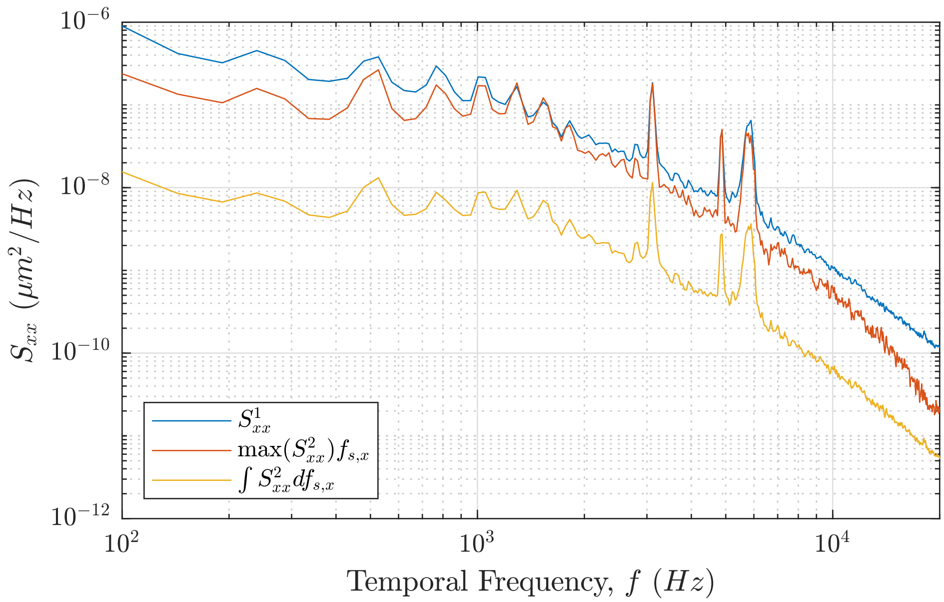

Figure 4.3. Recovery of time-based power spectrum from two-dimensional spectral estimate.

trum using the maximum value is a good estimation at the center of the frequency range but has some additional decay at both low and high frequencies. The calculated reduced order spectrum appears to follow the functional form of actual spectrum but with a significant offset.

4.4.1 2-D Slices of the Multidimensional Spectral Estimation

The full multidimensional spectrum contains information of flow features that are not only moving in the horizontal direction as the two-dimensional dispersion showed but also in every direction of the two-dimensional optical wavefront. Figure 4.4 shows two-dimensional slices of the full spectrum that on the top show the horizontal (stream wise) moving disturbances at $\xi_y = 0\ m^{-1}$ and on the bottom show the vertical (cross-stream) moving disturbances at $\xi_x = 0\ m^{-1}$. Since the wavelength is $\lambda = 1/\xi$, the waves that make up the disturbances shown in these slices are plane waves that are traveling solely in the these directions.

The top plot shows the two-dimensional spectrum for horizontally moving optical disturbances that was been shown previously. There are three major flow-related structures that can be observed. The flow-related structure that lays along u is caused by the boundary layers on both walls of the wind tunnel. It can be seen that the boundary-layer signal has a peak at the free-stream velocity, u, and has a slight decay as the velocity decreases towards the dotted line of $0.7u$ with a sharp decay as

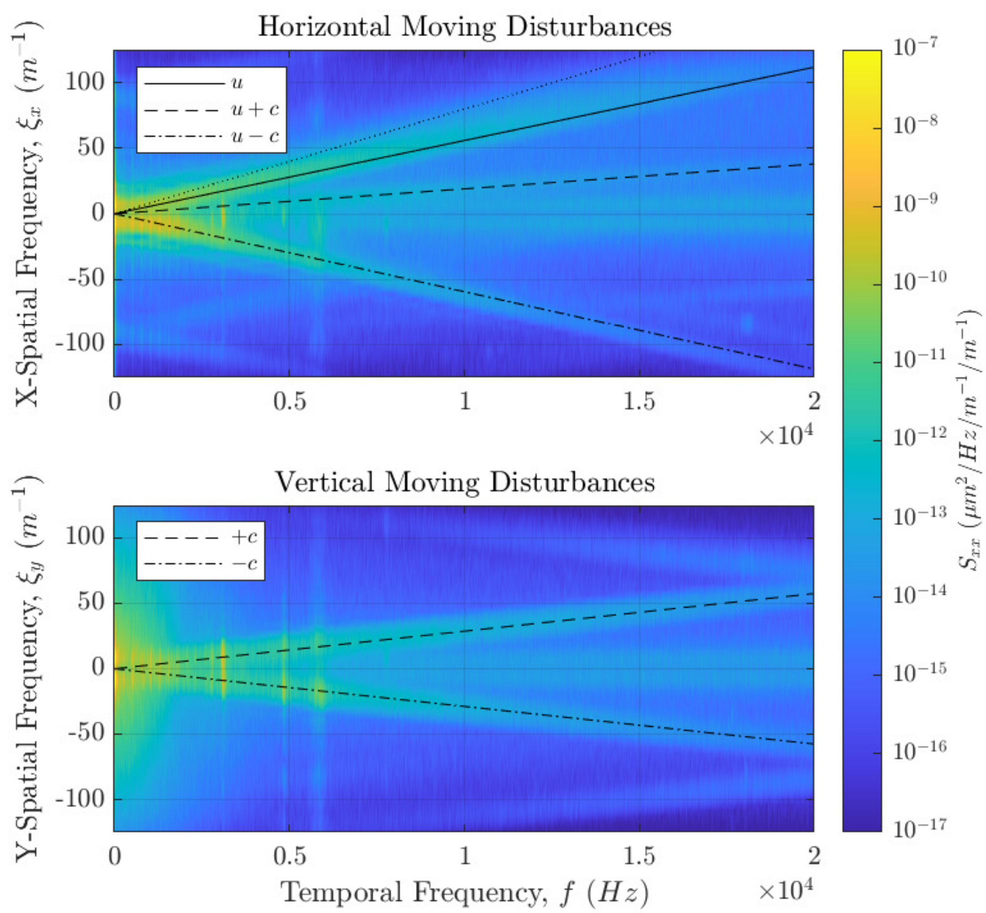

Figure 4.4. Horizontal and vertical moving optical disturbances. This is the same data as presented in Figure 4.1 but after calculating the full three-dimensional spectral estimate. These optical disturbances are plane waves that are traveling solely in their respective directions.

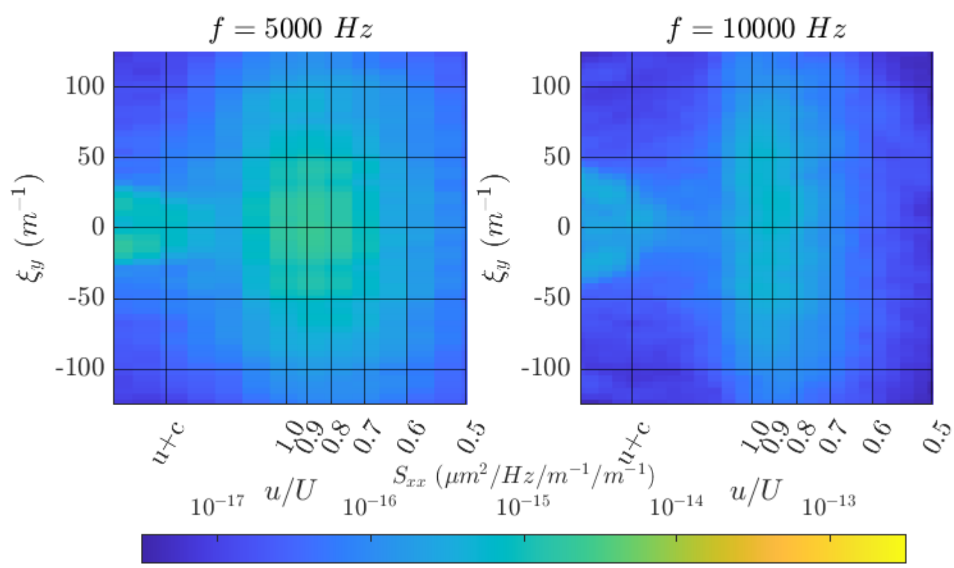

Figure 4.5. Temporal-frequency slices at 5 and 10-kHz with the various horizontal velocities labeled.

the velocity increases. While the boundary layer velocity has typically be reported as approximately $0.83u$ [17], this data shows the boundary layer velocity has a range of velocities at each given frequency in which the peak velocity component has some dependence on the temporal frequency. This can be more clearly seen in two temporal-frequency slice in Figure 4.5. Here the horizontal spatial-frequency has been replaced with the normalized horizontal velocity. The significant decay of the signal as the speed increases above the free-stream velocity there is a gradual decay as the speed decreases. There is also additional signal decay as the absolute value of the vertical spatial-frequency increases. The velocity of this boundary layer optical disturbance will be measured in Chapter 6 using a velocity filter to show a mean velocity of $0.85u$, which is near the generally accepted value of $0.83u$ [17].

The other two major flow-related structures in Figure 4.4 are related to acoustic signals traveling in both directions through the wind-tunnel, denoted by the dashed and dot-dash lines in the figure. The downstream-traveling acoustic wave, $u + c$, has a low signal power than the upstream-traveling acoustic wave, $u - c$. The likely explanation for this difference in signal power is that most of the acoustic energy in the wind tunnel is generated by the fan which propagates upstream and downstream within the wind-tunnel ducting. However, sound waves that move in the flow direction have their wavelength stretched as the flow is accelerated into the test-section contraction, while sound waves moving against the flow have their wavelength contracted. Hence the downstream-traveling waves have a longer wavelength as they pass through the measurement beam and thus more of the optical signal from the downstream-travelling waves is filtered out due to aperture filtering [40]. At low temporal-frequencies, the blade-passing frequency (520-Hz) and its associated harmonics appear as vertical lines with regular spacing in Figure 4.4.

The two main features on the vertical spectral slice plot on the bottom of Figure 4.4 are the signals moving at the speed of sound ($\pm c$) including some significant aliasing of these signals. These two lines represent acoustic waves that are traveling either straight up or down through the measurement beam. The blade-passing frequency and its harmonics are also visible in the vertical moving wave plots in both directions and have much less broadband spatial content in the vertical direction. Some of the high temporal-frequency narrow-band signals (3, 5, and 6-kHz) contain most of the signal power at the speed of sound lines in the vertical spectral slice plot. These signals has some dependence on the free-stream Mach number (see Figure 4.7). These maybe vibrations originating from the tunnel fan that are currently limiting the top speed of the tunnel; some older optical wavefronts collected in this tunnel under similar measurement conditions do not show these narrow-band signals. Because the portion of these signals with the most power is traveling vertically through the test section instead of steam wise, the tunnel walls maybe excited by the fan and resonating.

The stationary modes that have been discussed previously that lay along the temporal-frequency axis in the horizontal spectral slice plot also appear in the same location in the vertical spectral slice plot. These stationary modes appear the be constant when viewed from either direction and through out time. As a white-noise is generally not physical unless it is bandwidth limited with a falloff of at least $1/f^2$ [3]. Some of these stationary modes are likely cause by vibrations of various optical elements, especially at low temporal-frequencies. At higher temporal-frequencies, the stationary modes maybe related to electronic noise from the high-speed camera, higher order optical noise from the laser, or even numerical error from the processing code.

4.4.2 3-D Representations of Multidimensional Spectral Estimation

While the two-dimensional slices are fairly informative, particularly when it comes to signal strength of various flow structures and their velocities, a three-dimensional plot allows better visualization of the overall flow structures although some details are lost because typically only one power level can be plotted at a time. The same data that has been previously shown in two-dimensional form, is depicted in Figure 4.6 as an isosurface with a power of 10^{-14} $\mu m^2/Hz/m^{-1}/m^{-1}$ and shown from four different views. This particular isosurface encompasses approximately 99.9% of the power of the optical disturbances. The largest feature is the boundary layer which resembles an ellipsoidal plane that is tilted in the $f - \xi_s$ plane. The other main feature is the acoustic signal which appears as a cone which is slightly tilted in the direction of upstream-moving disturbances. The acoustic signal separates into several spikes at high temporal frequencies some of which are constructive interference from aliased signal ($\xi_x \approx 25\ m^{-1},\ \xi_y \approx \pm 60\ m^{-1}, andf \approx 20kHz$) which is better visualized in the 20-kHz temporal-frequency spectral slice in Figure 4.5. There may also be a small number of dominant duct modes at these high temporal-frequencies. The last feature is the stationary modes which appears as the cylindrical structure along the center of the plot (near zero spatial-frequency in x and y), which have a near constant shape and magnitude through all temporal-frequency ranges.

Figure 4.7 shows two views of an isosurface of the multidimensional spectrum over a range of Mach numbers. All of these plots are of an isosurface with the same power as used in Figure 4.6. The stationary modes seems to be constant throughout the range of Mach numbers indicating that they are most likely not flow related. The boundary layer signal increases in power significantly as the Mach number is increased while also the slope and thus the velocity is significantly increased as well. As shown in [17], the aero-optical $\mathrm{OPD_{RMS}}$ of the flat-plate boundary layer on the walls of the wind tunnel is expected to vary according to

$$\mathrm{OPD_{RMS}} = BK_{GD}\rho_\infty M^2 \delta \sqrt{C_f} G(M). \tag{4.20}$$

Hence the significant increase in the power of the boundary-layer spectrum with Mach number that can be observed in Figure 4.7 is expected based on the M^2 dependence in Equation 4.20. The increase in slope of the boundary-layer signal is also expected, and is caused by the increase in the convection speed of the boundary-layer aero-optical disturbances as the free-stream Mach number increases. The acoustic signal sees some interesting evolution as well. Along with the strength greatly increasing with Mach number, the slope of the upstream traveling disturbances decreases significantly while the downstream moving acoustic disturbances do not see much change other than an increase in signal strength.

As the angle of the optical beam changes as it looks through the test section the horizontal spatial-frequency goes from measuring only the axial component of the optical disturbance to measuring a combination of the axial and span wise component. This can be seen in Figure 4.8 with the same isosurface value as shown in previous figures and at a Mach number of 0.5. The 90° case

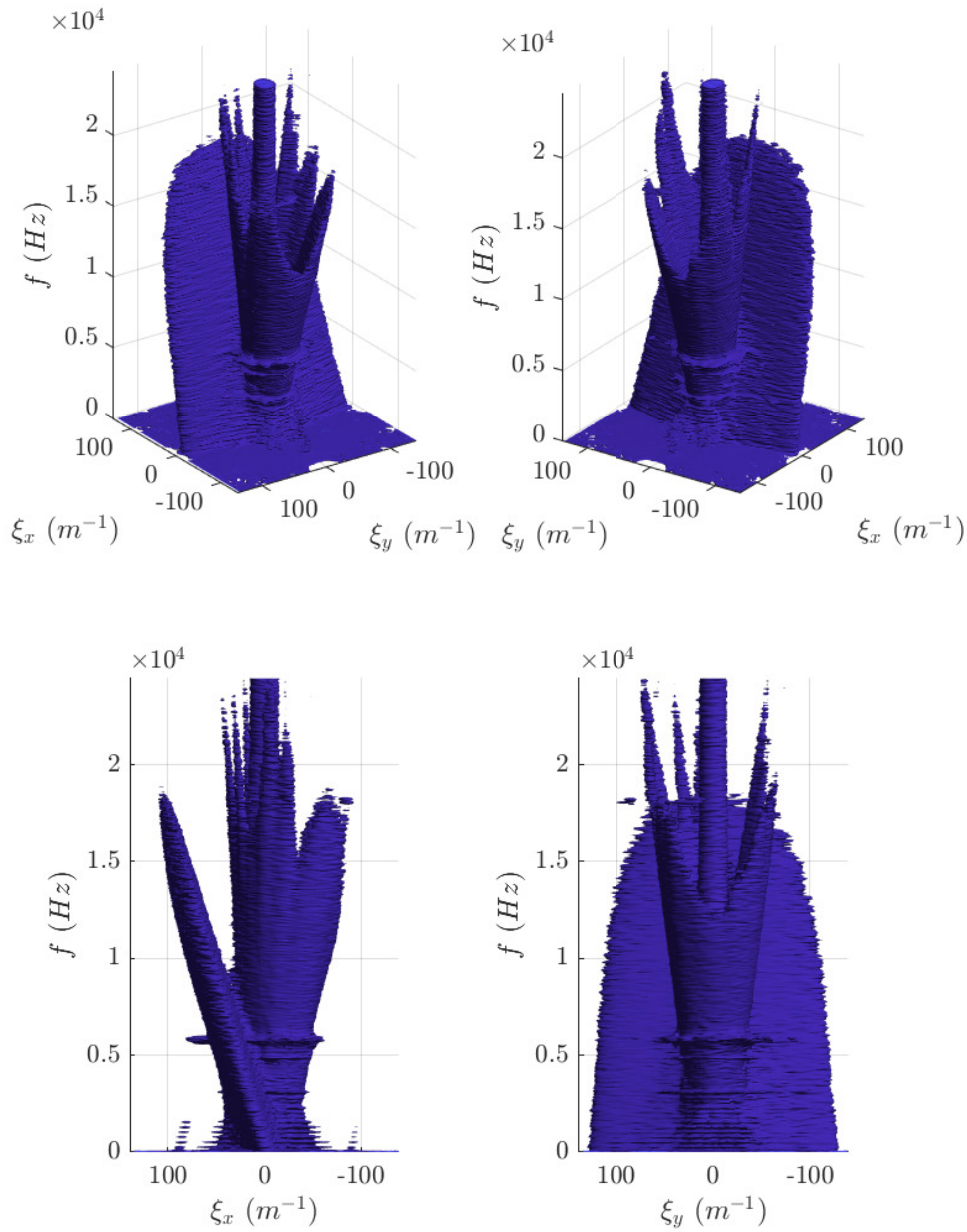

Figure 4.6. Three-dimensional view of the multidimensional spectral plot showing an isosurface at a power of 10^{-14} $\mu m^2/Hz/m^{-1}/m^{-1}$. The isosurface encompasses 99.9% of the power of the wavefront.

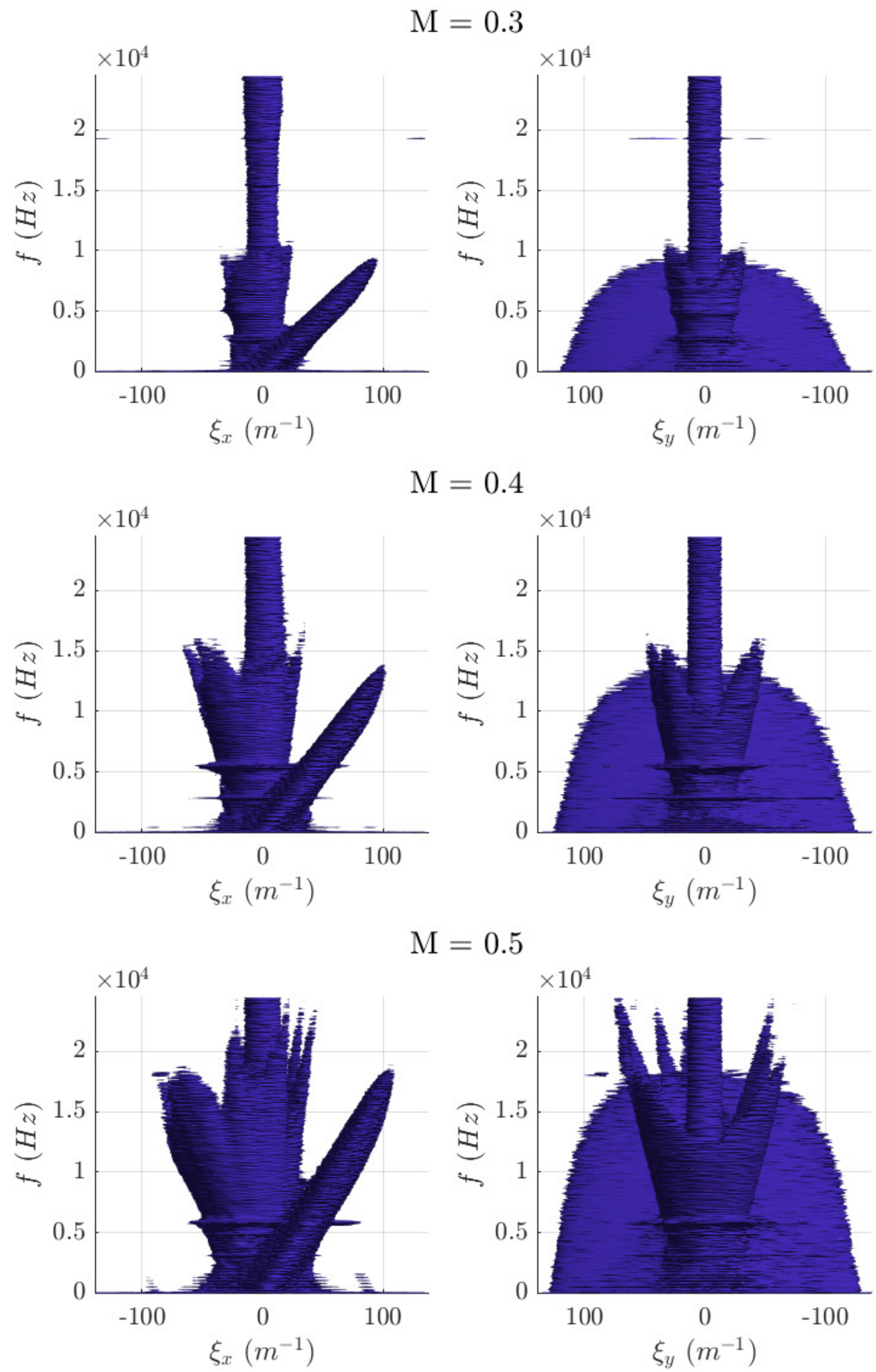

Figure 4.7. Multidimensional spectral estimate isosurfaces as the Mach number increased from 0.3 to 0.5. The isosurfaces are all shown at a power of 10^{-14} $\mu m^2/Hz/m^{-1}/m^{-1}$ and all encompass 99.9% of the wavefront power.

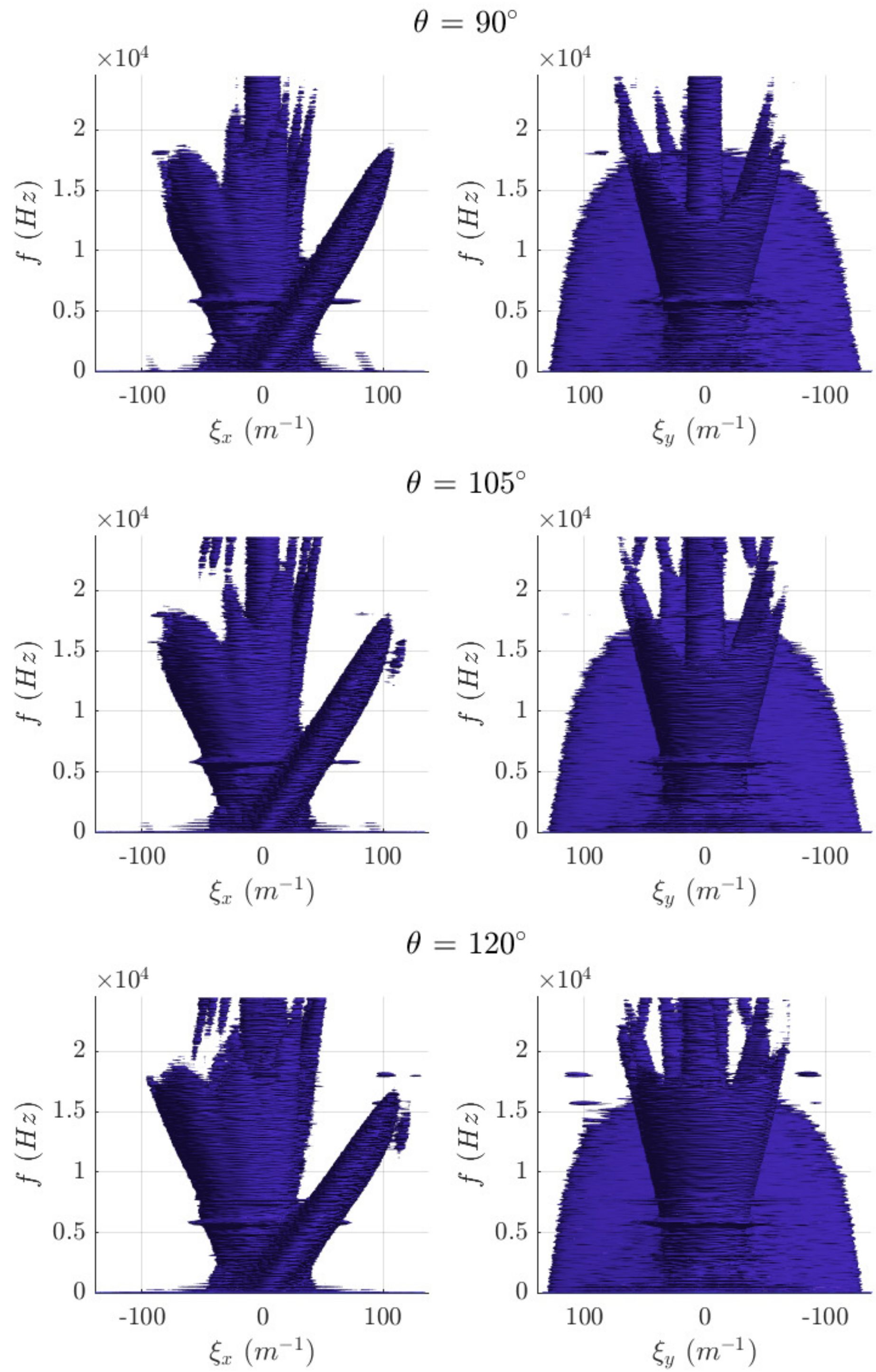

Figure 4.8. Multidimensional spectral estimate isosurfaces of different viewing angles through the test section at a Mach number of 0.5. The isosurfaces are all shown at a power of 10^{-14} $\mu m^2/Hz/m^{-1}/m^{-1}$ and all encompass 99.9% of the wavefront power.

has been shown previously and the vertical component of the optical disturbance sees little change as the viewing angle is increase except a small reduction in the boundary layer signal and some additional signal at the high temporal-frequencies in the acoustic cone. As the angle is increased the side of the acoustic cone traveling in the direction of flow is significantly in power, with a large amount of the signal being aliased into the upstream-traveling side as 'stalactites' as odd angles. The upstream-traveling acoustic signal is also increased in power but to a lesser extent. The stationary mode pillar experiences some change as well as the viewing angle hits 120° and is stretched in the horizontal direction. The effective velocity of the optical disturbances is reduced for the disturbances traveling in the same direction as the flow and increased for the disturbances traveling in the opposite direction.

While these three-dimensional isosurfaces offer some significant insight into the overall structure of the various optical disturbances they do not show how the spectral inside of the isosurface is distributed. Views inside of the isosurface of the horizontal and vertical plane waves were shown in Figure 4.4 while Figure 4.9 shows slices at various temporal-frequencies. The temporal-frequencies spectral slices shown are at: 0-Hz, the blade-passing frequency at 517-Hz, the second harmonic of the blade-passing frequency at 1551-Hz, and additional slices at 5, 10, and 20-kHz. The slice at 0 Hz temporal frequency shows the spatial frequencies of the wavefront disturbance that does not change with time. This temporally constant wavefront disturbance is typically called the "mean lensing"component of the wavefront measurement, since it is has an effect similar to a lens placed in the beam. The mean lensing slice at 0-Hz shows a mostly axisymmetric pattern with most of its power concentrated at low spatial frequencies. There appear to be the occasional spike radiating out from the center, most noticeably in line with the boundary layer signal.

The next four slices, for f=517.1-Hz to 10-kHz, show a vertical line associated with the boundary layers aero-optical disturbance, which progressively moves towards positive x-spatial frequencies with increasing frequency. The boundary-layer disturbance appears to be rotated slightly counter-clockwise indicating that the interrogation beam is slightly rotated between the test section and the wavefront sensor. The boundary layer signals at the lower temporal-frequencies appear to have equal decay in both the positive and negative ξ_x directions while at the higher frequencies, the decay is much more gradual in the positive ξ_x direction. This could be indicative of the lower temporal-frequency disturbances in the boundary layer typically traveling at a more uniform speed very near the free-stream velocity likely being either in the outer boundary layer or free-stream tunnel turbulence. The higher temporal-frequency disturbances seem to have a much wider range

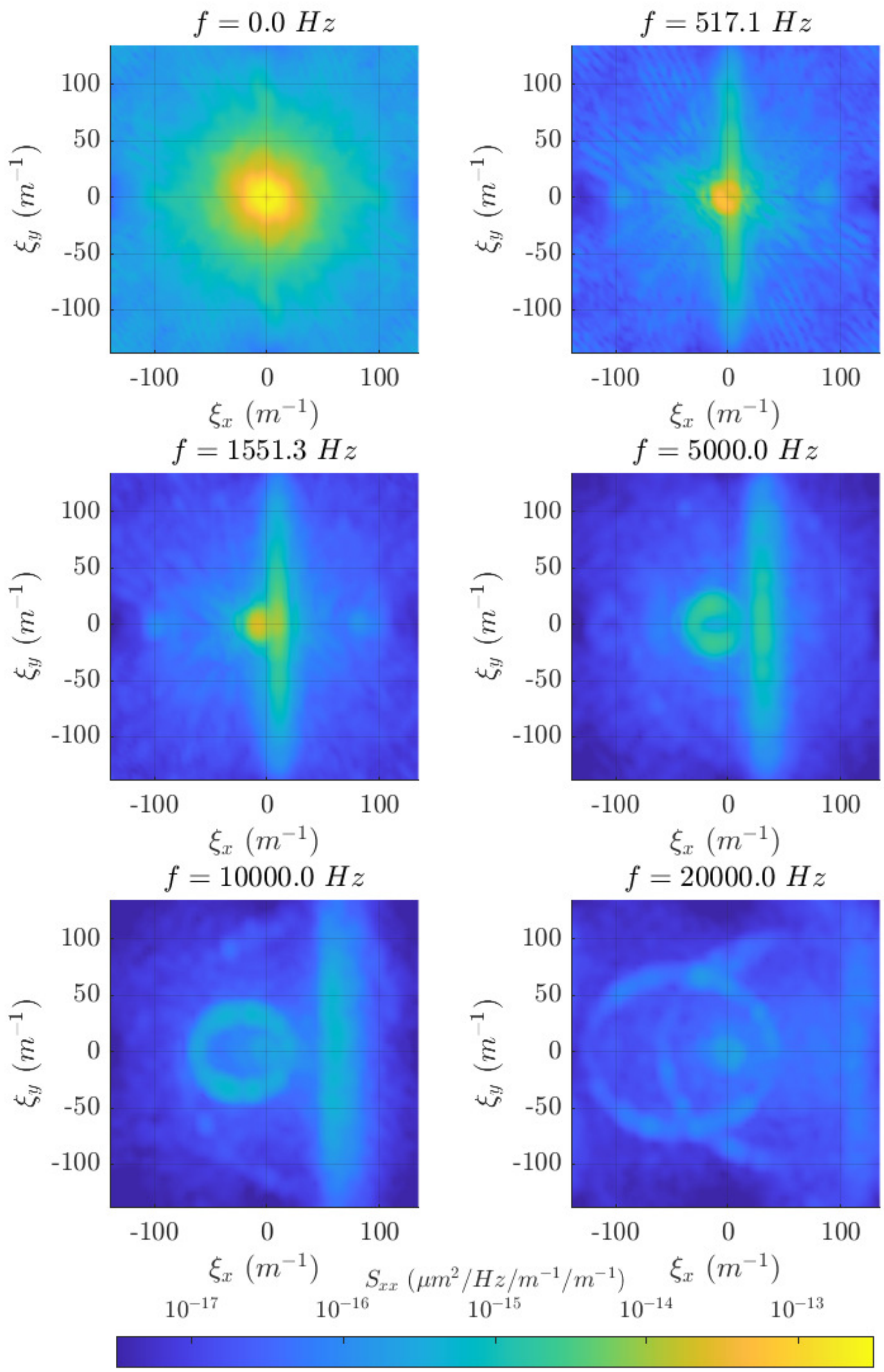

Figure 4.9. Multidimensional spectral estimate slices at various temporal-frequencies.

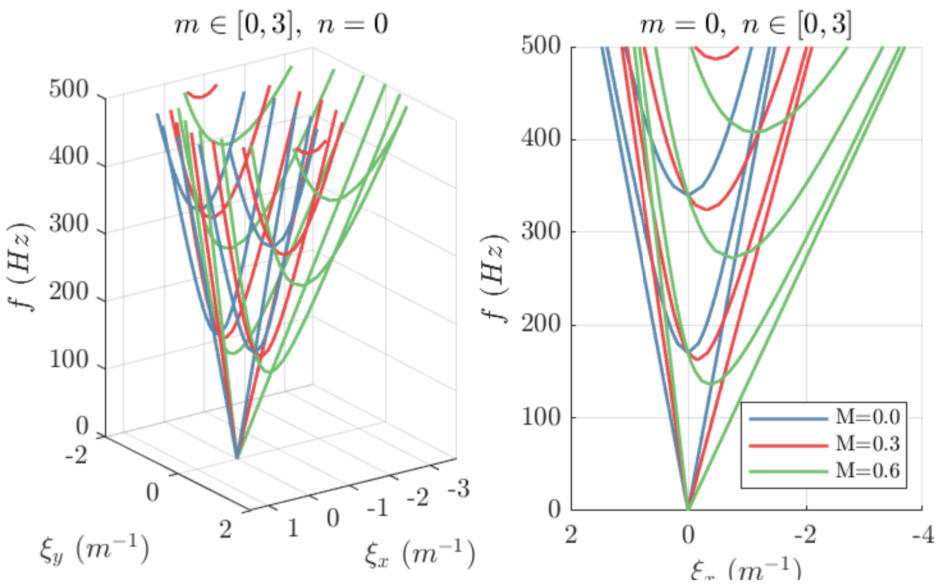

Figure 4.10. Acoustic duct mode lines showing the spatial-frequency location as a function of temporal-frequency, Mach number, and mode number.

of velocities that approach the free-stream velocity and are likely small structures that reside in different parts of the boundary layer and hence travel with a wide range of convection velocities.

The acoustic disturbances show an interesting evolution as the temporal-frequency increases. At low temporal-frequencies, the acoustic disturbances are concentrated near zero spatial frequency and with strong power. At high temporal-frequencies the acoustic disturbances appear as elliptically shaped rings. At 20-kHz, there are two elliptical shapes that are easily identifiable, the smaller one is the signal that is actually present at that frequency while the other one is aliased data due to the limited temporal sample rate. There is constructive interference where the two acoustic ring intersect. The 10-kHz slice also shows a small amount of acoustic aliasing Both the 10 and 20-kHz acoustic rings show some a non-uniform signal power throughout the circumference which are also visible in the three-dimensional views as the spikes at the high temporal-frequencies.

4.4.3 Artificially Increased Sample Rate

In the spectral slices shown in Figure 4.4, when a signal crosses a plane represented by one of the Nyquist frequencies (positive or negative) it is transposed to the conjugate Nyquist frequency plane and continues on with the same gradient as before. This behavior is illustrated in Figure 4.11 using the horizontal and vertical multidimensional spectrum slices. Here the black box represents the

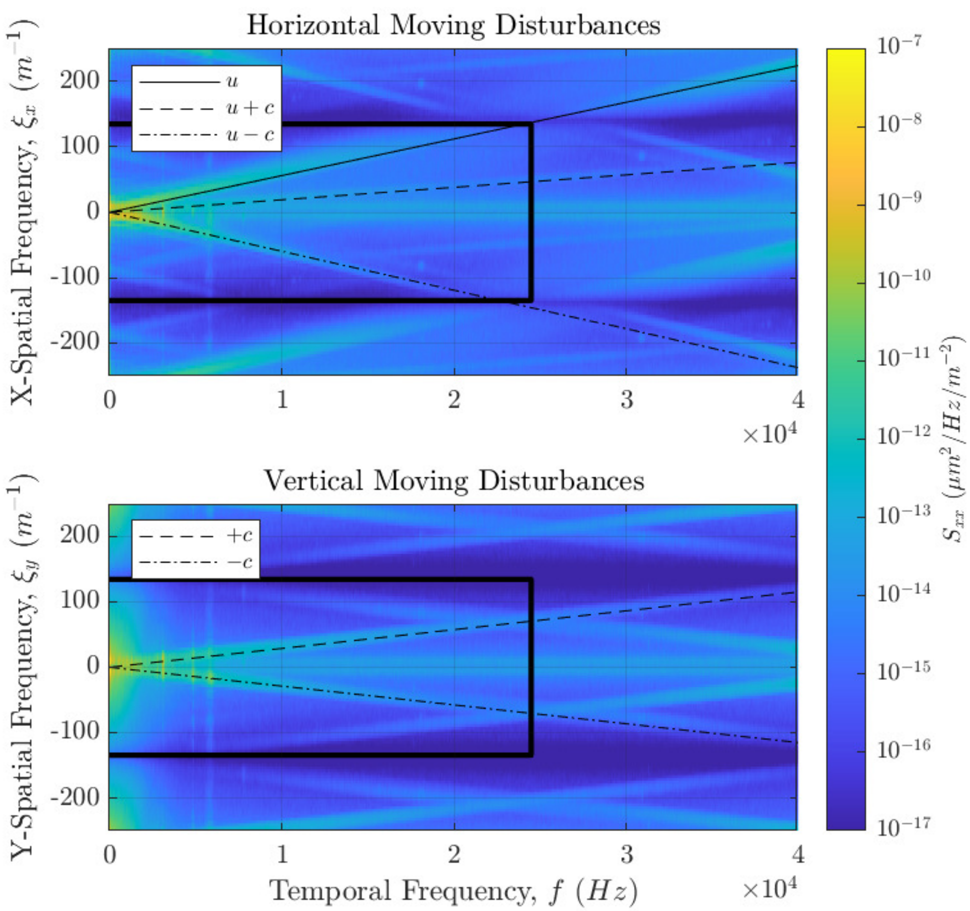

Figure 4.11. Artificially increased temporal sample rate using a dispersion analysis. The black box represents original dispersion plot.

original extents of the spectrum, while outside of the box the spectrum has simply been duplicated and appended which effectively artificially increases the sample rate. In this case the spectrum array was tiled in a three-by-three grid for each of the horizontal and vertical slices. This process has been previously discussed for two-dimensional spectral plots [26]. Along the spatial Nyquist frequency edges, there is a significant dip in the signal strength which would result in a spatial super sampling to have a significant loss of signal at these frequencies.

On the upstream moving disturbance side there is some noticeable aliasing that is present including a significant spike at 18-kHz (-80-m^{-1}) while aliased and about 31-kHz (-200-m^{-1}) when it has been unaliased. As that upstream moving acoustic disturbance crosses the spatial Nyquist frequency, the signal strength drops significantly to local background levels. The boundary layer signal is unfortunately to well aligned with its tiled self for any aliased data to be noticeable. The vertically moving disturbances have some significant temporal aliasing but little to no spatial aliasing.

This process can both of increase the sample rate and de-alias a multidimensional spectrum but it will also create additional aliased data. Depending on the downstream analysis to be performed, this additional aliased signal may need to be filtered out. In cases where the signal and an aliased data source do not intersect this process would work when investigating the spectrum along a path with little issue [26]. Signal interpolation may be needed to extract the signal from an intersection with aliased data.

There maybe some circumstances when the sample rate cannot be increased nor aliased data removed, such is likely the case for the boundary layer signal shown in the horizontal moving disturbances plot because the signal is directly inline with its aliased self. This may also cause an issue when trying to analyze the original spectrum, particularly at the higher frequencies where the aliased data is sufficiently strong and overlapping the true signal. To avoid this the sample rate velocity,

$$V_s = f/\xi, \tag{4.21}$$

should sufficiently different enough from the disturbance's characteristic velocity. This difference will vary for the depending on the spectral width of the signal. The sample rate velocity of the spectrum in Figure 4.11 is 176.4-m/s, the free-stream velocity is 174.3-m/s and the boundary layer has a significant spectral with to the signal such that it would be difficult to separate the real and aliased signals. The upstream-traveling acoustic wave however is a fairly thin signal that is distinguishable from the aliased signal and it has a characteristic velocity of -173.0-m/s.

CHAPTER 5

SYNTHETIC WAVEFRONT

In order to best understand how some basic filters preform on a set of data, a fully known synthetic wavefront was generated such that all of the various components could be generated separately with the combined product filtered and compared to the synthetic wavefront containing only relevant aero-optical data. This is done by creating an input dispersion plot where each source component is separately generated with parameters that can be modified to alter the output signal as necessary. Signals that are assumed to be statistically independent are converted into dimensional space separately and then summed together. While signals that are assumed to be related to one another (such as the sound and vibration components) are summed together in frequency space. Figure 5.1 shows the input dispersion plot with each signal component separately colored. The aero-optical signal is shown in red, the stationary modes in blue, duct acoustics in magenta, blade-passing frequency related corruption in green, slowly varying mean-lensing in yellow, and background in cyan.

Wavefronts were generated to approximate the sample conditions in that the data presented in Figure 4.6 were measured with. The sample rate was 200 m^{-1} with 64 (2^6) samples in the spatial dimensions and 30,000 Hz with 8192 (2^{13}) samples in the temporal dimension. The speed of sound was chosen to be 340 m/s, with a Mach number of 0.6, and a boundary layer velocity of 163.2 m/s ($0.8U_\infty$).

The general process of developing most of the component signals was to determine an approximate shape, normalize it in the appropriate dimensions, and scale the result by using a function derived from a hyperbola,

$$\frac{\log_{10}(WF) - b}{b^2} - \frac{\xi_{\rho_N}^2}{a^2} = 1, \tag{5.1}$$

such that the signal strength at unity of the normalized radial frequency, $\log_{10}(WF(\xi_{\rho_N} = 1))$, and the limiting slope, a/b, are inputs. This results in the signal strength of the wavefront being

$$\log_{10}(WF) = b - \sqrt{\frac{\xi_{\rho_N}^2}{m^2} + b^2}, \tag{5.2}$$

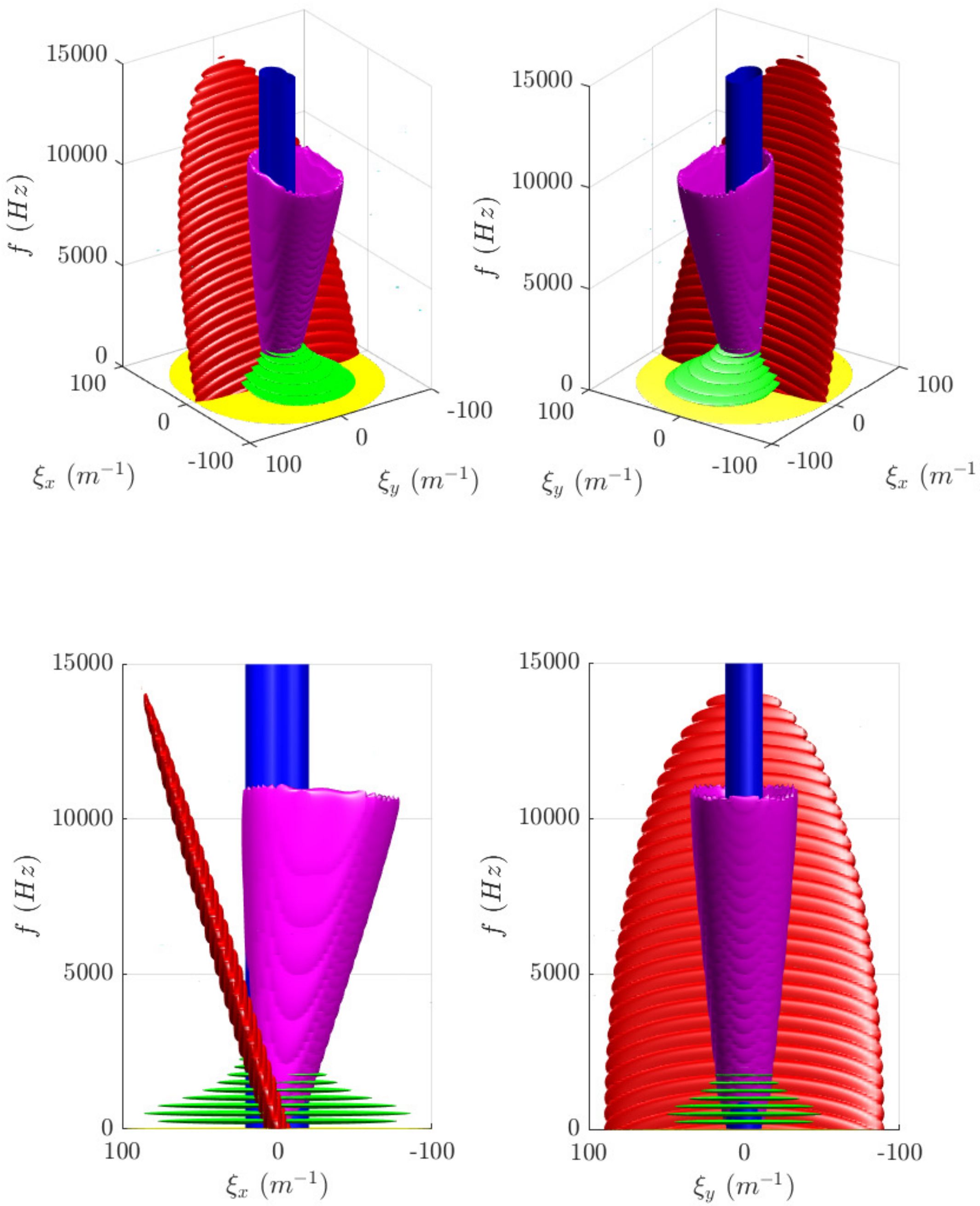

Figure 5.1. Synthetic wavefront input dispersion plot of an aero-optical signal and various signal corruption components. The aero-optical signal is shown in red, the stationary modes in blue, duct acoustics in magenta, blade-passing frequency related corruption in green, slowly varying mean-lensing in yellow, and background in cyan.

where

$$b = \frac{1}{2\log_{10}(WF(\xi_{\rho_N} = 1))} \cdot \left(\log_{10}(WF(\xi_{\rho_N} = 1))^2 - \frac{1}{m^2}\right). \tag{5.3}$$

The code used to generate the synthetic wavefront used in this section is shown in Listing A.3.

5.1 Aero-Optical Signal

The aero-optical signal which is approximating an optical beam passing through a boundary layers normal to each of the test section walls. This signal was approximated by creating an ellipsoid in the plane of the feature's velocity and normalizing the radius by some arbitrary factors to roughly match the shape of the measured dispersion plot shown in Figure 4.6. The dispersion magnitude was then calculated by applying Equation 5.2, with relevant code shown on Lines 19-30 of Listing A.3. In Figure 5.1 the aero-optical signal is shown in red.

5.2 Stationary Mode Signals

The stationary modes in Figure 4.6 appear to be temporally white-noise with the spatial frequencies forming an epicycloid of $k = 2$. This shape was further simplified using a single trigonometric function to represent the normalization function of the radial spatial frequency,

$$\xi_{\rho_N} = \frac{\xi_\rho}{\xi_{\rho_0}\sqrt{10 - 6\cos(2\xi_\theta)}}, \tag{5.4}$$

this makes an epicycloidal like shape which has a smooth derivative. This dispersion component is shown in blue in Figure 5.1 and the relevant code shown in Lines 61-66 of Listing A.3.

5.3 Sound & Vibration Signals

The sound & vibrating component signals are comprised of two parts. The first of these is the blade-passing frequency and its harmonic disturbances (shown in green in Figure 5.1) and the second is the acoustic duct modes (shown in magenta). Like the stationary modes, the blade-passing frequency disturbances were modeled with the simplified epicycloid narrow-band disc and each harmonic was modulated by using a low-pass filter offset to the blade-passing frequency. The code for the blade-passing frequency disturbances is shown in Lines 97-113 of Listing A.3.

The acoustic duct mode disturbances form a cone which in the $f - \xi_x$ plane is defined by the lines $u \pm c$, while in the $f - \xi_y$ plane is defined by the speed of sound. At each temporal frequency step an ellipse was defined based on the constraining lines and the distance to that ellipse used to calculate a normalized radial frequency. The strength of the disturbance was decreased logarithmically in temporal frequency as shown in the code in Lines 183-200 of Listing A.3.

5.4 Mean Lensing Signal

The mean-lensing signal (shown in yellow in Figure 5.1) uses a stretched version of the simplified epicycloid and represents the slowly varying spatial disturbance. The relevant code is shown on Lines 144-152 of Listing A.3.

5.5 Background Noise Signal

The background noise disturbance (with a few small spots shown in cyan in Figure 5.1) was the only component that did not use the hyperbola to scale the signal but instead was just normally distributed random noise with a mean noise level and deviation as inputs. The relevant code is shown in Lines 230-234 of Listing A.3.

5.6 Synthetic Wavefront Creation

A synthetic signal can be created from a power spectra by solving for x in Equation **??** and using the Inverse Fast Fourier Transform,

$$x(t) = \mathrm{REAL}\left[\mathrm{IFFT}\left\{\sqrt{S_{xx} \cdot N \cdot f_{samp}} \cdot \exp i\phi\right\}\right], \tag{5.5}$$

where REAL is the real component and ϕ is a random set of phases for each point in the measurement space. As shown previously this relation can be extended into n-dimensions,

$$f(\mathbf{x}) = \mathrm{REAL}\left[\mathrm{IFFT_n}\left\{\sqrt{\mathbf{S_{xx}} \cdot \prod \overrightarrow{N} \cdot \overrightarrow{f}_{samp}} \cdot \exp i\phi\right\}\right]. \tag{5.6}$$

Care should be taken when constructing the random set of phases, as the zero-frequency component has zero phase and the phases on either side of it are conjugates of one another. The code for creating a wavefront from a dispersion plot is shown in Lines 336-340 of Listing A.3 and is specifically creating the wavefront for the aero-optical signal but other signals are generated using the same basic code. Note that the first three lines are to get the set of phases properly configured that creates conjugate phases rotated about the origin.

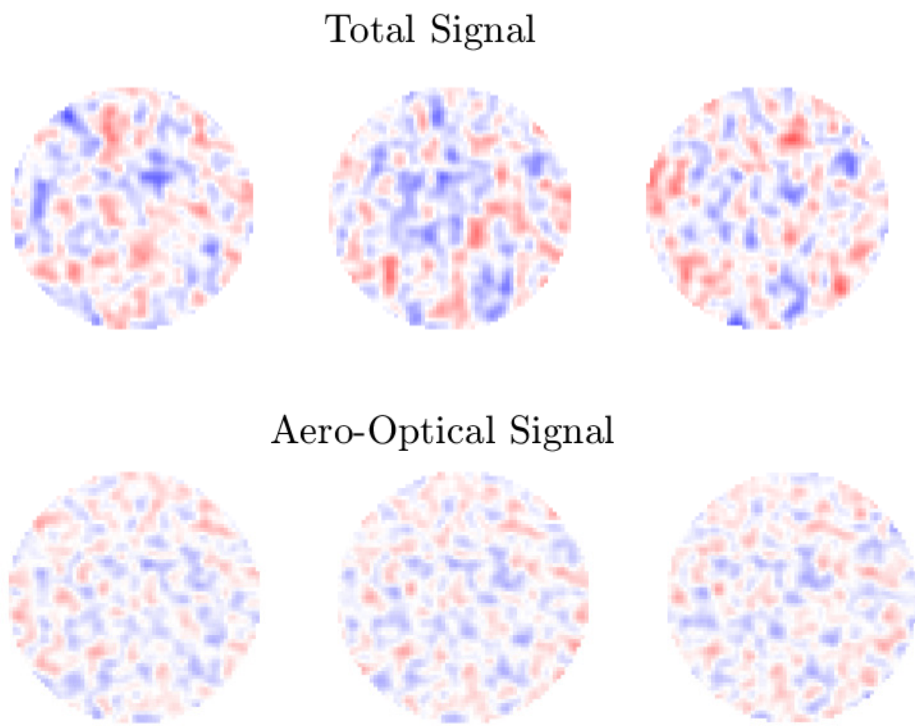

Figure 5.2. Sample frames from the synthetic wavefront with the total wavefront signal on top and the aero-optical only signal bottom. Flow is from right to left.

It was assumed that the aero-optical signal, the stationary modes, and the background noise were statistically independent of one another and the sound and vibration combination of modes and as such could be separately transformed into physical space. While the components of the sound and vibration sources, the blade-passing frequency, the acoustic cone, and the mean-lensing, were assumed to be related to one another and thus were summed together in frequency space prior to being transformed into physical space. Once the separate components were in physical space the total wavefront was obtained by summing up the separate components with the aero-optical signal being a separately saved along side the total wavefront. Some frames from the synthetic wavefront are shown in Figure 5.2 with the total wavefront shown on top and the aero-optical only signal shown on the bottom. Flow is from right to left. The aero-optical signal is often times noticeable in the total wavefront signal, but can be easily overpowered by the various contamination sources.

5.7 Comparison to Measured Data

A dispersion plot of the total synthetic wavefront is shown in Figure 5.3. In this view the aero-optical signal is more noticeable but there still remains some significant overlap with the various contamination sources. While the mean-lensing component is not as visible in this isosurface, the rest of the dispersion plot in a good representation of the input dispersion plot shown in Figure 5.1. The blade-passing frequency was depicted as symmetric in the synthetic wavefront while measured data (shown in Figure 4.6) shows more signal on the side traveling in the direction of flow. The harmonics of the BPF are more on the upstream traveling side of the dispersion and are a little less pronounced in the measured data. The total synthetic wavefront has a spatial time-averaged RMS of $0.0112 \pm 0.0006 \mu m$ with the aero-optical only signal having a spatial time-averaged RMS of $0.0073 \pm 0.0003 \mu m$. The measured wavefront presented in Figure 4.6 had a spatial time-averaged RMS of $0.0874 \pm 0.0263 \mu m$. The overall spatial RMS of the synthetic wavefront was 12.8% when compared to the measured wavefront indicating that the algorithms used to generate the wavefront are not representative of reality and can provide a future path of research in order to produce more realistic synthetic wavefronts. Double Check line numbers for the Listings.

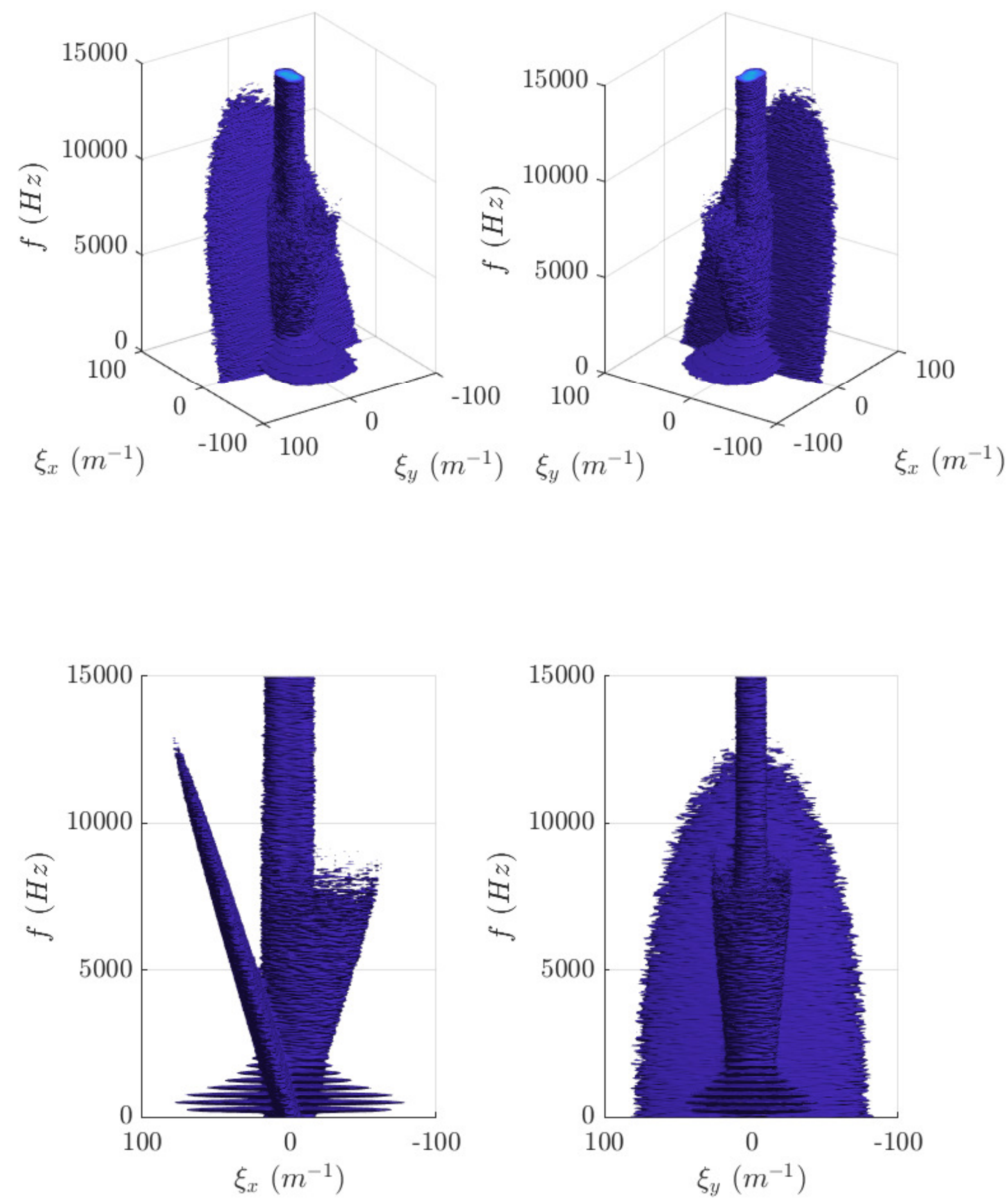

Figure 5.3. Synthetic wavefront output dispersion plot of an aero-optical signal and various signal corruption components.

CHAPTER 6

SINGLE SENSOR FILTERING TECHNIQUES

Show some dispersions of POD modes and discuss whether or not POD filtering maybe a viable option.

A filter is a function, $G(\omega)$, that describes the gain a signal will experience in frequency space. In the simplest case, the filtered signal is the inverse Fourier transform of the gain multiplied by the Fourier transform of the signal. Additionally, a windowing function, $W(\mathbf{x})$, can be used to help suppress finite sampling effects,

$$f_F(\mathbf{x}) = \mathrm{REAL}\left(\frac{\mathrm{IFFT_n}[G(\omega)\cdot \mathrm{FFT_n}\{f(\mathbf{x})\cdot W(\mathbf{x})\}]}{W(\mathbf{x})}\right), \tag{6.1}$$

where f is the signal function and f_F is the filtered signal. Depending on the windowing function some data could be destroyed during this process if there is a zero present due to the possibility of dividing by zero.

A basic MATLAB code for applying a filter to a wavefront using a separate function for both generating and applying the gain function which is presented in Listing A.4. This code generates a windowing function as described by Equations 4.7, 4.14, and 4.17. The temporal windowing function was generated with an additional two terms such that the end points which are equal to zero could be removed to prevent the first and last frames from being destroyed. Likewise, the spatial window used the arbitrary aperture function which ensures that all of the points inside of the aperture are non-zero. In some cases, a windowing function was not used due to filtered wavefront having a far greater magnitude in some places despite the precautions used. The filter presented in this code sample is a second order temporal high-pass filter with a cut-off frequency of 2000 Hz. The function WFfilter takes input based on a normalized cut-point in reference to the sample rate.

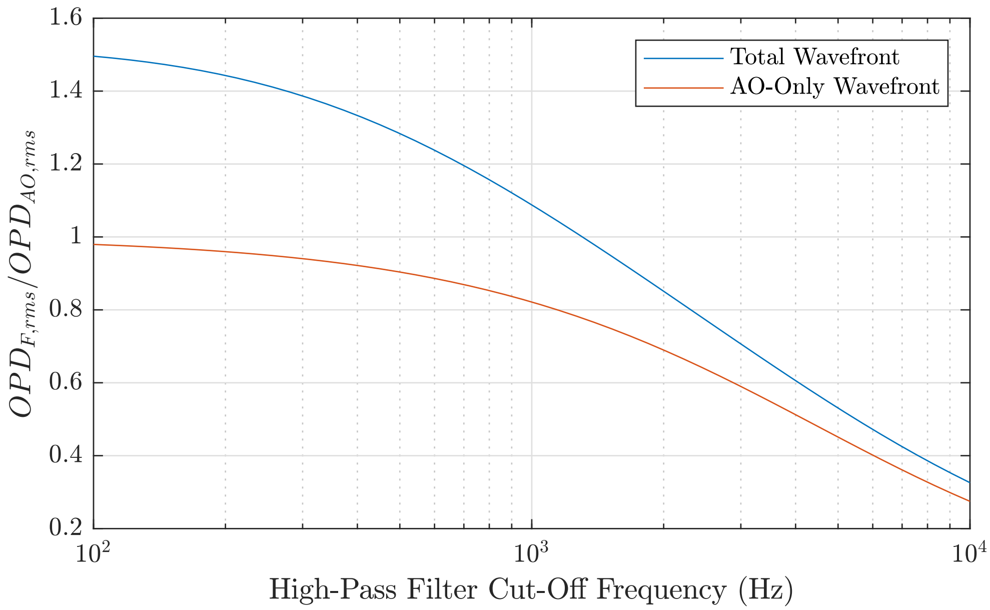

Figure 6.1. OPD time-averaged spatial-RMS of high-pass temporal filters relative to the aero-optical only unfiltered wavefront.

6.1 Temporal Filter Methods

The methods presented in this section are based on Butterworth filters [8] but could easily be extended to other types of filters. The basic gain function,

$$G(f) = \frac{1}{\sqrt{1 + \left(\frac{f}{f_c}\right)^{\pm 2n}}}, \tag{6.2}$$

where f_c is the cut-off frequency, n is the filter order (number of filters in a series), and $\pm$ represents either a low-pass ($+$) or high-pass ($-$) filter. In this particular formulation, only the magnitude is attenuated, circuit based Butterworth filters or their digital copies will have some variable phase attenuation as well. Additionally, a band-pass filter can be constructed by placing a low-pass in series with a high-pass filter and a band-stop by placing the two types in parallel.

As a large portion of the wavefront contamination is at low frequencies, a high-pass filter is the most useful in temporal space for removing unwanted contamination, as shown in Figure 6.1. This figure shows the time-averaged spatial-RMS of both the total and aero-optical only wavefronts with various cut-off high-pass filters relative to that of the aero-optical only wavefront unfiltered. The total wavefront ratio crosses unity around 1200 Hz, which is about halfway between the second and third harmonic of the blade-passing frequency in this simulated wavefront. While approximately 75% of the aero-optical signal remains at this cut-off frequency, that difference is made up by the remaining contamination. This can provide a computationally cheap way estimating the aero-optical portion of the wavefront for calculations that rely on the spatial-RMS of a wavefront. While it is easy to determine a cut-off frequency for this synthetic wavefront, a measured wavefront will likely take some knowledge or expectation of the contamination that is present in the measurement.

An example of band-pass and band-stop filtering is shown if Figure 6.2. The figure shows measured data that is band-stop filtered in the left column and band-pass filtered in the right column in several different frames. The flow is from right-to-left and the band-pass filtered wavefront clearly shows upstream-moving optical disturbances associated with acoustic duct modes traveling upstream from the fan. The band-stop shows a much slower moving optical disturbance that is in general moving in the direction of the flow, but it still possess the optical disturbances of the blade-pass frequency harmonics.

One thing of note, MATLAB's builtin filter functions only work in one-dimension of frequency space and are unable to determine the direction that a signal is traveling. They also only apply the filter to the positive frequencies and zero-out the negative ones which both reduces the signal by two and also switches all disturbances to moving in the same direction. So even for a filter that operates in one-dimension, it is best to apply the filter over both positive and negative frequencies to the n-dimensional Fourier transform in order to preserve the direction of travel of a signal. This additionally allows several filters to be applied in series with one another without having to perform a Fourier and inverse Fourier transform for each successive filter. I should maybe show this matlab filter issue in an appendix.

Some additional uses of temporal filters would be in sizing and/or designing an adaptive optics system. A low-pass filter with a cut-off at the bandwidth of either a fast-steering or deformable mirror would help determine the signal that a system would need to reject. A control system may need to have the bandwidth reduced in order to keep a mirror's travel within limits. While a high-pass filter would inform designers of the remaining optical aberrations that cannot be corrected.

6.2 Upstream/Downstream Moving

For the filtering of upstream and downstream moving optical disturbances a logistic function was chosen,

$$f(x) = \frac{1}{1 + \exp\{-kx\}}. \tag{6.3}$$

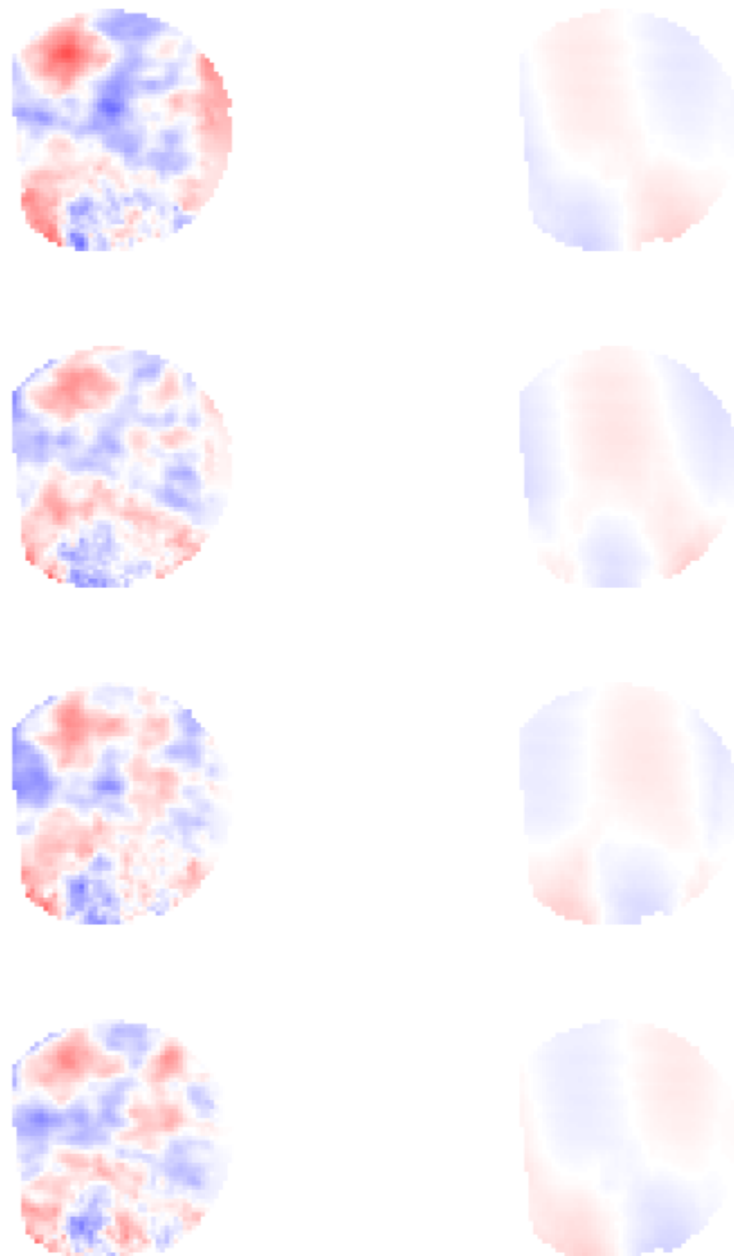

Figure 6.2. Measured wavefronts filtered at the blade-passing frequency (532±10 Hz). The left column is band-stop filtered while the right is band-pass filtered.

This function needs to be expanded into two-dimensions (x and t) with the filter ideally returning a value of one in both the first and third quadrants and zero otherwise for a filter outputs disturbances moving in the direction of flow. To accomplish this the logistic curve in each dimension is scaled and offset to output values between negative one and positive one,

$$G_t(f) = \frac{2}{1 + \exp\{-k_t f\}} - 1 \tag{6.4}$$

and

$$G_x(\xi_x) = \frac{2}{1 + \exp\{\pm k_x \xi_x\}} - 1, \tag{6.5}$$

where $\pm$ determines whether the filter is obtaining upstream traveling disturbances $(+)$ or downstream traveling $(-)$. These two gain functions are then multiplied together and scaled to output values between zero and one,

$$G(\xi_x, f) = \frac{(G_t \cdot G_x) + 1}{2}. \tag{6.6}$$

As the values of k_x and k_t go to infinity an ideal case is obtained. Downstream traveling disturbances have a gain of one in the first and third quadrants, zero in the second and forth quadrants, and a value of 1/2 when either frequency is zero.

The dispersion analysis using an ideal downstream moving filter on the synthetic wavefront is shown in Figure 6.3 along side the dispersion of the unfiltered wavefront. All of the upstream traveling disturbances are removed and the disturbances at $\xi_x = 0$ m^{-1} are significantly reduced. Some of the stationary modes remain while only the acoustic and vibration signals that are propagating in the direction of flow remain. The aero-optical signal is clipped slightly at $\xi_x = 0$ due to the spatial width of the signal. The ratio of the time-averaged spatial-RMS of the filtered signal when compared to the aero-optic only signal was 1.24 while the unfiltered ratio was 1.53. When the filter was applied to only the aero-optic signal the ratio was 0.96. This filter method will retain any disturbance that is traveling in the direction of flow. Even with an ideal filter there is some slight attenuation of the aero-optical signal due to signal having some spectral width that crosses into upstream-moving portion of the dispersion plot.

6.3 Velocity Filtering

The dispersion plot shows flow structures that are traveling at a given speed as having a constant slope. A plane in the dispersion plot can be used to measure a flow structure's velocity in both x

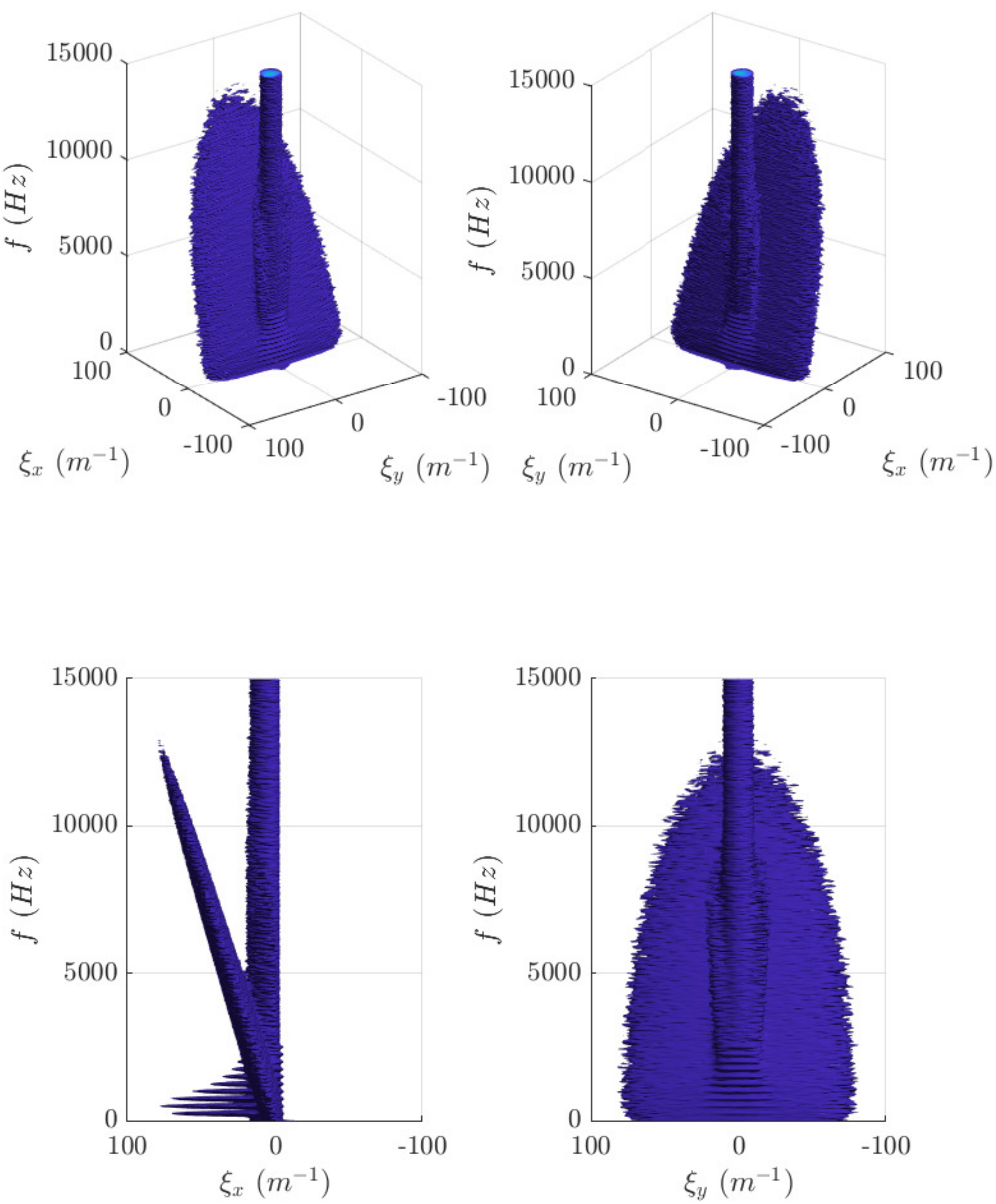

Figure 6.3. Dispersion isosurface of the synthetic wavefront with a downstream filter in place.

and y-directions. The distance from any given point in the dispersion plot to a plane described by the velocities v_x and v_y can be computed by

$$d = \frac{|v_x \xi_x + v_y \xi_y - f|}{\sqrt{v_x^2 + v_y^2 + 1}}. \tag{6.7}$$

A low-pass or high-pass filter can then be used to retain only disturbances that are traveling at that velocity, or to exclude those disturbances respectively.

A low-pass velocity-filter of the synthetic wavefront is shown in Figure 6.4. The filtered dispersion plot shows primarily only the aero-optic signal remains with some additional low-frequency content from the blade-passing frequency and harmonic disturbances as well as some stationary and acoustic disturbances. The ratio of the time-averaged spatial-RMS relative to that of the aero-optical only signal went from 1.53 in the unfiltered case to 1.01 in the filtered case. This method can provide a very effective way in quickly estimating the clean spatial-RMS of a contaminated wavefront.

Another use of the synthetic wavefront is measuring the speed of a broadband disturbance such as the aero-optical signal of a boundary layer. This is done by finding the velocity that maximizes the output spatial-RMS of the velocity filter, see Figure 6.5. In this case boundary layer speed was determined to be 163 m/s which corresponds to the design velocity of the synthetic signal of $0.8U$. If the velocity range used is to large, a false result can be obtained due to the inclusion of disturbance structures not related to the aero-optical signal. For signals that have a mean-velocity component that is not aligned with an axis both velocity components can be varied as shown in Figure 6.6. In this case a variable low-pass velocity filter was employed with a high-pass spatial filter operating in the radial direction. This helped eliminate some of the low-frequency stationary disturbances as well as some of the disturbances related to the blade-passing frequency. The velocity was measured using the optical disturbances in the dispersion plot to be approximately 207 m/s in the x-direction and -17 m/s in the y-direction.

6.4 Basic Filter Summary

Three different basic wavefront filters were shown and discussed in this chapter. The temporal filter is most useful when separating an optical wavefront into frequency bands. Adaptive optics system performance can be evaluated by using both high-pass and low-pass temporal filters. High-pass filters can be used to determine a systems performance that cannot be corrected while low-pass

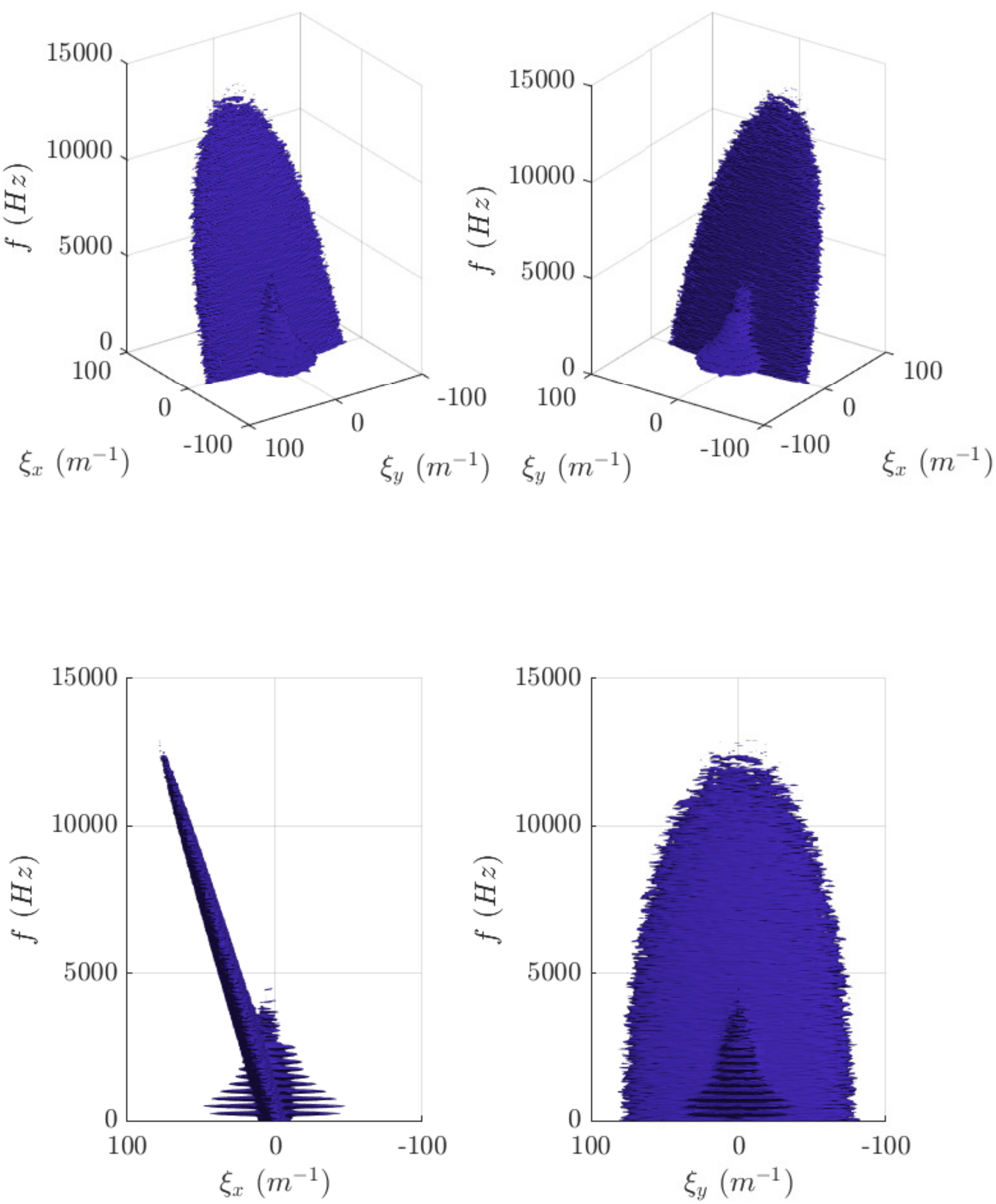

Figure 6.4. Dispersion isosurface of the synthetic wavefront with a low-pass velocity-filter in place.

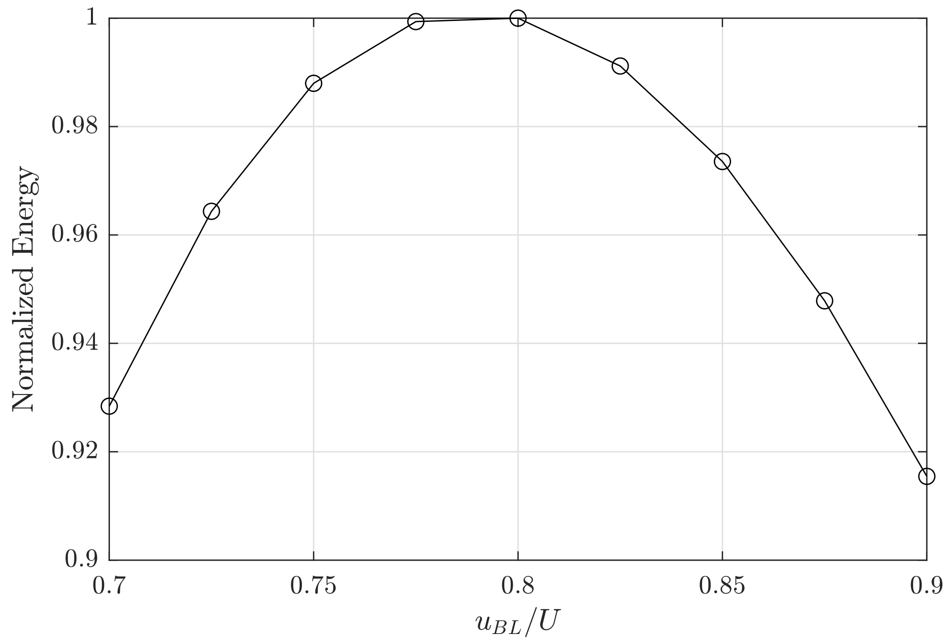

Figure 6.5. Velocity low-pass filter used to determine the mean disturbance velocity. The maximum value corresponds with the actual value used in the creation of the synthetic wavefront.

filters can be used to sizing the travel of active optical components. Band-pass filters are helpful in analyzing a wavefront over a narrow-band to examine the optical aberrations at specific frequencies that significantly contribute to the overall optical disturbance.

Filters that separate upstream and downstream-moving disturbances are useful as most of the optical contamination comes from acoustic signals that are traveling upstream form a wind-tunnel fan. These filters would also be useful for separating out an aero-optical signal that has a broad range of velocities that can occur in a span wise measurement of a boundary layer. Use some of sontag's data and site his dissertation.

The velocity filter is the most useful for isolating the aero-optical portion of a wavefront measurement given the aero-optical signal has a fairly narrow and constant velocity range. By using this filter to maximize the power over a range of velocities it can be used to measure the speed in both x and y-directions of an optical disturbance.

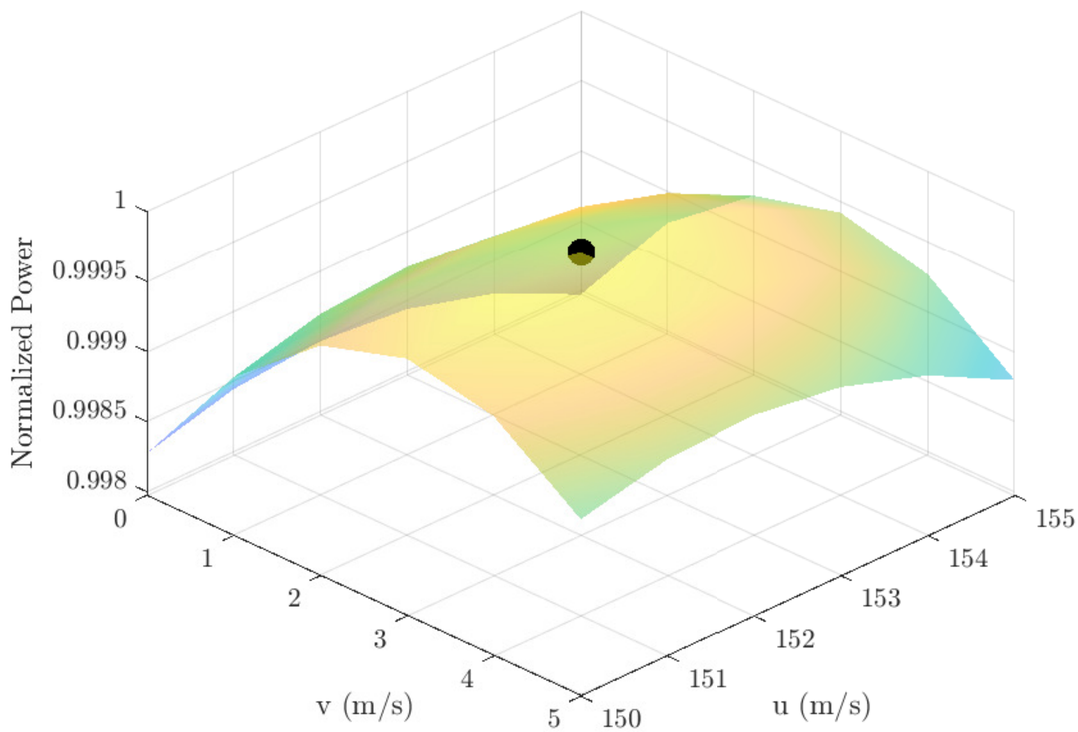

Figure 6.6. Velocity low-pass filter used to determine the mean disturbance velocity of measured data presented in Figure **??**. The velocity in the x-direction was measured to be 207 m/s and -17 m/s in the y-direction.

CHAPTER 7

MULTIPLE SENSOR FILTERING TECHNIQUES

- Maybe combine Figures 7.4 and 7.5

The previous chapter investigated filtering optical wavefront corruption by applying a variety of filters to the wavefront in the multi-dimensional spectral domain. These techniques involve only data from the optical wavefront itself and user knowledge and experience to obtain filtered data. When additional data streams are available, such as from microphones or accelerators, a targeted filter mechanisms become available.

A previous study [25] focused on using the combination of linear stochastic estimation (LSE) and spectral proper orthogonal decomposition (SPOD) to remove vibration related contamination from aero-optical wind-tunnel measurements. This process along with optical tip and tilt removal showed approximately an 85% reduction in the measured $\mathrm{OPD}_{\mathrm{RMS}}$ by combining accelerator measurements with optical wavefront measurements.

7.1 Optical Tip and Tilt

Zernike polynomials are traditionally used for describing optical aberrations of a optical system [4]. These polynomials are defined on the unit circle and form a set of orthogonal functions,

$$Z_n^m(\rho,\theta) = R_n^m(\rho)\cos(m\theta) \tag{7.1}$$

where $R_n^m(\rho)$ is the radial basis function and $\cos(m\theta)$ is the angular basis function. For values of $-m$ the angular basis function becomes $\sin(m\theta)$. The radial basis function are developed from Jacobi polynomials but for purposes in this study, only a few simple ones will be used. An optical wavefront can be approximated by a summation of Zernike polynomials multiplied by their corresponding coefficients

$$\mathrm{WF} \approx \sum Z_j a_j. \tag{7.2}$$

The Noll naming scheme is an method of organizing the Zernike polynomials into a single notation of Z_j, along with normalizing each polynomial to have a spatial RMS equal to one [32]. The first three of these using the Noll naming scheme are piston, tip, and tilt. Piston is simply the average OPD value of the single wavefront frame

$$Z_1 = 1. \tag{7.3}$$

Tip and tilt are the best planar fit to the OPD along the x-axis and y-axis respectively where tip is

$$Z_2 = 2\rho \cos\theta, \tag{7.4}$$

and tilt is

$$Z_3 = 2\rho \sin\theta. \tag{7.5}$$

Once the coefficients for these modes are solved for they can be filtered out

$$WF^F = WF - \sum Z_j a_j. \tag{7.6}$$

7.2 LSE-SPOD

The LSE-SPOD technique starts with performing SPOD on the primary data set and then using the Fourier transforms of the additional sensor data to perform a filtering operation. The spectral proper orthogonal decomposition technique is described in detail by Schmidt and Colonius [39]. A schematic of the SPOD algorithm is shown in Figure 7.1. The algorithm begins by separating the original data set, Q, into a number of smaller blocks,

$$Q = \begin{bmatrix} | & | & & | \\ q^{(1)} & q^{(2)} & \cdots & q^{(N)} \\ | & | & & | \end{bmatrix}, \quad Q \in \mathbb{C}^{M \times N} \tag{7.7}$$

where M is the total number of degrees of freedom (number of spatial points times the block length in time) and N is the number of blocks. Each block is then Fourier Transformed in the temporal dimension or through all dimensions. Once in the frequency domain the data blocks are then

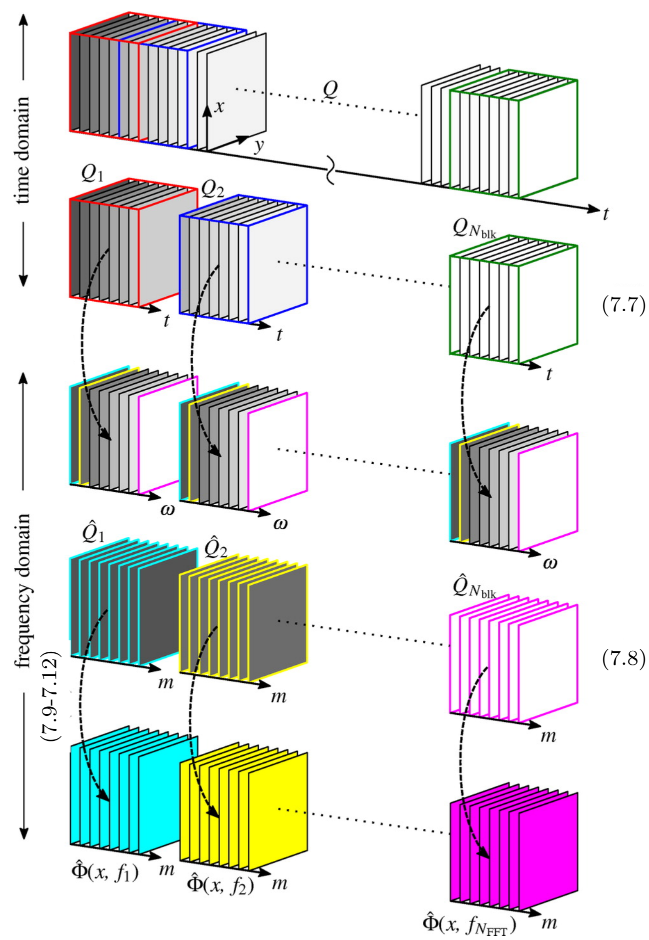

Figure 7.1. Schematic of the SPOD algorithm (taken from [39]). The numbers in parentheses denote the equations used.

reorganized by creating new blocks of identical temporal-frequencies,

$$\hat{Q} = \begin{bmatrix} | & | & & | \\ \hat{q}^{(1)} & \hat{q}^{(2)} & \dots & \hat{q}^{(N)} \\ | & | & & | \end{bmatrix}, \quad \hat{Q} \in \mathbb{C}^{M \times N} \tag{7.8}$$

where M is now the number of spatial points times the number of blocks and N is block length in time. Proper orthogonal decomposition is then performed separately on each temporal-frequency block via either traditional POD

$$\hat{C} = \frac{1}{N-1}\hat{Q}\hat{Q}^H, \tag{7.9}$$

$$\hat{C}W\hat{\Phi} = \hat{\Phi}\hat{\Lambda}, \tag{7.10}$$

or the method of snapshots,

$$\hat{Q}^H W \hat{Q}\hat{\Psi} = \hat{\Psi}\hat{\Lambda}, \tag{7.11}$$

$$\hat{\Phi} = \hat{Q}\hat{\Psi}, \tag{7.12}$$

where H denotes the Hermitian transpose, W is a weighting matrix, Φ is the set of deterministic spatial functions, Λ is the eigen-values, and Ψ is the coefficient matrix.

The linear stochastic estimation portion of the technique is described by Adrian [1]. This process uses a linear sum, L_{ij}, of additional measurements, y_j, to approximate a measured signal, x_i,

$$x_i^{LSE} = L_{ij}y_j, \tag{7.13}$$

where

$$L_{ij} = \langle x_i y_k \rangle \langle y_j y_k \rangle^{-1}. \tag{7.14}$$

When combined with SPOD, the estimation matrix, L, becomes

$$L = (\hat{\Psi}\hat{y}^H)(\hat{y}\hat{y}^H)^{-1}, \tag{7.15}$$

which allows for an estimated version of the coefficient matrix to be calculated

$$\hat{\Psi}^E = L\hat{y}. \tag{7.16}$$

The estimated coefficient matrix contains portions of the original signal that best resemble the additional sensor data. Assuming that the additional sensor data represents signal contamination of the original signal, a filtered coefficient matrix can be computed from the difference between the original and estimated coefficient matrix.

$$\hat{\Psi}^F = \hat{\Psi} - \hat{\Psi}^E. \tag{7.17}$$

A filtered signal, Q^F can be constructed by using the filtered coefficient matrix and the spatial functions,

$$\hat{Q} = \hat{\Psi}^F \hat{\Phi}^H. \tag{7.18}$$

7.3 Filtering Experimental Data

This filtering technique was tried with the same data sets that were shown in Figure 4.7. Both simultaneous accelerometer and microphone were made along side the optical wavefront measurements. The locations of some of the additional sensors are shown in Figure 7.2. Two microphones were used for ambient measurement (a ACO 7016B [11] and a Brüel & Kjær 4939 [7]), four microphones were used for test-section noise measurement (PCB 103B02 [33]), and ten accelerometers were located throughout the setup (PCB 352C33 [34]). One of the ambient microphones was mounted to the top of the optics bench facing the test-section and can be seen in Figure 7.2 just to the right of the primary lens and the other ambient microphone was hanging below the optics bench end towards the test-section.

The test-sections microphones were in groups of two either upstream or downstream from the optical beam by about 20-inches, with the upstream microphone locations viewable in Figure 7.2. The model installed in the test-section represents the outside of an aircraft fuselage with a 5-foot diameter and is angled to account for the aircraft's angle-of-attack for steady-level-flight at cruise. This results in the fuselage model being shifted approximately 2-inches higher from the test-section centerline upsteam at the microphone location. The duct microphones were placed about 2.75-inches from the model centerline.

There were six accelerometers attached to the test-section windows, with three being on each side. The locations of the three accelerometers on the model side can be seen in Figure 7.2, the three accelerometers on the other window used the opposite pattern (two high and one low). One accelerometer was placed on the primary lens (also shown) and one was placed in the center of the

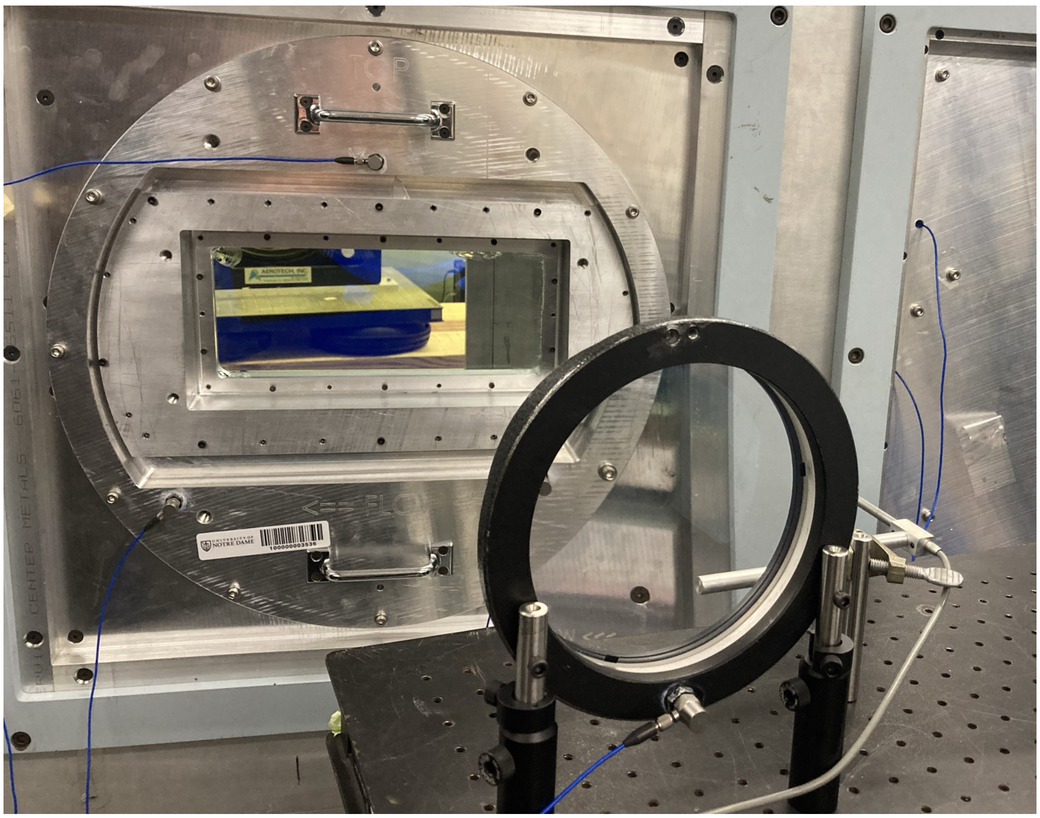

Figure 7.2. The locations of some of the additional sensors used in the LSE-SPOD filtering.

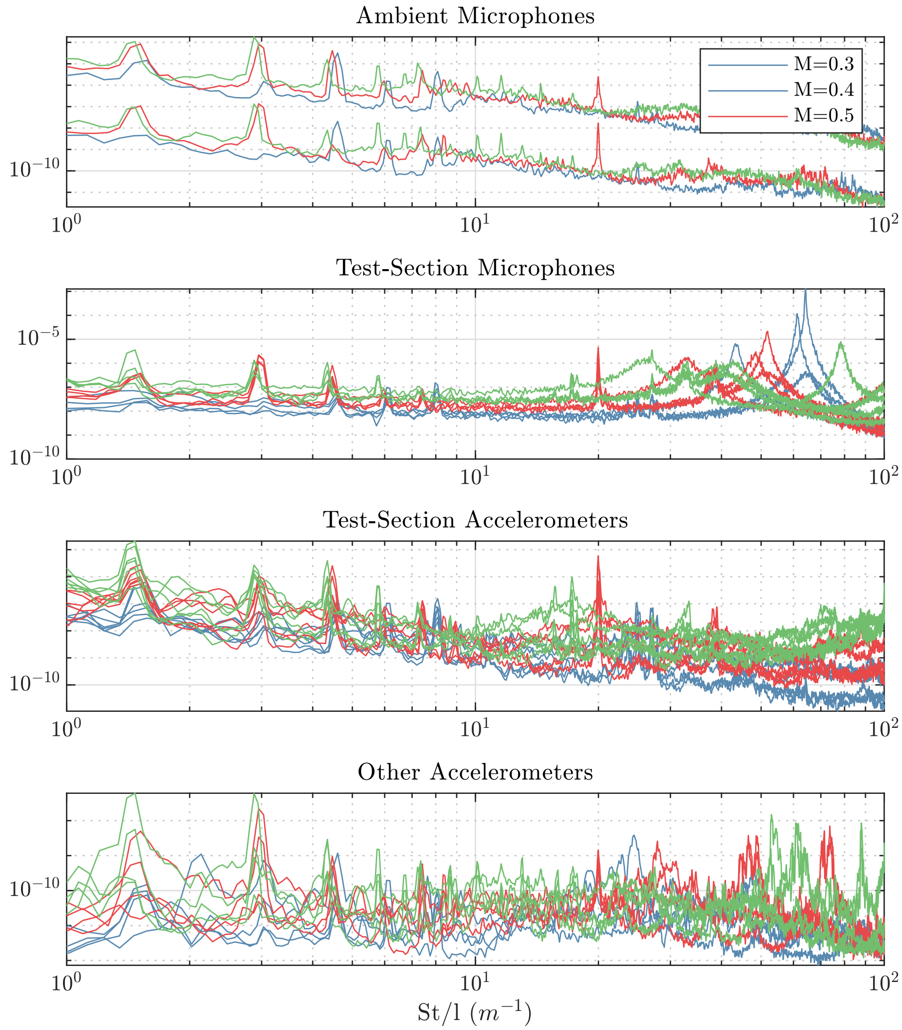

Figure 7.3. Power-spectra of the additional sensor measurements at the three Mach numbers tested. The x-axis is in Strouhal number per characteristic length (St/l).

optics bench. The last two accelerometers were located on the return mirror and oriented in a way to measure the tip and tilt of the return beam.

The power-spectra of all of the sensors at the three Mach numbers are shown in Figure 7.3. These plots are presented as Strouhal number per characteristic length with the different groups of sensors shown together. The blade-passing frequency for these data sets is at a St/l of approximately 3-m^{-1} with a clear and consistant narrow-band signal at for but the $M = 0.3$ run which has a slight increase in signal for some of the sensors. For the $M = 0.5$ case there is an additional strong narrow-band signal at 20-m^{-1} for all sensors and a slightly broader signal at 38-m^{-1} that is only present in the test-section mounted sensors that may be due to extra fan vibration which is currently limiting

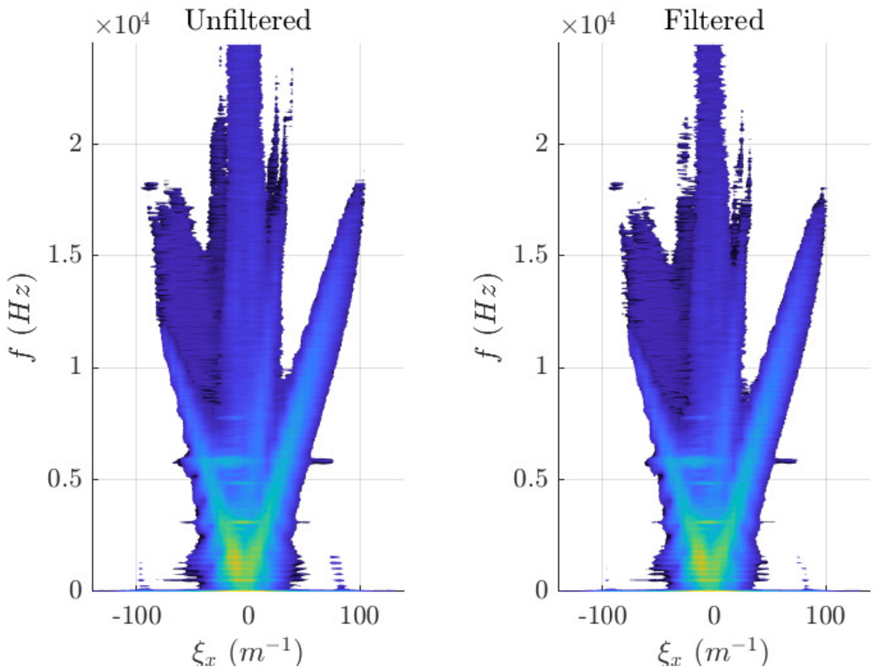

Figure 7.4. A multi-dimensional power spectrum of an unfiltered wavefront and the same wavefront filtered with the LSE-SPOD method using all 16 additional microphone or accelerometer measurements.

the top speed of the wind-tunnel. The test-section mounted microphones are picking up boundary layer accoustic noise above St/l of approximately 20-m^{-1}.

Two variants of this filtering technique were tried. The first was a standard LSE-SPOD technique in which the spectral POD was performed on the data set that was Fourier transformed in time only. The second will be referred to here as LSE-MSPOD, in which the spectral POD was applied to a data set in which the Fourier transformed was performed in all dimensions of space and time. Figures 7.4 and 7.5 show multi-dimensional power spectrum plots at a temporal block length of 2^{10} with no overlap. These plots show a combination of the isosurface and horizontal moving plane-wave slice. Both of these methods preformed effectively identical to one another with a drop of 14.2% drop in overall RMS value of the filtered wavefront (both time and space). There is a significant drop in the signal at the blade-passing frequency and its harmonics, especially at the higher spatial frequencies. The stationary signal information is also significantly reduced along with the high temporal-frequency acoustic signal. The aero-optical boundary layer signal is also partially reduced, which is most noticeable at higher temporal-frequencies. Some of this lost signal can be restored by increasing the overlap of the temporal frequency blocks, but this also restores some of

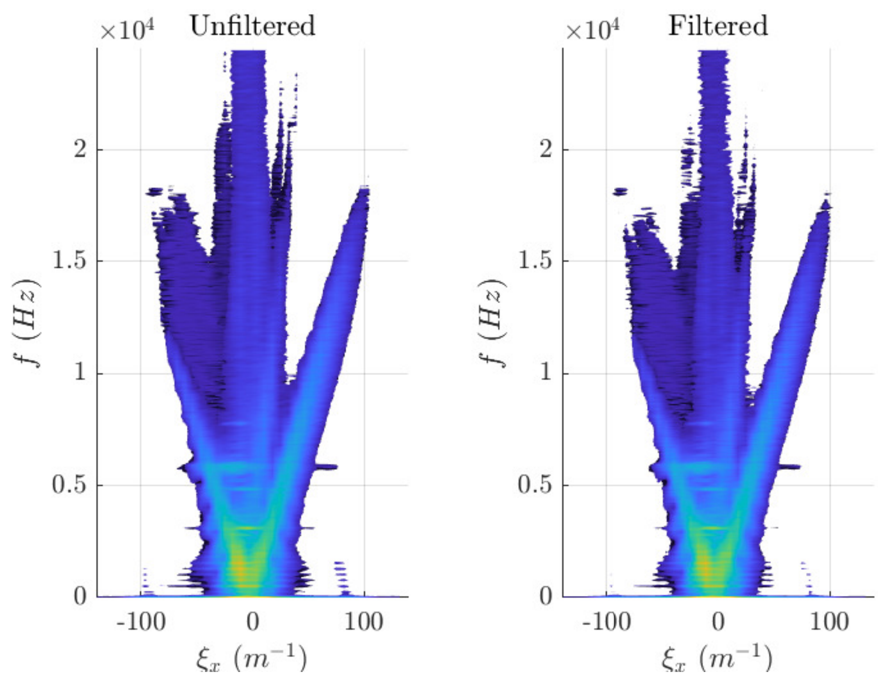

Figure 7.5. A multi-dimensional power spectrum of an unfiltered wavefront and the same wavefront filtered with the LSE-MSPOD method using all 16 additional microphone or accelerometer measurements.

TABLE 7.1

$\mathrm{OPD_{RMS}}$ (μm) COMPARISON USING DIFFERENT COMBINATIONS OF ADDITIONAL SENSOR INFORMATION IN THE LSE-MSPOD FILTERING PROCESS.

	M=0.3	M=0.4	M=0.5
Original	0.0561	0.0521	0.0824
Tip/Tilt Removal	0.0120(78.6%)	0.0195(62.6%)	0.0291(64.7%)
Accelerometers	0.0102(81.8%)	0.0168(67.7%)	0.0251(69.5%)
Ambient Microphones	0.0103(81.7%)	0.0170(67.3%)	0.0254(69.1%)
Duct Microphones	0.0103(81.6%)	0.0170(67.3%)	0.0255(69.0%)
Test-Section Sensors	0.0103(81.6%)	0.0168(67.8%)	0.0252(69.4%)
All Sensors	0.0099(82.3%)	0.0163(68.8%)	0.0242(70.6%)
Velocity Filter	0.0090(83.9%)	0.0146(72.1%)	0.0217(73.7%)
+All Sensors	0.0075(86.7%)	0.0122(76.7%)	0.0181(78.0%)

the unwanted high temporal-frequency contamination.

Table 7.1 shows the time averaged $\mathrm{OPD_{RMS}}$ of three different data sets at a beam angle through the test-section of 90°. The data sets were at Mach numbers of 0.3, 0.4 and 0.5 that had an unfiltered $\mathrm{OPD_{RMS}}$ of 0.0561, 0.0521, and 0.0824 μm respectively. Note that in the raw processed wavefronts for the Mach number of 0.3 was higher than the 0.4 case. There was a significant drop of between 62.6 and 78.6% in the $\mathrm{OPD_{RMS}}$ by removing the Zernike modes corresponding to tip and tilt. It is at this point the Mach number of 0.4 case has a higher $\mathrm{OPD_{RMS}}$ than the 0.3 case as would be expected Reference an equation or source (probably a non-dimensionalization equation).

Five different combinations of additional sensors were examined for filtering with the LSE-MSPOD process. The first set was all of the accelerometers which resulted in an additional drop in $\mathrm{OPD_{RMS}}$ of between 3 and 5%. The second and third sets used either the ambient or duct microphones and those sets had slightly less reduction than the accelerometers resulted in. The forth set was the test-section sensors that was comprised of six window mounted accelerometers and four duct mounted microphones. This set of sensors preformed the same as all of the accelerometers, while the use of all of the additional sensors in the last set performed the best, with an additional reduction in $\mathrm{OPD_{RMS}}$ of 4 to 6% from the tip/tilt removal cases.

A velocity filter was also tried in addition to just the tip/tilt removal or in conjunction with tip/tilt and all the sensors being used in the LSE-MSPOD process. The velocity filter performed better than the all sensors removal case by an additional 1.5 to 3%. When all sensors were used with LSE-MSPOD on the velocity filtered wavefronts an additional 3 to 4% of the $\mathrm{OPD}_{\mathrm{RMS}}$ was removed from just the velocity filtered case or an additional 8.1% reduction for only doing tip/tilt removal on the Mach number of 0.3 case or 14.1 and 13.3% reduction for the 0.4 and 0.5 Mach number cases.

Using either the temporal or multi-dimensional version of the LSE-SPOD filtering technique can help remove some of the narrow-band acoustic and vibration reduction in an optical wavefront. This additional reduction does seem to be somewhat tied to the number of sensors used with more sensors having a greater impact on the signal reduction. Since the vibrations and acoustics have the same primary source, the wind-tunnel fan, they seems to do a relatively equivalent job at filtering the optical contamination. Accelerometers have a benefit easier installation but the microphones do not necessary have to be installed inside of the wind-tunnel.

APPENDIX A

SAMPLE CODE

Listing A.1: A simple function for computing the power spectra for vector x given an arbitrary windowing function.

```
function [sxx,freq] = simpleSXX(x,fsamp,window)
N = length(x);
x = reshape(x,1,N);
switch nargin
    case 1
        window = reshape(hann(N),1,N);
        fsamp = 1;
    case 2
        window = reshape(hann(N),1,N);
end
if isempty(fsamp)
    fsamp = 1;
end
if isa(window,'function_handle')
    window = reshape(window(N),1,N);
end
cw = 1/sqrt(sum(window.^2,'all')/N);
sxx = fftshift((abs(cw*fft(x.*window))).^2)/N/fsamp;
freq = (-0.5:1/N:0.5-1/N)*fsamp;
end
```

Listing A.2: A simple function for computing the dispersion or n-dimensional power spectra of x given an arbitrary windowing function.

```
function [sxx,frequency] = simpleSXXn(x,sampleRate,window)
% Check Number of Inputs - Select Default Options
switch nargin
    case 1
        window = 1;
        sampleRate = ones(1,ndims(x));
```

```
    case 2
        window = 1;
end
% Check if 'sampleRate' is Empty
if isempty(sampleRate)
    sampleRate = ones(1,ndims(x));
end
% Check if 'window' is a Function Handle
N = size(x);
if isa(window,'function_handle')
    wfun = window;
    window = wfun(N(1));
    for aa=2:ndims(x)
        window = window.*permute(wfun(N(aa)),aa:-1:1);
    end
end
% Calculate Window Correction
if window==1
    cw = 1;
else
    cw = 1/sqrt(sum(window.^2,'all')/numel(x));
end
% Calculate Power Spectra
sxx = fftshift((abs(cw*fftn(x.*window))).^2)/numel(x)/prod(sampleRate);
% Calculate Frequency Ranges
frequency{1} = (-0.5:1/N(1):0.5-1/N(1))'*sampleRate(1);
for aa=2:ndims(x)
    frequency{aa} = permute((-0.5:1/N(aa):0.5-1/N(aa))'*sampleRate(aa),aa:-1:1);
end
end
```

Listing A.3: MATLAB code used to generate the synthetic wavefront used in Chapter **??**.

```
close all; clc; clearvars; %#ok<*UNRCH>

sampleRate = [200*[1 1] 30000];
nSamples = 2.^[6 6 13];
c = 340;
M = 0.6;
uBL_u = 0.8;
surfaceStrength = -14.5;
```

```
nMakePlots = 0;     % 0: off, 1: plot, 2: plot and save, 3: Combo Only

% Frequency Space
freq.x = (-0.5:1/nSamples(2):0.5-1/nSamples(2))*sampleRate(2);
freq.y = reshape((-0.5:1/nSamples(1):0.5-1/nSamples(1))*sampleRate(1),nSamples(1),1,1);
freq.t = reshape((-0.5:1/nSamples(3):0.5-1/nSamples(3))*sampleRate(3),1,1,nSamples(3));
freq.rho = sqrt(freq.x.^2+freq.y.^2);
freq.theta = atan2(freq.y,freq.x);

%%%% Aero-Optics Signal
AO.ellipsoid = [8 90 175];
AO.strength = -14.5;
AO.slope = -0.13;
% Calculations
AO.speed = c*M*uBL_u;
b = 1/2/AO.strength*(AO.strength^2-1/AO.slope^2);
AO.WF = zeros(nSamples);
XR = freq.x*cos(atan(-1/AO.speed))+freq.t*sin(atan(-1/AO.speed));
YR = freq.y;
TR = -freq.t*sin(atan(-1/AO.speed))+freq.x*cos(atan(-1/AO.speed));
R = sqrt((XR/AO.ellipsoid(1)).^2+(YR/AO.ellipsoid(2)).^2+(TR/AO.ellipsoid(3)).^2);
AO.WF = 10.^(b-sqrt(R.^2/AO.slope^2+b^2));
clear b XR YR TR R;

%%%% White-Noise Stationary Signal
SN.rho0 = 5;
SN.strength = -14.5;
SN.slope = -0.175;
% Calculations
b = 1/2/SN.strength*(SN.strength^2-1/SN.slope^2);
SN.WF = 10.^(b-sqrt(repmat((freq.rho./(SN.rho0.*sqrt(10-6*cos(2*freq.theta+pi)))).^2,1,1,nSamples(3))/SN.slope^2+b^2));
clear b;

%%%% Blade Pass Frequency Contamination
BPF.freq = 500;
BPF.harmonic = 0.5:0.5:5;
BPF.rho0 = 20;
BPF.tThickness = 100;
```

```
BPF.strength = -14;
BPF.slope = -0.13;
BPF.cutoff = 500;
BPF.aspectRatio = 1;
% Calculations
b = 1/2/BPF.strength*(BPF.strength^2-1/BPF.slope^2);
BPF.WF = zeros(nSamples);
for aa=1:length(BPF.harmonic)
    R = sqrt((sqrt(freq.x.^2+(BPF.aspectRatio*freq.y).^2)./(BPF.rho0/sqrt(1+((BPF.freq*BPF.harmonic(aa)-BPF.freq)/BPF.cutoff).^2)*sqrt(10-6*cos(2*freq.theta+pi)))).^2+((freq.t-BPF.freq*BPF.harmonic(aa))/BPF.tThickness).^2);
    BPF.WF = BPF.WF+10.^(b-sqrt(R.^2/BPF.slope^2+b^2));
    R = sqrt((sqrt(freq.x.^2+(BPF.aspectRatio*freq.y).^2)./(BPF.rho0/sqrt(1+((BPF.freq*BPF.harmonic(aa)-BPF.freq)/BPF.cutoff).^2)*sqrt(10-6*cos(2*freq.theta+pi)))).^2+((freq.t+BPF.freq*BPF.harmonic(aa))/BPF.tThickness).^2);
    BPF.WF = BPF.WF+10.^(b-sqrt(R.^2/BPF.slope^2+b^2));
end
clear b R;

%%%% Zero Frequency Contamination
ZERO.rho0 = 25;
ZERO.tThickness = 50;
ZERO.strength = -14.5;
ZERO.slope = -0.5;
ZERO.aspectRatio = 0.55;
% Calculations
b = 1/2/ZERO.strength*(ZERO.strength^2-1/ZERO.slope^2);
R = sqrt((sqrt(freq.x.^2+(ZERO.aspectRatio*freq.y).^2)./(ZERO.rho0*sqrt(10-6*cos(2*freq.theta+pi)))).^2+(freq.t/ZERO.tThickness).^2);
ZERO.WF = 10.^(b-sqrt(R.^2/ZERO.slope^2+b^2));
clear b R;

%%%% Acoustic Cone Signal
CONE.strength = [-13 -16];
CONE.slope = -0.3;
CONE.thickness = 8;
CONE.lowPassRho = 200;
CONE.lowPassX = 115;
% Calculations
freqMod.x0 = sin(0.5*atan(1/c/(M+1))+0.5*atan(1/c/(M-1)))*freq.t;
freqMod.y0 = 0;
```

```
freqMod.ax = sin(0.5*atan(1/c/(M+1))-0.5*atan(1/c/(M-1)))*freq.t;
freqMod.ay = sin(atan(1/c))*freq.t;
freqMod.theta = atan2(freq.y-freqMod.y0,freq.x-freqMod.x0);
freqMod.rho = (sqrt((freq.x-freqMod.x0).^2+(freq.y-freqMod.y0).^2)./sqrt((freqMod.ax.*cos(freqMod.theta)).^2+(freqMod.ay.*sin(freqMod.theta)).^2)-1).*sqrt((freqMod.ax.*cos(freqMod.theta)).^2+(freqMod.ay.*sin(freqMod.theta)).^2)/CONE.thickness;
freqMod.rho(:,:,end/2+1) = freq.rho(:,:)/CONE.thickness;
b1 = ((CONE.strength(2)-CONE.strength(1))/(sampleRate(3)/2)*abs(freq.t)+CONE.strength(1));
b = 1/2./b1.*(b1.^2-1/CONE.slope^2);
CONE.WF = 10.^(b-sqrt(freqMod.rho.^2/CONE.slope^2+b.^2));
CONE.WF = CONE.WF.*sqrt(1./(1+(freqMod.rho/CONE.lowPassRho).^2));
CONE.WF = CONE.WF.*sqrt(1./(1+(freq.x/CONE.lowPassX).^2));
clear freqMod b b1;

%%%% Background Noise
BACK.strength = -18;
BACK.deviation = 0.75;
% Calculations
BACK.WF = 10.^(randn(nSamples)*BACK.deviation+BACK.strength);
BACK.WF(2:nSamples(1),2:nSamples(2),nSamples(3)/2+2:nSamples(3)) = flip(flip(flip(BACK.WF(2:nSamples(1),2:nSamples(2),2:nSamples(3)/2),1),2),3);

%%%% Sound and Vibration
SV.WF = BPF.WF+ZERO.WF+CONE.WF;

%%%% Plot
views = [-125 25; -55 25; 180 0; 270 0];
f1 = figure(1);
for aa=1:4
    subplot(2,2,aa)
    patch(isosurface(freq.x,freq.y,freq.t,AO.WF,10^surfaceStrength),'edgecolor','none','facecolor','red','facelighting','gouraud');
    patch(isosurface(freq.x,freq.y,freq.t,SN.WF,10^surfaceStrength),'edgecolor','none','facecolor','blue','facelighting','gouraud');
    patch(isosurface(freq.x,freq.y,freq.t,BPF.WF,10^surfaceStrength),'edgecolor','none','facecolor','green','facelighting','gouraud');
    patch(isosurface(freq.x,freq.y,freq.t,ZERO.WF,10^surfaceStrength),'edgecolor','none','facecolor','yellow','facelighting','gouraud');
    patch(isosurface(freq.x,freq.y,freq.t,CONE.WF,10^surfaceStrength),'edgecolor','none','facecolor','magenta','facelighting','gouraud');
```

```
    patch(isosurface(freq.x,freq.y,freq.t,BACK.WF,10^surfaceStrength),'edgecolor','none','facecolor','cyan','facelighting','gouraud');
    grid on;
    hold on;
    daspect([1 1 sampleRate(3)/sampleRate(1)/3]);
    xlim(sampleRate(1)/2*[-1 1]);
    ylim(sampleRate(2)/2*[-1 1]);
    zlim(sampleRate(3)/2*[0 1]);
    camlight;
    xlabel('$\xi_x\ (m^{-1})$','Interpreter','Latex');
    ylabel('$\xi_y\ (m^{-1})$','Interpreter','Latex');
    zlabel('$f\ (Hz)$','Interpreter','Latex');
%     title('Synthetic Signal','Interpreter','Latex');
    f1.Children(1).TickLabelInterpreter = 'latex';
    view(views(aa,:));
    camlight;
end
f1.Units = 'inches';
f1.Position = [1 1 6 8];
% Save Plot
saveas(f1,'synthetic_wavefront.eps','epsc');

%%%% Animation
nFrames = 150;
theta = (0:nFrames-1)/(nFrames)*4*pi;
az = rad2deg(theta);
el = 25*sin(theta/2);

f2 = figure(2);
scolor = parula(2);
patch(isosurface(freq.x,freq.y,freq.t(end/2+1:end),AO.WF(:,:,end/2+1:end),10^surfaceStrength),'edgecolor','none','facecolor','red','facelighting','gouraud');
patch(isocaps(freq.x,freq.y,freq.t(end/2+1:end),AO.WF(:,:,end/2+1:end),10^surfaceStrength,'all'),'edgecolor','none','facecolor','red','facelighting','gouraud');
patch(isosurface(freq.x,freq.y,freq.t(end/2+1:end),SN.WF(:,:,end/2+1:end),10^surfaceStrength),'edgecolor','none','facecolor','blue','facelighting','gouraud');
patch(isocaps(freq.x,freq.y,freq.t(end/2+1:end),SN.WF(:,:,end/2+1:end),10^surfaceStrength,'all'),'edgecolor','none','facecolor','blue','facelighting','gouraud');
```

```
patch(isosurface(freq.x,freq.y,freq.t(end/2+1:end),BPF.WF(:,:,end/2+1:end),10^
    surfaceStrength),'edgecolor','none','facecolor','green','facelighting','gouraud'
    );
patch(isocaps(freq.x,freq.y,freq.t(end/2+1:end),BPF.WF(:,:,end/2+1:end),10^
    surfaceStrength,'all'),'edgecolor','none','facecolor','green','facelighting','
    gouraud');
patch(isosurface(freq.x,freq.y,freq.t(end/2+1:end),ZERO.WF(:,:,end/2+1:end),10^
    surfaceStrength),'edgecolor','none','facecolor','yellow','facelighting','gouraud
    ');
patch(isocaps(freq.x,freq.y,freq.t(end/2+1:end),ZERO.WF(:,:,end/2+1:end),10^
    surfaceStrength,'all'),'edgecolor','none','facecolor','yellow','facelighting','
    gouraud');
patch(isosurface(freq.x,freq.y,freq.t(end/2+1:end),CONE.WF(:,:,end/2+1:end),10^
    surfaceStrength),'edgecolor','none','facecolor','magenta','facelighting','
    gouraud');
patch(isocaps(freq.x,freq.y,freq.t(end/2+1:end),CONE.WF(:,:,end/2+1:end),10^
    surfaceStrength,'all'),'edgecolor','none','facecolor','magenta','facelighting','
    gouraud');
patch(isosurface(freq.x,freq.y,freq.t(end/2+1:end),BACK.WF(:,:,end/2+1:end),10^
    surfaceStrength),'edgecolor','none','facecolor','cyan','facelighting','gouraud')
    ;
patch(isocaps(freq.x,freq.y,freq.t(end/2+1:end),BACK.WF(:,:,end/2+1:end),10^
    surfaceStrength,'all'),'edgecolor','none','facecolor','cyan','facelighting','
    gouraud');
grid on;
daspect([1 1 50]);
xlim(sampleRate(1)/2*[-1 1]);
ylim(sampleRate(2)/2*[-1 1]);
zlim(sampleRate(3)/2*[0 1]);
xlabel('$\xi_x\ (m^{-1})$','Interpreter','Latex');
ylabel('$\xi_y\ (m^{-1})$','Interpreter','Latex');
zlabel('$f\ (Hz)$','Interpreter','Latex');
f2.Children(1).TickLabelInterpreter = 'latex';
f2.Units = 'inches';
f2.Position = [1 1 5.5 6.25];
cl = camlight;

filename = 'synthetic_wavefront.gif';
frameRate = 15;
for aa=1:nFrames-1
    view(az(aa),el(aa));
```

```
    camlight(cl);
    drawnow;
    frame = getframe(f2);
    im = frame2im(frame);
    [imind,cm] = rgb2ind(im,256);
    if aa==1
        imwrite(imind,cm,filename,'gif','Loopcount',inf,'DelayTime',1/frameRate);
    else
        imwrite(imind,cm,filename,'gif','WriteMode','append','DelayTime',1/frameRate
            );
    end
end

%%%% Make Wavefronts
[wf.x,wf.y] = meshgrid(0.975*(-1:2/(nSamples(1)-1):1),0.975*(-1:2/(nSamples(2)-1):1)
    );
wf.rho = sqrt(wf.x.^2+wf.y.^2);
wf.theta = atan2(wf.y,wf.x);
wf.mask = ones(size(wf.x));
wf.mask(wf.rho>1) = NaN;
wf.x = wf.x.*wf.mask;
wf.y = wf.y.*wf.mask;
wf.rho = wf.rho.*wf.mask;
wf.theta = wf.theta.*wf.mask;
wf.sampleRate = sampleRate;
% Aero-Optics Signal
phase = pi*(2*rand(nSamples)-1);
phase(nSamples(1)/2+1,nSamples(2)/2+1,nSamples(3)/2+1) = 0;
phase(2:nSamples(1),2:nSamples(2),nSamples(3)/2+2:nSamples(3)) = -flip(flip(flip(
    phase(2:nSamples(1),2:nSamples(2),2:nSamples(3)/2),1),2),3);
wf.AO = real(ifftn(ifftshift(sqrt((AO.WF)*prod(sampleRate)*numel(AO.WF)).*exp(1i*
    phase))));
wf.AO = wf.AO.*wf.mask;
clear phase;
% White-Noise Stationary Signal
phase = pi*(2*rand(nSamples)-1);
phase(nSamples(1)/2+1,nSamples(2)/2+1,nSamples(3)/2+1) = 0;
phase(2:nSamples(1),2:nSamples(2),nSamples(3)/2+2:nSamples(3)) = -flip(flip(flip(
    phase(2:nSamples(1),2:nSamples(2),2:nSamples(3)/2),1),2),3);
wft.SN = real(ifftn(ifftshift(sqrt((SN.WF)*prod(sampleRate)*numel(SN.WF)).*exp(1i*
    phase))));
```

```
wft.SN = wft.SN.*wf.mask;
clear phase;
% Background Noise
phase = pi*(2*rand(nSamples)-1);
phase(nSamples(1)/2+1,nSamples(2)/2+1,nSamples(3)/2+1) = 0;
phase(2:nSamples(1),2:nSamples(2),nSamples(3)/2+2:nSamples(3)) = -flip(flip(flip(
    phase(2:nSamples(1),2:nSamples(2),2:nSamples(3)/2),1),2),3);
wft.BACK = real(ifftn(ifftshift(sqrt((BACK.WF)*prod(sampleRate)*numel(BACK.WF)).*exp
    (1i*phase))));
wft.BACK = wft.BACK.*wf.mask;
clear phase;
% Sound and Vibration
phase = pi*(2*rand(nSamples)-1);
phase(nSamples(1)/2+1,nSamples(2)/2+1,nSamples(3)/2+1) = 0;
phase(2:nSamples(1),2:nSamples(2),nSamples(3)/2+2:nSamples(3)) = -flip(flip(flip(
    phase(2:nSamples(1),2:nSamples(2),2:nSamples(3)/2),1),2),3);
wft.SV = real(ifftn(ifftshift(sqrt((SV.WF)*prod(sampleRate)*numel(SV.WF)).*exp(1i*
    phase))));
wft.SV = wft.SV.*wf.mask;
clear phase;
% Total
wf.wf = wf.AO+wft.SN+wft.BACK+wft.SV;
% Save
% save('synthetic_wavefront.mat','wf');
% disp('File Saved');
```

Listing A.4: MATLAB code used to filter wavefronts in Chapter ??.

```
function [wf] = WFfilter(wf,varargin)
%WFFILTER Summary of this function goes here
%   Detailed explanation goes here

% Check Number of Inputs
if mod(nargin,2)==0 || nargin<3
    error('Invalid Number of Inputs');
end
% Zero-Out NaN Values
mask = double(~isnan(wf(:,:,1)));
mask(mask==0) = NaN;
% disp(mask);
wf(isnan(wf)) = 0;
```

```
% 3D-FFT
wf = fftshift(fftn(wf));
% Calculate Frequency
BlockSize = size(wf);
Frequency.y = reshape(-1/2:1/BlockSize(1):1/2-1/BlockSize(1) ,[] ,1);
Frequency.x = reshape(-1/2:1/BlockSize(2):1/2-1/BlockSize(2) ,1 ,[]);
Frequency.t = reshape(-1/2:1/BlockSize(3):1/2-1/BlockSize(3) ,1 ,1 ,[]);
Frequency.rho = sqrt(Frequency.x.^2+Frequency.y.^2);
% Filters
for aa=1:length(varargin)/2
    switch lower(varargin{2*aa-1})
        case 'time-highpass'
            if length(varargin{2*aa})==1
                n = 1;
            else
                n = varargin{2*aa}(2);
            end
            [b,a] = butter(n,varargin{2*aa}(1),'high','s');
            gain = abs(reshape(freqs(b,a,reshape(Frequency.t,1,[])),1,1,[]));
            clear b a;
        case 'time-lowpass'
            if length(varargin{2*aa})==1
                n = 1;
            else
                n = varargin{2*aa}(2);
            end
            [b,a] = butter(n,varargin{2*aa}(1),'low','s');
            gain = abs(reshape(freqs(b,a,reshape(Frequency.t,1,[])),1,1,[]));
            clear b a;
        case {'time-passband' 'time-bandpass'}
            if length(varargin{2*aa})==2
                n = 1;
            else
                n = varargin{2*aa}(3);
            end
            [b,a] = butter(n,varargin{2*aa}(1:2),'bandpass','s');
            gain = abs(reshape(freqs(b,a,reshape(Frequency.t,1,[])),1,1,[]));
            clear b a;
        case {'time-bandstop' 'time-stop'}
            if length(varargin{2*aa})==2
                n = 1;
```

```
            else
                n = varargin{2*aa}(3);
            end
            [b,a] = butter(n,varargin{2*aa}(1:2),'stop','s');
            gain = abs(reshape(freqs(b,a,reshape(Frequency.t,1,[])),1,1,[]));
            clear b a;
        case 'space-highpass'
            if length(varargin{2*aa})==1
                n = 1;
            else
                n = varargin{2*aa}(2);
            end
            gain = sqrt(1./(1+(Frequency.rho/varargin{2*aa}(1)).^(-2*n)));
        case 'space-lowpass'
            if length(varargin{2*aa})==1
                n = 1;
            else
                n = varargin{2*aa}(2);
            end
            gain = sqrt(1./(1+(Frequency.rho/varargin{2*aa}(1)).^(+2*n)));
        case 'velocity-highpass'
            if length(varargin{2*aa})==3
                n = 1;
            else
                n = varargin{2*aa}(4);
            end
            dist = abs(varargin{2*aa}(1)*Frequency.x+varargin{2*aa}(2)*Frequency.y-
                Frequency.t)/sqrt((varargin{2*aa}(1))^2+(varargin{2*aa}(2))^2+1);
            gain = sqrt(1./(1+(dist/varargin{2*aa}(3)).^(-2*n)));
        case 'velocity-lowpass'
            if length(varargin{2*aa})==3
                n = 1;
            else
                n = varargin{2*aa}(4);
            end
            dist = abs(varargin{2*aa}(1)*Frequency.x+varargin{2*aa}(2)*Frequency.y-
                Frequency.t)/sqrt((varargin{2*aa}(1))^2+(varargin{2*aa}(2))^2+1);
            gain = sqrt(1./(1+(dist/varargin{2*aa}(3)).^(+2*n)));
        case 'x-space'
            switch length(varargin{2*aa})==1
                case 1
```

```
                    n = 1;
                    threeDB = 0;
                case 2
                    n = varargin{2*aa}(2);
                    threeDB = 0;
                case 3
                    n = varargin{2*aa}(2);
                    threeDB = varargin{2*aa}(3);
            end
            if isempty(n)
                n = 1;
            end
            if threeDB
                gain = 1./(1+exp(-n*(Frequency.x-varargin{2*aa}(1)-log(sqrt(2)-1)/n)));
            else
                gain = 1./(1+exp(-n*(Frequency.x-varargin{2*aa}(1))));
            end
        case 'y-space'
            switch length(varargin{2*aa})==1
                case 1
                    n = 1;
                    threeDB = 0;
                case 2
                    n = varargin{2*aa}(2);
                    threeDB = 0;
                case 3
                    n = varargin{2*aa}(2);
                    threeDB = varargin{2*aa}(3);
            end
            if isempty(n)
                n = 1;
            end
            if threeDB
                gain = 1./(1+exp(-n*(Frequency.y-varargin{2*aa}(1)-log(sqrt(2)-1)/n)));
            else
                gain = 1./(1+exp(-n*(Frequency.y-varargin{2*aa}(1))));
            end
        case 'forward-moving'
            kx = BlockSize(2);
```

```
                kt = BlockSize(3);
                if ~isempty(varargin{2*aa})
                    kx = kx*varargin{2*aa}(1);
                    kt = kt*varargin{2*aa}(2);
                end
                gain = (2./(1+exp(-kx*Frequency.x))-1).*(2./(1+exp(-kt*Frequency.t))-1)/2+0.5;
            case 'backward-moving'
                kx = BlockSize(2);
                kt = BlockSize(3);
                if ~isempty(varargin{2*aa})
                    kx = kx*varargin{2*aa}(1);
                    kt = kt*varargin{2*aa}(2);
                end
                gain = (2./(1+exp(kx*Frequency.x))-1).*(2./(1+exp(-kt*Frequency.t))-1)/2+0.5;
            case 'forward-moving-ideal'
                gain = sign(Frequency.x.*Frequency.t)/2+0.5;
            case 'backward-moving-ideal'
                gain = -sign(Frequency.x.*Frequency.t)/2+0.5;
            case {'unity' 'no-filter'}
                gain = 1;
            otherwise
                warning('Invalid Filter Type.  Setting Gain to Unity.');
                gain = 1;
        end
%        disp(max(gain,[],'all'));
%        disp(min(gain,[],'all'));
        wf = wf.*gain;
        clear gain n;
end
% 3D-iFFT
wf = real(ifftn(ifftshift(wf))).*mask;
end
```

BIBLIOGRAPHY

1. R. J. Adrian. On the role of conditional averages in turbulence theory. In *Symposia on Turbulence in Liquids*, 1975.

2. M. An, I. Gertner, M. Rofheart, and R. Tolimieri. Discrete fast fourier transorm algorithms: A tutorial survey. *Advances in Electronics and Electron Physics*, 80:1–67, 1991. doi: 10.1016/S0065-2539(08)60607-1.

3. R. B. Blackman and J. W. Tukey. *The Measurement of Power Spectra - From the Point of View of Communications Engineering*. Dover, 1958.

4. M. Born and E. Wolf. *Principles of Optics*. Pergamon, 1965.

5. S. Braun, editor. *Encyclopedia of Vibration*. Academic Press, 2001.

6. Brüel & Kjær. 2670. `https://www.bksv.com/-/media/literature/Product-Data/bp1584.ashx`, November 2018. Product Data.

7. Brüel & Kjær. 4939. `https://www.bksv.com/-/media/literature/Product-Data/bp1851.ashx`, October 2021. Product Data.

8. S. Butterworth. On the theory of filter amplifiers. *Experimental Wireless and the Wireless Engineer*, 7:536–541, 1930.

9. B. L. Catron, M. R. Rennie, S. Gordeyev, and E. J. Jumper. Effect of acoustic disturbances on aero-optical measurements. In *2018 Plasmadynamics and Lasers Conference*, 2018. doi: 10.2514/6.2018-3903.

10. B. L. Catron, M. R. Rennie, S. Gordeyev, and E. J. Jumper. Filtering of acoustic disturbances from aero-optical measurements. In *AIAA Scitech 2020 Forum*, 2020. doi: 10.2514/6.2020-0683.

11. A. CO. Sound measurement microphone. `https://www.aco-japan.co.jp/pdf/en_microphone.pdf`. Product Catalog.

12. N. De Lucca, S. Gordeyev, E. J. Jumper, and D. J. Wittich. Effects of engine acoustic waves on optical environment around turrets in-flight on aaol-t. *Optical Engineering*, 57(6), 2018. doi: 10.1117/1.OE.57.6.064107.

13. O. T. . E. Director. Fy99 annual report - airborne laser (abl). `https://www.globalsecurity.org/military/library/budget/fy1999/dot-e/airforce/99abl.html`, 2000.

14. E. J. Fitzgerald and E. J. Jumper. The optical distortion mechanism in a nearly incompressible free shear layer. *Journal of Fluid Mechanics*, 512:153–189, 2004. doi: 10.1017/S0022112004009553.

15. J. H. Gladstone and T. P. Dale. Researches on the refraction, dispersion, and sensitiveness of liquids. *Philosophical Transactions of the Royal Society of London*, 153:317–343, 1863.

16. J. W. Goodman. *Introduction to Fourier Optics*. McGraw-Hill, 1968.

17. S. Gordeyev, A. E. Smith, J. A. Cress, and E. J. Jumper. Experimental studies of aero-optical properties of subsonic turbulent boundary layers. *Journal of Fluid Mechanics*, 740:214–253, 2014. doi: 10.1017/jfm.2013.658.

18. F. Jacobsen and P. M. ller Juhl. *Fundamentals of General Linear Acoustics*. John Wiley & Sons, 2013.

19. W. C. G. Jr., Y. Hidaka, and T.Tanzawa. Refractivity of combustion gases. *Combustion and Flame*, 40:213–219, 1980. doi: 10.1016/0010-2180(81)90124-3.

20. E. J. Jumper and E. J. Fitzgerald. Recent advances in aero-optics. *Progress in Aerospace Sciences*, 37(3):299–339, 2001. doi: 10.1016/S0376-0421(01)00008-2.

21. E. J. Jumper, M. A. Zenk, S. Gordeyev, D. Cavalieri, and M. R. Whiteley. Airborne aero-optics laboratory. *Optical Engineering*, 52(7), 2013. doi: 10.1117/1.OE.52.7.071408.

22. M. V. Klein and T. E. Furtak. *Optics*. John Wiley & Sons, 2nd edition, 1986.

23. D. T. Kyrazis. Airborne laser laboratory departure from kirtland air force base and a brief history of aero-optics. *Optical Engineering*, 52(7), 2013. doi: 10.1117/1.OE.52.7.071403.

24. H. W. Liepmann. Deflection and diffusion of a light ray passing through a boundary layer. Technical Report SM-14397, Douglas Aircraft Company, Santa Monica Division, May 1952.

25. N. D. Lucca, S. Gordeyev, A. Smith, E. Jumper, M. Whiteley, and T. Neale. The removal of tunnel vibration induced corruption in aero-optical measurements. In *45th AIAA Plasmadynamics and Lasers Conference*, 2014. doi: 10.2514/6.2014-2494.

26. K. P. Lynch, R. Spillers, N. E. Miller, D. R. Guildenbecher, and S. Gordeyev. Aero-optical measurements of a mach 8 boundary layer. In *AIAA AVIATION 2021 Forum*, 2021. doi: 10.2514/6.2021-2831.

27. V. N. Mahajan. Strehl ratio for primary aberrations: some analytical results for circular and annular pupils. *Journal of the Optical Society of America*, 72(9):1258–1266, 1982. doi: 10.1364/JOSA.72.001258.

28. V. N. Mahajan. Strehl ratio for primary aberrations in terms of their aberration variance. *Journal of the Optical Society of America*, 73(6):860–861, 1983. doi: 10.1364/JOSA.73.000860.

29. J. H. McClellan. Multidimensional spectral estimation. *Proceedings of the IEEE*, 70(9):1029–1039, 1982. doi: 10.1109/PROC.1982.12431.

30. P. M. Morse and K. U. Ingard. *Theoretical Acoustics*. McGraw-Hill, 1968.

31. M. L. Munjal. *Acoustics of Ducts and Mufflers*. John Wiley & Sons, 2nd edition, 2014.

32. R. J. Noll. Zernike polynomials and atmospheric turbulence. *Journal of the Optical Society of America*, 66(3):207–211, 1976. doi: 10.1364/JOSA.66.000207.

33. PCB Piezotronics. 103B02. `https://www.pcb.com/contentStore/docs/pcb_corporate/pressure/products/specsheets/103b02_c.pdf`, October 2020. Product Specifications - Revision: C.

34. PCB Piezotronics. 352C33. `https://www.pcb.com/contentStore/docs/pcb_corporate/vibration/products/specsheets/352c33_h.pdf`, April 2008. Product Specifications - Revision: H.

35. Peerless. XT25SC90-04. `https://tymphany-driver-files.s3.us-west-1.amazonaws.com/files/driver/pdfs/XT25SC90-04.Rev1.MP1%20-%20Product%20Sheet.pdf`, August 2021. Product Sheet - Revision: 1.

36. C. Porter, M. Rennie, and E. Jumper. Aero-optic effects of a wingtip vortex. *AIAA Journal*, 51(7):1533–1541, 2013. doi: 10.2514/1.J050899.

37. R. H. Randall. *An Introduction to Acoustics*. Dover Publications, 1951.

38. R. M. Rennie, D. A. Duffin, and E. J. Jumper. Characterization and aero-optic correction of a forced two-dimensional weakly compressible shear layer. *AIAA Journal*, 46(11):2787–2795, 2008. doi: 10.2514/1.35290.

39. O. T. Schmidt and T. Colonius. Guide to spectral proper orthogonal decomposition. *AIAA Journal*, 58(3):1023–1033, 2020. doi: 10.2514/1.J058809.

40. J. P. Siegenthaler. *Guidelines for Adaptive-Optic Correction Based on Aperture Filtration*. Doctoral dissertation, University of Notre Dame, Notre Dame, IN, 2008.

41. J. P. Siegenthaler, S. Gordeyev, and E. Jumper. Shear layers and aperture effects for aero-optics. In *36th AIAA Plasmadynamics and Lasers Conference*, 2005. doi: 10.2514/6.2005-4772.

42. A. E. Smith, S. Gordeyev, and E. J. Jumper. Recent measurements of aero-optical effects caused by subsonic boundary layers. *Optical Engineering*, 52(7), 2013. doi: 10.1117/1.OE.52.7.071404.

43. H. A. Stine and W. Winovich. Light diffusion through high-speed turbulent boundary layers. Technical Report RM A56B21, National Advisory Committee For Aeronautics, May 1956.

44. S. L. Valley. Handbook of geophysiscs and space environments. Technical Report ADA056800, Air Force Cambridge Research Laboratories, April 1965.

45. K. Wang and M. Wang. Aero-optics of subsonic turbulent boundary layers. *Journal of Fluid Mechanics*, 696:122–151, 2012. doi: 10.1017/jfm.2012.11.